Astronomy Letters, Vol. 26, No. 2, 2000, pp. 104–115. Translated from Pis'ma v Astronomicheskiĭ Zhurnal, Vol. 26, No. 2, 2000, pp. 133–145.

A Spectroscopic Study of V1016 Ori

E. A. Vitrichenko[1] and V. G. Klochkova[2]

[1] *Space Research Institute, Russian Academy of Sciences, ul. Profsoyuznaya 84/32, Moscow, 117810 Russia*
[2] *Special Astrophysical Observatory, Russian Academy of Sciences, Nizhniĭ Arkhyz, Stavropolskiĭ kraĭ, 357147 Russia*

Received December 18, 1998; in final form, August 9, 1999

Abstract—Two CCD spectra of the star V1016 Ori were obtained with the echelle spectrograph of the 6-m (BTA) telescope. An analysis of these spectra allowed us to estimate the star's atmospheric parameters ($T_{\rm eff}$ = 29700 K, $\log g$ = 4.4) and projected rotational velocity ($V\sin i$ = 60 km s^{-1}) and to determine its chemical composition. Chemical anomalies were found. The Fe abundance is nearly solar; He, C, O, Mg, Al, Si are underabundant; and Ne, S, Zn are overabundant. The "spectroscopic" radius of the primary is in satisfactory agreement with its radius determined from the light and radial-velocity curves if the small star is assumed to lie in front of the giant star during an eclipse. The paradox of the primary's anomalous radius is thus resolved. A table of line equivalent widths and a portion of the star's spectrum are given in Appendices 1 and 2. © *2000 MAIK "Nauka/Interperiodica".*

INTRODUCTION

The Orion Trapezium is one of the youngest stellar complexes with ongoing star formation [1]. V1016 Ori is a member of the Orion Trapezium. This is an eclipsing star [2] for which the radial-velocity curve was constructed [3]. The binary period is $65\overset{\rm d}{.}4$, the magnitude is $V = 6\overset{m}{.}75$, and the spectral type is B0 V [4]. *UBVR* and *UBVRI* observations were obtained by Zakirov [5] and Bondar' and Vitrichenko [6], respectively. The star's spectrum was studied by Ismailov [7], Bossi *et al.* [8], and Cunha and Lambert [9, 10].

The star's continuum was investigated over a wide ($\lambda\lambda$ 0.36–4.7 μm) wavelength range [11]. The observed flux was shown to be represented as the sum of fluxes from four emission sources: (1) a B0 V primary of the eclipsing system, (2) an A0 V secondary of the eclipsing system, (3) a dust envelope around the secondary star with the temperature $T_{\rm d}$ = 1600 K, and (4) an infrared object with a temperature $T \sim 3000$ K. The latter component of the system may be a protostar in the Hayashi stage. The age of the Orion Trapezium stars is estimated to be 3×10^5 years, which is younger than the age of the Sun by four orders of magnitude. Since the early evolutionary phases of massive stars have not been studied adequately, a study of V1016 Ori can give valuable information.

The components' masses and radii can be determined in principle from the light and radial-velocity curves. Unfortunately, no secondary lines have been detected so far, which complicates the problem but, nevertheless, allows these parameters to be estimated in some approximation [12]. It follows from the light curve that the two components are of comparable brightness [5], but the spectrum of only one component is observed [12]. The contradiction can be explained by the fact that a semitransparent dust envelope around the secondary star rather than the secondary itself produces an eclipse [4, 13].

Bossi *et al.* [8] pointed out that the primary's radius determined from the light and radial-velocity curves turned out to be half the radius determined from its luminosity and temperature. The authors failed to explain this paradox.

Felli *et al.* [14] detected radio emission from the star at a wavelength of 6 cm. Other Orion Trapezium stars exhibit no such emission. A flare was reliably detected at this wavelength [15]. The authors concluded that the secondary was an active T Tau star.

An optical companion was discovered in V1016 Ori by speckle interferometry, which more closely coincides in position with the radio source than with the eclipsing system. The companion lies $0\overset{''}{.}2$ north of the binary. Its magnitudes are $K = 7\overset{m}{.}65$ and $H = 7\overset{m}{.}75$ [16].

Here, we set the following objectives:

(1) To determine the star's atmospheric parameters, i.e., to estimate $T_{\rm eff}$ and $\log g$ with the highest possible accuracy.

(2) To determine the star's chemical composition and to compare it with the solar composition in order to estimate the anomalies that can be presumed in a young object. The very location of the star in the gaseous Orion Nebula with abundance anomalies [17] can also result in anomalous abundances because of accretion. The dust envelope around the secondary, the separation of elements, and meridional circulation in the absence of corotation can produce abundance anomalies as well.

1063-7737/00/2602-0104$20.00

(3) To compare the observed spectrum with the synthetic spectrum constructed by using model atmospheres. This comparison requires the projected rotational velocity of the star and its microturbulence to be determined.

(4) To attempt to resolve the above paradox with the primary's radius.

OBSERVATIONAL MATERIAL

Two spectra of the star were obtained with the PFES echelle spectrograph of the BTA telescope. The detector was a CCD array [18]. Data on the observed spectra are given in Table 1. These spectra were previously used to determine the radial velocity [12].

The first and second columns give the spectrum numbers and the midexposure Julian dates, respectively. The phase was calculated with the period from [6], but the initial epoch is measured from the time of periastron passage by the star. The wavelength ranges and the star's refined radial velocities are listed in the next columns. The radial velocities differ from the previously published ones [12], which is attributable to the use of a different wavelength system and to a more critical line identification.

The spectra were calibrated in wavelength by using telluric lines. The radial velocities were determined from all the identified lines, except for the hydrogen and helium lines. We measured 170 and 155 lines in the first and second spectra, respectively.

Our measured equivalent widths are compared with those measured by Cunha and Lambert [9, 10] in Fig. 1. We see from this figure that there are no systematic differences. The internal accuracy of our measurements is ~0.004 Å, while the above authors estimated their measurement error to be ~0.003 Å. The rms deviation of our measurements from their ones is 0.015 Å. The disagreement with the internal errors can be explained both by the addition of errors and by random "bounces" of the measurements of three lines (see Fig. 1).

The main objective of obtaining spectroscopic observations is to search for secondary lines. A high signal-to-noise ratio and a good spectral resolution are required to solve this problem. Our spectra satisfy these requirements. The spectral resolution is 0.45 Å (in terms of the standard deviation), as determined from interstellar Na lines and emission lines of the Orion Nebula. This parameter for the primary lines is twice the above value, which is enough to solve the problem stated above.

A list of lines, their equivalent widths, and the elemental abundances deduced from these lines are given in *Appendix 1*. The spectrum-reduction technique is detailed in the introductory part.

A portion of the V1016 Ori spectrum is given in *Appendix 2*. Here, the two lower curves are the star's spectra, and the upper curve is the synthetic spectrum computed by using the STARSP code; the latter is based on the WIDTH6 code developed by R. Kurucz [19]. We chose the following model parameters: $T_{\rm eff}$ = 30000 K, $\log g$ = 4.5, metallicity [M/H] = 0, microturbulence ξ_t = 15 km s^{-1}, and $V\sin i$ = 60 km s^{-1}.

Table 1. Data on the spectra

No.	JD 2450000+	Exposure	Phase	λλ, Å	V_r, km s^{-1}
1	357.562	30^m	0.173	4165–8000	+46(1)
2	507.283	45	0.461	4330–7000	+51(1)

PROJECTED ROTATIONAL VELOCITY

To best fit a synthetic spectrum to the observed spectra and to solve the problem of corotation, it is necessary to estimate the projected rotational velocity.

We could not use published rotational-velocity calibrations based on the widths of classical He I and Mg II lines to estimate $V\sin i$, because these calibrations are reliable only for high rotational velocities. The calibration curve was constructed by means of the STARSP code, which yielded the projected rotational velocity for the observed line width. The results are presented in Table 2, which gives the measurements of other authors together with our measurements.

There is good agreement between the first two measurements, but our measurements differ markedly from them. We believe this difference to be caused by the different quality of the spectra. Our spectra are definitely of a better quality than those which were at the disposal of other authors. The relatively low rotational velocity can therefore be assumed to be real.

The synchronous rotational velocity is given in the last column of Table 2. When estimating the synchronous rotational velocity, we assumed the orbit to be circular and the primary's radius to be $3R_\odot$. Since the orbit

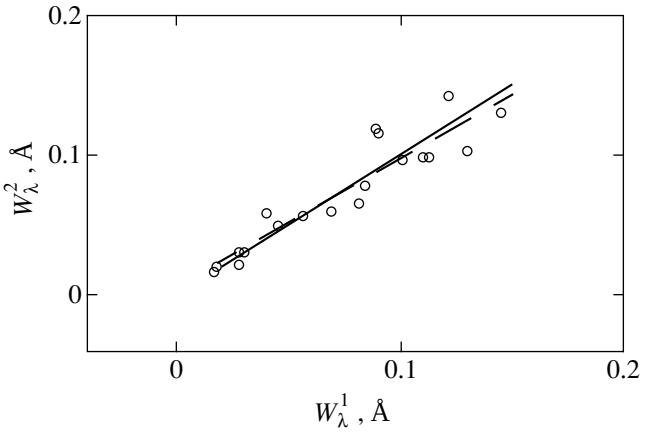

Fig. 1. Comparison of our measured line equivalent widths W_λ^1 (x axis) with the equivalent widths W_λ^2 (y axis) from [9, 10]. The solid line is the line of one-to-one correspondence, and the dashed line is a least-squares fit.

Table 2. Projected rotational velocity of V1016 Ori

Sources	$V\sin i$, km s^{-1}
Ismailov [7]	112(30)
Abt [30]	135(14)
This paper	60(2)
Corotation	2.3(2)

is elliptical, the angular velocity of the secondary star in the orbit changes by a factor of ~3. In this case, the term "corotation" therefore loses its meaning in an exact sense. Nevertheless, the difference is so large that we conclude that there are no conditions close to corotation: The star rotates around its axis considerably more rapidly than it did if the corotation conditions were satisfied.

STAR'S ATMOSPHERIC PARAMETERS AND ABUNDANCE DETERMINATION

Determining the chemical composition of the star requires estimating its atmospheric parameters: effective temperature $T_{\rm eff}$ and surface gravity g. However, for these parameters to be estimated, we must know the chemical composition. The problem thus turns out to be iterative.

We make three iterations. In the first iteration, we assume the chemical composition to be normal, take the published temperature and gravity, compute the line equivalent widths using models, construct the lines of equal equivalent widths (isolines) in the $T_{\rm eff}$–$\log g$ plane, and estimate $T_{\rm eff}$ and $\log g$ [20]. We estimate the microturbulence and its effect on the elemental abundance. In the second iteration, we allow for the chemical anomalies revealed in the first approximation in the model atmosphere, redetermine the chemical composition, and reconstruct the isolines in the $T_{\rm eff}$–$\log g$ plane. In the third iteration, we use the atmospheric parameters determined in the second approximation and take into account the ionization equilibrium. This last iteration is combined with the final determination of $T_{\rm eff}$, $\log g$, and chemical composition.

Estimates of the spectral type over a wide range can be found in the literature. Frost *et al.* [21] classified the star as Oe5. In his book [22], Martynov assigned the spectral type B4 to it. Such a large discrepancy can only be explained by the difficulty in classifying the B stars. The difficulty primarily lies in the fact that, as the star's temperature and gravity increase simultaneously, the ionization does not change, while the line intensity changes only slightly because of the high excitation potential of the observed lines. As a result, the spectrum changes only slightly. Only the hydrogen lines depend considerably more strongly on gravity than on temperature (the g effect), but they are measured with a large error.

Four examples of the V1016 Ori classification are given in Table 3. An examination of this table shows that the difference between the parameters is significant.

Ismailov's classification [7] is based on Kopylov's criteria [23]. Bossi *et al.* [8] determined the spectral type and luminosity class from the appearance of the spectrum. We estimated the temperature and gravity from the tables of Straizis and Kuriliene [24] in accordance with the estimated spectral type and luminosity class. Cunha and Lambert [9] used the following three criteria for the classification: the $[c_1]$ index, the Balmer jump, and the Hγ profile. The authors themselves write that their classification is unreliable, because the $[c_1]$ index is determined with a large uncertainty, while the other two criteria depend only slightly on temperature.

Our classification described below is given in the last row of Table 3.

The First Approximation. It is well known that, when the chemical composition is determined, the microturbulence ξ_t must be estimated. This parameter for V1016 Ori was estimated by two authors. Ismailov [7] obtained $\xi_t = 6.8$ km s^{-1} from the condition that the helium lines yielded the same abundance. Cunha and Lambert [9] determined ξ_t by the classical method from the condition that the oxygen lines yielded the same abundance. They obtained $\xi_t = 7.0$ and 5.0 km s^{-1} for the local-thermodynamic-equilibrium (LTE) and non-LTE cases, respectively. At the same time, the authors argue that the elemental abundances for B stars do not depend on microturbulence at all.

We decided to verify this conclusion. In Fig. 2a, the slope (b) of the straight line

$$\varepsilon(\mathrm{X/H}) = a + bW_\lambda \qquad (1)$$

is plotted against ξ_t for the oxygen (solid curve) and nitrogen (dashed curve) lines. In formula (1), the quantity ε(X/H) is the abundance of oxygen or nitrogen relative to hydrogen, and W_λ is the line equivalent width. We found that $b = 0$ for oxygen at $\xi = 10$ km s^{-1} and that the condition $b = 0$ was not satisfied for nitrogen at all values of ξ_t. The latter is explained by the fact that b depends not only on microturbulence but also on temperature, as confirmed by numerical simulations.

In Fig. 2b, the abundance of oxygen (solid line) and nitrogen (dashed line) is plotted against microturbulence ξ_t. An examination of the figure shows that the abundance of these elements depends only slightly on ξ_t in the range from 10 to 27 km s^{-1}, which confirms the conclusion of Cunha and Lambert [9]. There is no point in considering dependences similar to those in Fig. 2 for large ξ_t, because $\xi_t = 27$ km s^{-1} is equal to the speed of sound [25]. The abundance of other species is also insensitive to ξ_t. As a result of these studies, we arbitrarily assumed that $\xi_t = 15$ km s^{-1}. Increasing or decreasing this value by a factor of 1.5–2 causes the abundance to change by a few hundredths of dex (see

Fig. 2b), which is of the order of the measurement errors.

We constructed the lines of equal equivalent widths in the $T_{\rm eff}$–$\log g$ plane at [M/H] = 0 and ξ_t = 15 km s^{-1} for 30 lines but could not estimate the star's parameters. Since the isolines filled virtually the entire plane of the figure, we passed to the second approximation.

The Second Approximation. It follows from [9, 10] that, first, at least four elements exhibit an underabundance of ~0.3 dex. Second, the intensities of the most numerous O II lines are sensitive neither to temperature nor to gravity but only to abundance, which is anomalous. Third, the lines of some species (for example, C II and Al III) were found to be insensitive to gravity but sensitive only to temperature and abundance. The lines of such species cannot be used to determine the atmospheric parameters.

As this stage, we assumed that [M/H] = –0.2 dex for all metals. We chose all the three observed lines for hydrogen, two lines of moderate intensity for each of the species He I, C III, N III, and Si IV, and one line for C III and N III. Their mean isolines were constructed in the $T_{\rm eff}$–$\log g$ plane. The lines used to estimate the atmospheric parameters are listed in Table 4.

We could not use the isoline for color index in the $T_{\rm eff}$–$\log g$ plane. This isoline is nearly horizontal, fixing the effective temperature. However, the color index should not be used for V1016 Ori for the following three reasons. First, the color for early B stars depends only slightly on temperature. Second, the A0 secondary can distort appreciably the color, and this distortion is difficult to take into account, because the data on the secondary star are inaccurate. Third, the reddening law for the Orion Trapezium remains polemical, while the anomalies of this law distort [c_1].

The line equivalent widths used to construct Fig. 3 are distorted by the contribution of the secondary. If the magnitude difference is assumed to be $\Delta V = 2\overset{m}{.}4$ [6], then the line equivalent widths must be increased by ~9%. This correction affects the result only slightly. In addition, we show below that the magnitude difference between the components may be considerably larger. For these reasons, the correction was ignored.

The situation with the hydrogen lines is more complicated. We estimated the correction for the star's duplicity to be 20–30%, but this correction cannot be accurately calculated, because the data on the secondary are inadequate. On the other hand, the hydrogen-line equivalent widths were determined with a comparable error. Finally, allowance for the correction affects the result only slightly, because the hydrogen-line equivalent widths for early B stars depend so strongly on gravity that, at an error of 20% in the equivalent width, the error in $\log g$ is a mere 0.1 dex, which is smaller than the above error.

Table 3. Atmospheric parameters of the star

Source	Sp	$T_{\rm eff}$, K	$\log g$
Ismailov [7]	B1 V	26500	4.1
Bossi *et al*. [8]	B3 III-IV	20000:	3.8:
Cunha and Lambert [9]	B0.5 V	29970	3.92
This paper	B0(1) ZAMS	29700(700)	4.4(2)

The Third Approximation. The third approximation of estimating $T_{\rm eff}$ and $\log g$ is combined with the final determination of the star's chemical composition.

The result of this approximation is shown in Fig. 3. We see from the figure that the isolines form a band whose width in the central part is ~1400 K. In the first approximation, this width was ~3000 K. The three isolines for hydrogen which cross this band at an angle of ~60° have a peculiar location. They are found to fix the gravity.

The curve labeled Ion was obtained as follows. The spectrum exhibits lines of six elements in two adjacent

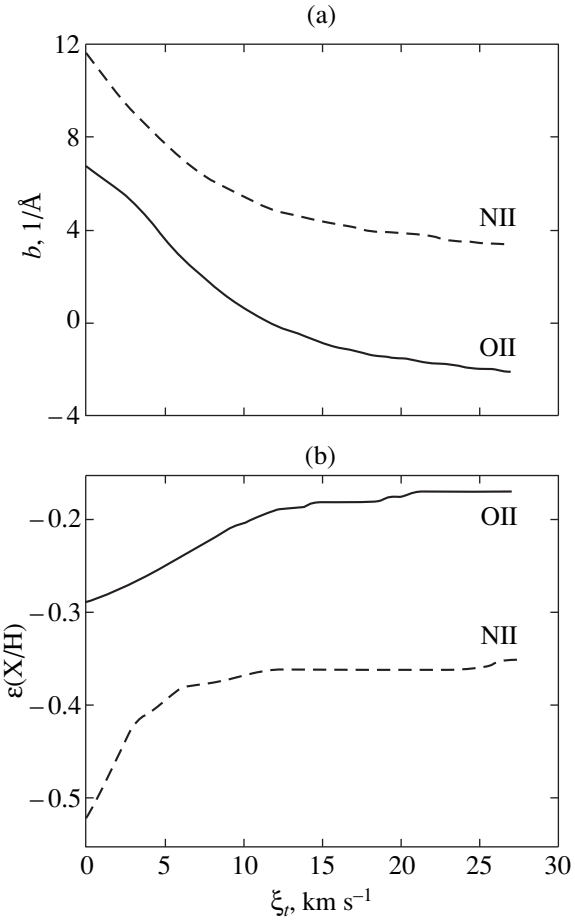

Fig. 2. (a) Coefficient b in $\varepsilon(X/H) = a + bW_\lambda$ versus microturbulence ξ_t for oxygen and nitrogen ions. (b) Oxygen and nitrogen abundances ε(X/H) determined from all lines versus microturbulence.

Table 4. List of lines used to determine the atmospheric parameters

Species	λ, Å
H	4340.46, 4861.32, 6562.80
He I	4437.55, 4921.93
He II	4685.70, 5411.52
C II	4647.42
N III	4634.13
Si IV	4212.40, 4654.31

ionization stages. For each pair of ions, we calculated the lines of equal abundances and averaged all the six isolines, because they show the same slope. This mean curve is plotted in the plane.

The ellipse marks the region with the center at $T_{\rm eff}$ = 29 700(700) K and $\log g$ = 4.4(2). The errors are given in parentheses.

We determined the chemical composition of V1016 Ori by means of the STARSP code with the following model-atmosphere parameters: $T_{\rm eff}$ = 30 000 K and $\log g$ = 4.5. We assumed [M/H] = –0.2 in our preliminary calculation; in the final calculation, we used the model atmosphere computed with a corrected chemical composition and with allowance for non-LTE effects for those ions for which these calculations were performed [20]. The oscillator strengths were taken from the VALD data bank. The results of the final calculation are summarized in Table 5.

The first column lists the species whose lines were used to determine the chemical composition. The hydrogen abundance was not analyzed. The second column gives the deviation of the star's elemental abundance from the solar one. The error in the abundance σ and the number of lines used *N* are given in the next two columns. The error is the error of the mean and depends on the number of lines used and on errors in the oscillator strengths, equivalent widths, atmospheric parameters, and departures from LTE. The elemental abundances, errors, and the number of lines from [9, 10] are listed in columns 5–7. These quantities are marked with asterisks. The last column gives the solar abundances from [26].

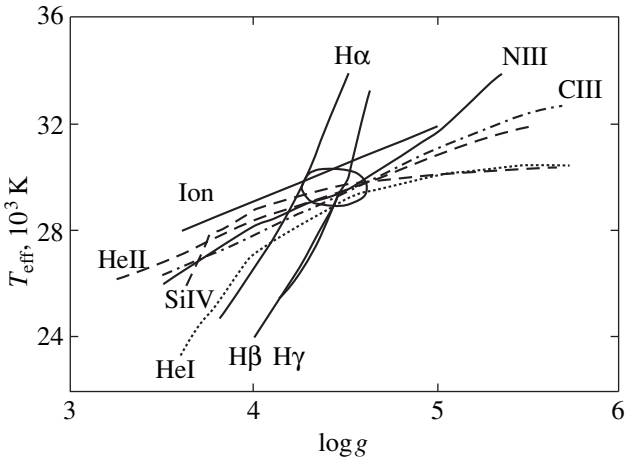

Fig. 3. $T_{\rm eff}$–log$g$ plane. The curves are lines of equal equivalent widths. The curve labeled Ion is the line of equal abundances of elements in two adjacent ionization stages (the mean of six pairs of ions). The ellipse center marks the chosen parameters.

The following general conclusion can be drawn from the abundance analysis. The Fe abundance is nearly solar or slightly enhanced; He, C, O, Mg, Al, Si are underabundant; and Ne, S, Zn are overabundant. The large Zn overabundance needs to be confirmed, because the abundance was estimated only from two lines, one of which was measured unreliably. For carbon, oxygen, and silicon, there are differences in the abundances derived from adjacent ionization stages. The result is unreliable for oxygen, because only one O III line was measured. This effect has remained incomprehensible. The cause should be sought in inaccuracy of the oscillator strengths or in peculiar atmospheric structure of the star.

PARAMETERS OF THE BINARY COMPONENTS

Determining the star's atmospheric parameters opens up a possibility for refining some of the stellar parameters. We estimate the primary's radius from the relation [27]

$$M_{\rm b} = 42.31 - 5\log R_1 - 10\log T_{\rm eff}, \qquad (2)$$

where $M_{\rm b} = -5^{m}.01(5)$ is the absolute bolometric magnitude [12]. From (2) we derive the radius of the primary star, $R_1 = 3.30(16)R_\odot$. This value is in good agreement with that [$R_1 = 3.2(4)R_\odot$] obtained in the above paper by the same method, but the error is a factor of 2.5 smaller, because the temperature was determined more accurately.

It follows from the light curve that the primary's radius is $r_{\rm s}$ = 0.0141(5), in fractions of the semimajor axis of the orbit [28]. The semimajor axis of the orbit was estimated to be $160R_\odot$ [12]. The primary's radius is thus $R_1 = 2.26(14)R_\odot$, which disagrees with the above estimate. This discrepancy was noted by Bossi *et al.* [8] and Vitrichenko *et al.* [12]. The discrepancy can be eliminated by assuming a different eclipse pattern. So far, it has been assumed that the giant cool star lies in front of the smaller primary star during an eclipse (the GS hypothesis). Let us consider a different assumption: the small cool star is in front of the giant star (the SG hypothesis). In the latter case, we can obtain a solution that satisfies the observations at the primary's radius $r_{\rm g}$ = 0.033(1) in conjunction and $r_{\rm g}$ = 0.0185(5) relative to the semimajor axis. We obtain $R_1 = 2.96(12)R_\odot$,

which is in considerably better agreement with the radius estimated from the luminosity and temperature.

The solution for the SG hypothesis can be obtained in the V band for approximately equal stellar radii and for the secondary's brightness $L_s \sim 0$; i.e., the secondary emits virtually no radiation in this band. If this is indeed the case, then the absence of its lines in the spectrum becomes clear. However, the question of its nature is yet to be solved.

The gravity determined from the star's classification ("spectroscopic" method) can be compared with that calculated from the mass and radius. Let us calculate $\log g$ from

$$g = g_\odot M_1/R_1^2, \quad (3)$$

where $g_\odot = 2.740 \times 10^4$ cm s^{-2} is the solar surface gravity, and $M_1 = 10.2M_\odot$ is the primary's mass [12]. Equation (3) yields $\log g = 4.37(4)$, in good agreement with the spectroscopically determined $\log g = 4.4(2)$.

CONCLUSIONS AND DISCUSSION

Our main results are as follows:

(1) We estimated the atmospheric parameters of the primary star: $T_{\rm eff} = 29700$ K and $\log g = 4.4$.

(2) The projected rotational velocity is $V\sin i = 60$ km s^{-1}, which is a factor of ~20 higher than that for corotation.

(3) The primary's chemical composition turned out to be anomalous. The Fe abundance is nearly solar; He, C, O, Mg, Al, Si are underabundant; and Ne, S, Zn are overabundant.

(4) We were able to resolve the paradox with the primary's radius. The two independent determinations of this radius agree if the radii of the primary and secondary stars are assumed to be virtually equal, consistent with the light curve.

Let us dwell on the questions that must be solved for the nature of V1016 Ori to be elucidated.

By analogy with BM Ori, we may assume that the primary has reached the zero-age main sequence (ZAMS), but the secondary, being less massive, must then be on the way to the ZAMS. The search for its lines in the spectrum must be continued; for this purpose, it is desirable to obtain a spectrum at the largest eclipse phase. The primary's spectrum will then be weakened, and the secondary lines will be easier to detect.

The agreement between the primary's radii determined by the spectroscopic method and by the method of solving the light and radial-velocity curves is a good argument for the correct estimate of the stellar masses. However, a new question arises. If the mass ratio is $q \sim 4$, then the ratio of bolometric luminosities is $L_2/L_1 \sim 4^4 \sim 260$. At this luminosity ratio, the A0 star cannot be responsible for the reddening at minimum light. Two cases are possible. In the first case, the reddening stems from the fact that a third star, for example, Θ^1 Ori A1 [16], falls within the photometer aperture. Its (dereddened) $K - H$ color index is nearly zero, so this may be either an A star or an M star. In the second case, the mass–luminosity law does not hold.

Table 5. Chemical composition of V1016 Ori

Species	[X/H]	σ	N	[X/H]*	σ*	N*	Sun
He I	−0.15	0.09	8				−1.05
He II	−0.26	0.12	2				−1.05
C II	−0.36	0.03	7	−0.19	0.06	2	−3.45
C III	0.00	0.10	5				−3.45
N II	−0.14	0.03	23	−0.37	0.05	4	−4.03
N III	−0.21		1				−4.03
O II	−0.29	0.03	52	−0.17	0.11	8	−3.13
O III	0.02		1				−3.13
Ne I	0.35		1				−3.92
Ne II	0.40	0.07	4				−3.92
Mg II	−0.17		1				−4.42
Al III	−0.24	0.09	3				−5.53
Si III	−0.33	0.14	12	−0.11	0.01	3	−4.45
Si IV	0.03	0.10	3				−4.45
S III	0.24	0.14	3				−4.79
Fe III	0.07	0.04	17				−4.50
Zn III	1.04	0.01	2				−7.40

A good observational test would be to determine the depths of infrared minima. If the eclipsing body is an M star, the primary minimum must decrease in depth, while the secondary minimum must increase. In the case of an A star, these effects must also be present, but their magnitude is much smaller.

The existence of a light-curve solution for the SG hypothesis casts doubt on the existence of a dust envelope around the secondary star [4, 13]. However, a question also arises here. How is the infrared excess formed? The dust enclosing the entire system must be colder. The problem of either an anomalous absorption law or the falling of a cool object within the photometer aperture arises again.

Cunha *et al.* [29] showed that the F and G stars in the Orion association had an iron underabundance, [Fe/H] = –0.16. We found the iron abundance in V1016 Ori to be either nearly solar or slightly enhanced. This disagreement is incomprehensible. The underabundance of helium and other light elements proves the youth of the system [20].

ACKNOWLEDGMENTS

We wish to thank V.V. Tsymbal, who provided the STARSP code that we widely used here. The line lists kindly sent to us from the Vienna Data Center (VALD) at our request were very helpful. We are grateful to L.I. Antipova, L.S. Lyubimkov, T.S. Ryabchikova, V.L. Khokhlova, and V.S. Shevchenko for useful discussions. We are also grateful to the referees, whose constructive and friendly remarks helped improve the content of the paper.

APPENDIX 1

EQUIVALENT WIDTHS OF LINES AND THE ABUNDANCES DETERMINED FROM THEM

The next table provides the line equivalent widths W_λ for V1016 Ori. The species and the wavelengths from the VALD line list are given in the first and second columns, respectively. The next-to-last column contains the line equivalent widths. The colon marks unreliable measurements. The abundances of each element relative to hydrogen are given in the last column. We assumed $\log\varepsilon = 0$ for hydrogen. If the abundance is not given, then the line was not used to determine the chemical composition.

The spectrum-reduction technique is described in [12], but we repeat here the basic principles.

All orders were combined into a single set, which was sorted by wavelength. The new set was filtered with a 0.8 Å wide rectangular window at steps of 0.4 Å. This filtration is convenient for adding up the overlapping spectral regions of adjacent orders. Measurements of the signal-to-noise ratio in several spectral regions without detectable absorption lines show that it was ~200 and ~400 before and after the filtration, respectively. Model simulations revealed a decrease in the spectral resolution by ~5%. The central line depth decreases by the same amount.

The spectral lines were identified by using the VALD line lists.

We measured the line equivalent widths and radial velocity by using our program. Each line (except for the hydrogen lines) was approximated by a Gaussian profile, which was least-squares fitted to the observed line profile. The radial velocity was determined from the profile shift. The equivalent width was determined by two methods. The first method involved integrating the line over the range that was manually specified in such a way that the line was within this range. The second method involved calculating the line equivalent width from the formula for the integral of a Gaussian profile. In the second method, the continuum was chosen anew (local continuum). In general, these two methods yielded different equivalent widths. The difference served to estimate the measurement error. The internal error was ~0.004 Å for weak and medium lines and ~10–20% for strong (helium and hydrogen) lines.

The choice of local continuum was made for two reasons. One reason is obvious: Otherwise, it would be impossible to measure weak lines in the wings of strong lines. The other reason is that, for such a relatively high signal-to-noise ratio, it is difficult to place the continuum with the required accuracy (~0.0025 in fractions of the continuum). Therefore, this continuum was first placed with an accuracy of ~0.01 and then refined by the least-squares method in the region with the measured line.

The hydrogen lines are particularly difficult to measure. First, it is difficult to place the continuum in an echelle spectrum. The length of one order in the blue is ~100 Å; the hydrogen-line width at the line base is the same. Meanwhile, a 2% error in the continuum placement gives a ~20% error in the equivalent width. Second, the hydrogen-line profile cannot be represented by a Gaussian. Third, the central part of the hydrogen lines is distorted by emission from the Orion Nebula. The hydrogen-line equivalent widths were measured manually on tracings of the spectrum. These measurements are unreliable for the reasons given above.

A comparison of the two spectra revealed no differences exceeding the observational errors, which allowed us to average the line equivalent widths.

Our equivalent-width determinations are compared with published ones in Fig. 1. There were a total of 19 common measurements. We see from the figure that the measurements are in satisfactory agreement. No systematic differences were found. The rms deviation from the line of one-to-one correspondence is 0.015 Å, which may be taken as the external error. The disagreement with the internal error is attributable to the marked difference of the measurements of three lines (see Fig. 1).

The hydrogen- and helium-line equivalent widths are given in [7]. They disagree with our measurements, which can be explained by the fact that our observational material is of a higher quality than that used by Ismailov [7].

We paid particular attention to the detection of misses in the measurements; for this purpose, we took the following measures. In most cases, we measured lines that were seen in both spectra, which ruled out the possibility of taking a local defect in the spectrum as a line. The measured radial velocities were analyzed by using the 2.5σ criterion, where $\sigma = 14$ km s^{-1} is the error of a single measurement from one spectrum. The same criterion was used to reject lines with an anomalous width and anomalous abundance as misses. For the second spectrum, the instrumental radial velocity (with no correction for the Earth's motion) is +76 km s^{-1}. The radial velocity of telluric lines is known to be nearly zero. This difference virtually rules out the possibility of taking a telluric line as a stellar line.

Species	λ, Å	W_λ, Å	logε	Species	λ, Å	W_λ, Å	logε
Hγ	4340.46	3.8:		N II	5045.10	0.025	–4.3
Hβ	4861.32	3.1:		N II	5535.35	0.010:	–4.0
Hα	6562.80	3.2:		N II	5666.63	0.028	
He I	4168.97	0.16		N II	5676.02	0.030	–4.2
He I	4387.93	0.60	–1.0	N II	5679.56	0.046	
He I	4437.55	0.084	–1.1	N II	5686.21	0.014	–4.4
He I	4471.47	0.90:	–1.1	N II	5710.77	0.029	–4.1
He I	4713.14	0.228	–1.3	N II	5931.78	0.031	–4.0
He I	4921.93	0.655	–0.9	N II	5941.65	0.106:	
He I	5015.68	0.22:	–1.5	N II	6379.62	0.006:	–4.3
He I	5047.74	0.138	–1.1	N II	6482.05	0.058:	–4.0
He I	5875.80	0.374:		N II	6610.56	0.005:	
He I	6678.15	0.38:	–1.6	N III	4634.13	0.027	–4.2
He II	4685.70	0.16	–1.1	O II	4078.76	0.034	–3.7
He II	5411.52	0.045:	–1.5	O II	4257.58	0.022	–3.3
C II	4267.13	0.135		O II	4275.53	0.115:	–3.3
C II	4409.16	0.040		O II	4276.76	0.17:	
C II	4411.15	0.025	–4.0	O II	4282.99	0.060	–3.4
C II	4619.25	0.056:	–3.7	O II	4285.21	0.082	
C II	5132.95	0.029	–3.8	O II	4288.80	0.065	–3.2
C II	5143.50	0.043:		O II	4291.27	0.120	–3.2
C II	5145.17	0.030	–3.8	O II	4294.87	0.084	–3.2
C II	5151.09	0.018	–3.7	O II	4303.61	0.136	–3.3
C II	6578.05	0.054:		O II	4313.42	0.077	–3.3
C II	6779.94	0.013		O II	4317.15	0.134	–3.3
C II	6783.91	0.030	–3.9	O II	4319.64	0.147	–3.5
C II	6791.46	0.012:	–3.7	O II	4325.76	0.094	
C III	4647.42	0.159	–3.7	O II	4347.38	0.12:	–3.5
C III	4665.86	0.024	–3.6	O II	4349.43	0.064	
C III	5272.52	0.017	–3.0	O II	4351.28	0.133	–3.3
C III	5695.91	0.091	–3.5	O II	4353.58	0.065:	–3.2
C III	5826.42	0.018	–3.5	O II	4366.91	0.088	–3.8
N II	4227.74	0.040		O II	4369.31	0.036	–3.5
N II	4237.05	0.060	–4.1	O II	4378.73	0.126	
N II	4241.79	0.074	–4.0	O II	4395.96	0.048	–3.5
N II	4432.74	0.024	–4.3	O II	4406.03	0.019	
N II	4447.03	0.08	–4.0	O II	4414.88	0.124	
N II	4607.15	0.016	–4.4	O II	4416.97	0.121	–3.7
N II	4613.87	0.040		O II	4443.04	0.028:	–3.5
N II	4621.39	0.029	–4.1	O II	4446.58	0.064:	
N II	4630.54	0.077	–4.2	O II	4448.34	0.097:	–3.2
N II	4779.72	0.015	–3.9	O II	4452.38	0.070	–3.3
N II	4788.14	0.016	–4.1	O II	4465.45	0.100:	
N II	4803.29	0.023	–4.2	O II	4487.72	0.038	–3.0
N II	4994.37	0.019	–4.2	O II	4488.19	0.047:	–3.4
N II	5001.47	0.068	–4.4	O II	4591.01	0.113	–3.7
N II	5010.62	0.026	–4.2	O II	4596.20	0.110	–3.6
N II	5025.66	0.016:	–4.0	O II	4602.06	0.057	–3.5

Species	λ, Å	W_λ, Å	logε	Species	λ, Å	W_λ, Å	logε
O II	4609.37	0.084	–3.4	Si III	4813.33	0.013	–5.5
O II	4638.86	0.100	–3.6	Si III	4819.71	0.031	–5.3
O II	4641.56	0.122		Si III	4828.95	0.032	–5.4
O II	4649.14	0.19:	–3.7	Si III	5113.76	0.020:	–4.0
O II	4650.85	0.17	–3.2	Si III	5473.04	0.032:	–4.2
O II	4661.64	0.090	–3.7	Si III	5739.73	0.070	–4.9
O II	4673.75	0.041	–3.3	Si III	6523.90	0.023:	
O II	4676.24	0.089	–3.6	Si III	6831.55	0.023:	–4.3
O II	4691.45	0.018	–3.3	Si III	6834.06	0.022	–4.1
O II	4696.36	0.024	–3.3	Si IV	4212.40	0.051	–4.3
O II	4699.19	0.083	–3.5	Si IV	4328.18	0.022:	–4.3
O II	4703.26	0.020:	–3.8	Si IV	4403.73	0.018	
O II	4705.32	0.084	–3.9	Si IV	4654.31	0.058	–4.7
O II	4709.99	0.061	–3.0	S III	4253.59	0.254	–4.4
O II	4741.69	0.020	–3.3	S III	4361.53	0.063:	–4.9
O II	4751.25	0.020	–3.3	S III	4439.84	0.07:	–4.3
O II	4843.26	0.026	–3.0	S III	4443.04	0.018	
O II	4871.54	0.043:	–3.1	Fe III	4286.16	0.06:	–4.1
O II	4890.85	0.032	–3.5	Fe III	4372.13	0.064	–4.4
O II	4906.82	0.054	–3.5	Fe III	4431.02	0.017	–4.2
O II	4924.52	0.098:	–3.3	Fe III	5127.39	0.025	–4.3
O II	4941.10	0.045	–3.7	Fe III	5156.11	0.027:	–4.5
O II	4943.00	0.056	–3.8	Fe III	5235.22	0.023:	–4.3
O II	4955.74	0.028	–3.4	Fe III	5243.31	0.022	
O II	5160.03	0.052		Fe III	5276.48	0.010	–4.7
O II	5175.99	0.028	–3.6	Fe III	5282.30	0.008	
O II	5190.56	0.030	–3.2	Fe III	5302.60	0.006	–4.8
O II	5206.71	0.036		Fe III	5330.73	0.031:	
O II	6098.51	0.025		Fe III	5573.42	0.007	–4.4
O II	6640.99	0.043	–3.2	Fe III	5833.94	0.013	
O II	6721.36	0.062	–3.3	Fe III	5854.62	0.018:	–4.4
O III	5592.25	0.016:	–3.1	Fe III	5886.63	0.029:	
Ne I	6402.25	0.023:	–3.6	Fe III	5891.90	0.042:	–4.4
Ne II	4219.74	0.065	–4.2	Fe III	5940.10	0.050:	
Ne II	4391.98	0.077	–3.4	Fe III	5953.61	0.013:	–4.7
Ne II	4428.63	0.039	–3.5	Fe III	5956.81	0.016:	
Ne II	4457.05	0.025:		Fe III	5976.76	0.036:	
Ne II	4899.61	0.022	–3.8	Fe III	5984.56	0.024	–4.2
Mg II	4481.13	0.12:	–4.6	Fe III	6036.55	0.013	–4.5
Al III	4479.89	0.02:	–6.0	Fe III	6048.71	0.011	–4.4
Al III	4529.19	0.059	–5.7	Fe III	6054.18	0.007:	–4.6
Al III	5722.73	0.029	–5.7	Fe III	6169.76	0.020	–4.4
Si III	4552.62	0.145	–5.0	Fe III	6194.78	0.021	
Si III	4567.84	0.132	–4.9	Ni III	5445.93	0.023:	–4.8
Si III	4574.76	0.082	–4.7	Zn III	5075.24	0.022	–6.3
Si III	4716.65	0.017	–5.2	Zn III	5336.86	0.010:	–6.4

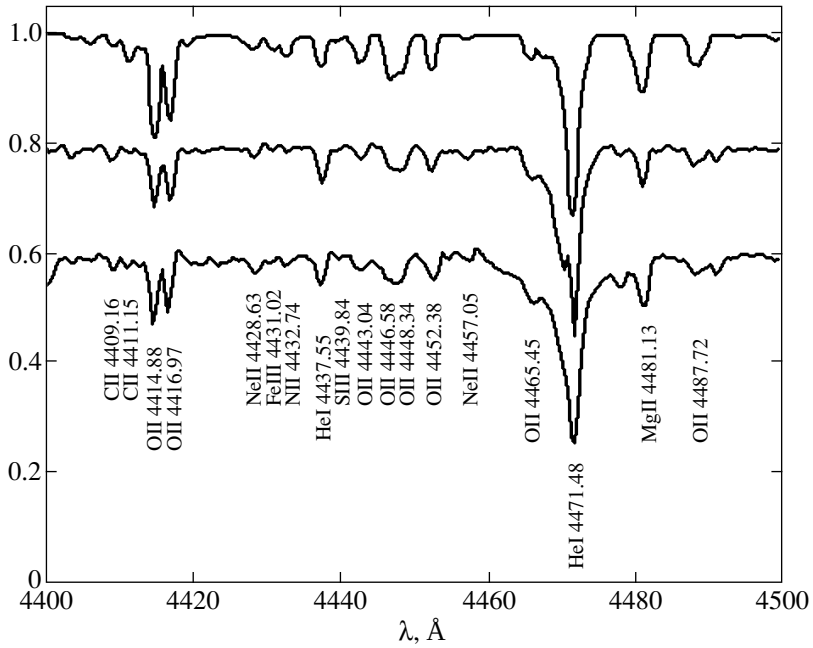

Portion of the V 1016Ori spectrum

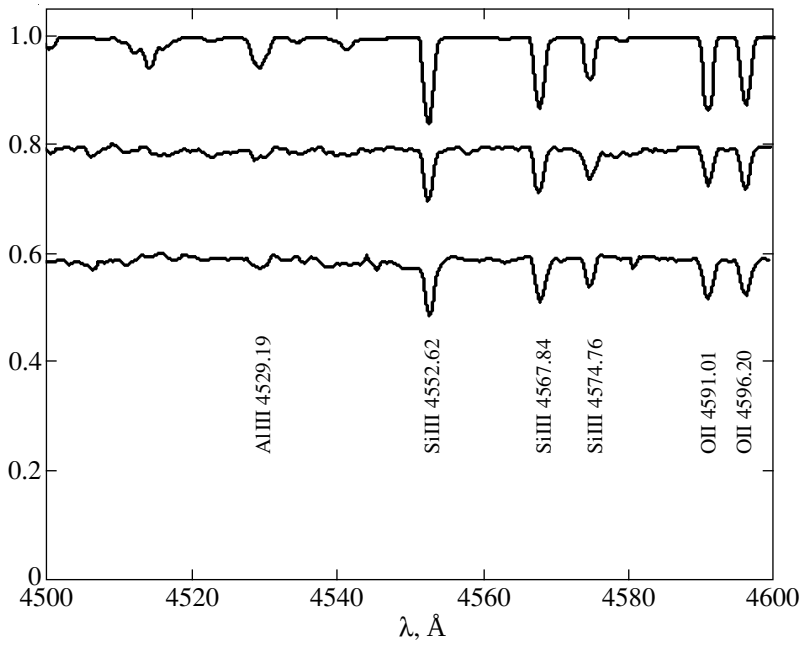

(Contd.)

APPENDIX 2

PORTION OF THE SPECTRUM FOR V1016 Ori

Here, we provide a portion of the star's spectrum constructed as follows. The upper curve is the synthetic spectrum computed by means of the STARSP code with $T_{\rm eff}$ = 30000 K, $\log g$ = 4.5, [M/H] = 0, and $V\sin i$ = 60 km s^{-1}. The middle and lower curves are spectra *1* and *2*, respectively. The spectrum numbers correspond to those in Table 1. All the three spectra were subject to the filtration described above.

The wavelengths (in Å) are laid off along the *x* axis. The observed spectra were displaced along the *x* axis by –21 km s^{-1} for spectrum 1 and by –76 km s^{-1} for spectrum *2*, which corresponds to the measured radial velocities without allowance for the Earth's motion with the opposite sign. This implies the reduction of the spectra to a zero radial velocity. The intensity (in fractions of the continuum) is laid off along the *y* axis. The observed spectra were arbitrarily displaced along the *y* axis by 0.2 (for spectrum *1*) and by 0.4 (for spectrum *2*).

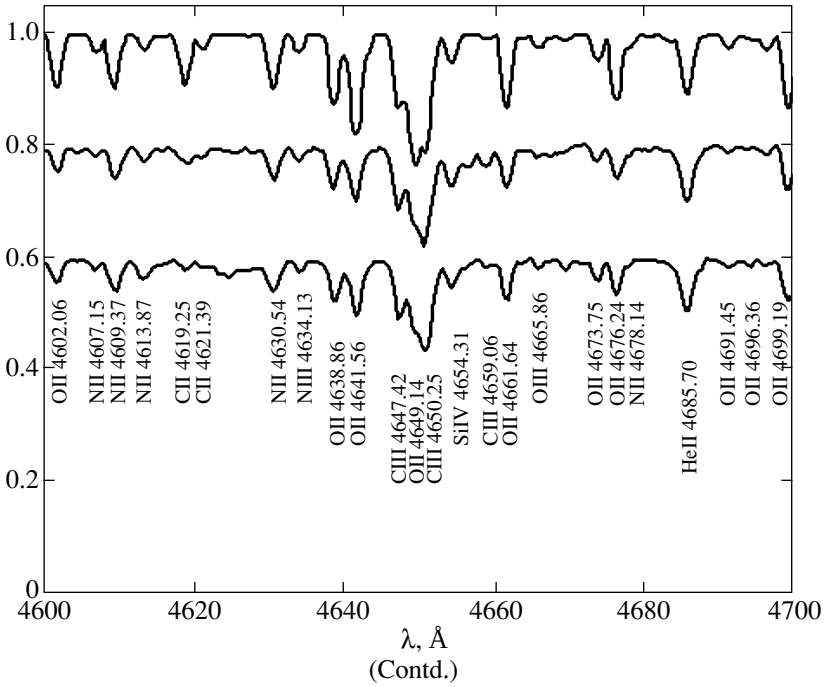

(Contd.)

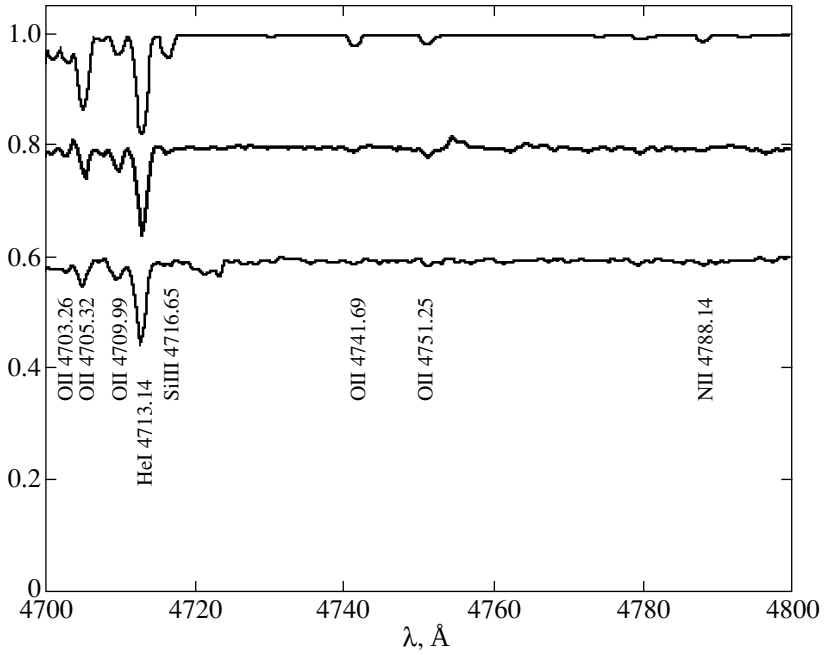

(Contd.)

All the measured stellar lines are marked in the plots. We did not mark telluric lines and bands, interstellar lines and bands, as well as emission lines belonging to the Orion Nebula.

Most of the stellar lines belong to O II. The line intensities of this species in the range of the above atmospheric parameters depend neither on temperature nor on gravity but on abundance alone. An examination of the spectra shows that the observed oxygen lines are weaker than the corresponding lines in the synthetic spectrum. This is a clear confirmation of the oxygen underabundance. The lines of other light elements are also weakened.

Our numerical simulations show the following:

(1) The synthetic spectrum computed with [X/H] = –0.2 differs only slightly in appearance from the observed spectra.

(2) By contrast to case (1), allowance for chemical anomalies and more accurate values of $T_{\rm eff}$ and log$g$ when computing the model atmosphere does not affect the spectrum and the elemental abundances.

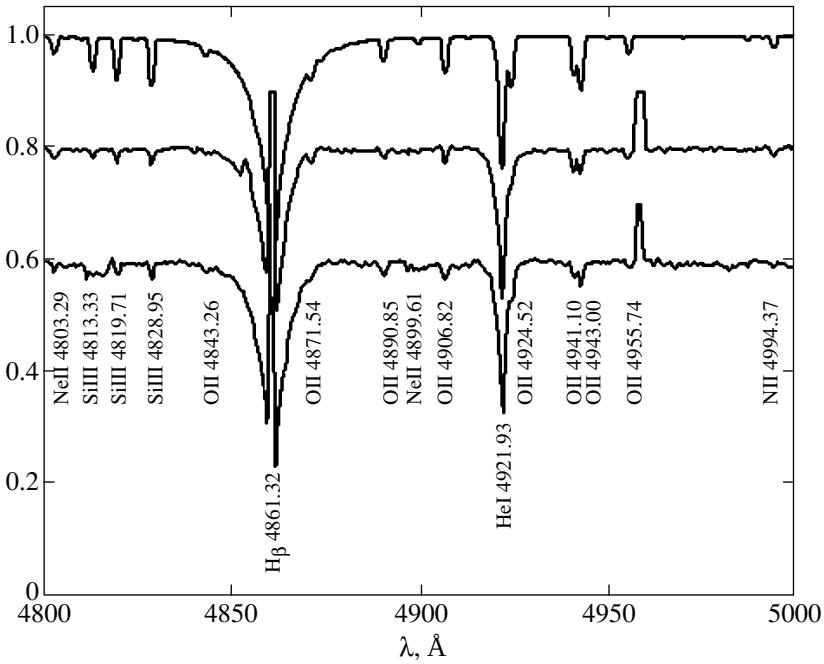

(Contd.)

REFERENCES

1. V. S. Shevchenko, *Ae/Be Herbig Stars* [in Russian] (Fan, Tashkent, 1989).
2. E. Lohsen, Inform Bull. Var. Stars No. 988, 1 (1975).
3. E. Lohsen, Inform. Bull. Var. Stars No. 1211, 1 (1976).
4. E. A. Vitrichenko, Pis'ma Astron. Zh. **24**, 708 (1998) [Astron. Lett. **24**, 611 (1998)].
5. M. M. Zakirov, Perem. Zvezdy **21**, 223 (1979).
6. N. I. Bondar' and E. A. Vitrichenko, Preprint No. 1992, IKI RAN (Space Research Inst., Russian Academy of Sciences) (1998).
7. N. Z. Ismailov, Pis'ma Astron. Zh. **14**, 327 (1988) [Sov. Astron. Lett. **14**, 138 (1988)].
8. M. Bossi, A. Gaspani, M. Scardia, *et al.*, Astron. Astrophys. **222**, 117 (1989).
9. K. Cunha and D. L. Lambert, Astrophys. J. **399**, 586 (1992).
10. K. Cunha and D. L. Lambert, Astrophys. J. **426**, 170 (1994).
11. E. A. Vitrichenko, Pis'ma Astron. Zh. **25**, 220 (1999) [Astron. Lett. **25**, 179 (1999)].
12. E. A. Vitrichenko, V. G. Klochkova, and S. Plachinda, Pis'ma Astron. Zh. **24**, 352 (1998) [Astron. Lett. **24**, 295 (1998)].
13. E. A. Vitrichenko, Preprint No. 1982, IKI RAN (Space Research Inst., Russian Academy of Sciences) (1998).
14. M. Felli, M. Massi, and V. Churchwell, Astron. Astrophys. **217**, 179 (1989).
15. M. Felli, M. Massi, and M. Catarzi, Astron. Astrophys. **248**, 453 (1991).
16. M. G. Petr, V. C. Foresto, S. V. W. Beckwith, *et al.*, Preprint No. 1998-5, Max Planck Inst. (1998).
17. K. Cunha, Rev. Mex. Astron. Astrofis. **27**, 111 (1993).
18. V. E. Panchuk, I. D. Naidenov, V. G. Klochkova, *et al.*, Byull. Spets. Astrofiz. Obs. **44**, 127 (1998).
19. V. V. Tsymbal, ASP Conf. Ser. **108**, 198 (1995).
20. L. S. Lyubimkov, *Stellar Chemical Composition: Method and Results of Analysis* [in Russian] (Astroprint, Odessa, 1995).
21. E. B. Frost, S. B. Barret, and O. Struve, Astrophys. J. **64**, 1 (1926).
22. D. Ya. Martynov, *A Course in General Astrophysics* [in Russian] (Nauka, Moscow, 1988).
23. I. M. Kopylov, Izv. Krymsk. Obs. **20**, 123 (1958).
24. V. Straizis and G. Kuriliene, Astrophys. Space Sci. **89**, 353 (1981).
25. J. E. Pringle, *Interacting Binary Stars* (Nauka, Moscow, 1993).
26. N. Grevesse, A. Noels, and A. J. Sauval, ASP Conf. Ser. **99**, 117 (1996).
27. C. W. Allen, *Astrophysical Quantities* (The Athlone, London, 1973).
28. N. I. Bondar', E. A. Vitrichenko, and M. M. Zakirov, Pis'ma Astron. Zh., 2000 (in press).
29. K. Cunha, V. V. Smith, and D. L. Lambert, Astrophys. J. **493**, 195 (1998).
29. H. A. Abt, Astron. J. **75**, 1095 (1970).

Translated by V. Astakhov

Astronomy Letters, Vol. 26, No. 2, 2000, pp. 116–121. Translated from Pis'ma v Astronomicheskiĭ Zhurnal, Vol. 26, No. 2, 2000, pp. 146–152.

The Triple System HR 7272

A. A. Tokovinin[1], R. F. Griffin[2], Yu. Yu. Balega[3], E. A. Pluzhnik[3], and S. Udry[4]

[1] *Sternberg Astronomical Institute, Universitetskiĭ pr. 13, Moscow, 119899 Russia*
[2] *Cambridge University, Cambridge, Great Britain*
[3] *Special Astrophysical Observatory, Russian Academy of Sciences, Nizhniĭ Arkhyz, Stavropolskiĭ kraĭ, 357147 Russia*
[4] *Observatoire de Genevé, Geneva, Switzerland*

Received July 8, 1999

Abstract—A combined spectroscopic–interferometric orbit is computed for the primary component of the visual binary star HR 7272 = ADS 12101. The orbital period is 3.55 years; semimajor axis $0\farcs074$. Radial velocities of both components were determined by correlation techniques; their semi-amplitudes are 6.6 and 8.4 km s^{-1}. Because those amplitudes are so modest, the correlation dips are never well resolved, and the mass ratio and orbital parallax remain poorly determined. Adopting normal masses for the components, we obtain the dynamical parallax; the Hipparcos parallax for this star seems to have a large error, probably because the orbital motion was not taken into account. The visual component B belongs to this system and has a constant radial velocity. *© 2000 MAIK "Nauka/Interperiodica".*

INTRODUCTION

The bright star HR 7272 (HD 178911, BD +34°3439) was first listed as a visual binary by F.G.W. Struve [1]; he gave the magnitudes, with remarkable accuracy, as $6\fm7$ and $8\fm0$ and described the colors with his usual precision as *subflava* and *subcinerea* (pale yellow and pale red). The system is known as Σ 2474 or as ADS 12101 [2].

Since the discovery of the pair, its separation has decreased from $17\farcs3$ to the present $16\farcs2$, with little change of position angle. The system has a high proper motion (+47 and +195 mas yr^{-1} in R.A. and declination, respectively), and the relative stability of the AB configuration attests that it is a physical pair. That is confirmed by the astrometric measurements made by Hipparcos [3], although the precision of the proper motion and parallax of B is low by Hipparcos standards.

A summary of available *UBV* data for HR 7272 is given in Table 1. The first *UBV* measurements of the components appear to be those made by Eggen [4, 5]. Sowell and Wilson [6] listed a *V* magnitude of $6\fm48$ for visual primary A and gave an explicit note, "Companion star excluded;" the total light from the two stars as measured by Eggen would, however, be $6\fm47$, so the note may be inaccurate. Olsen [7] gave *V* magnitudes for both components. The Tycho catalogue [3] gives *V* magnitudes appreciably brighter than any of the ground-based measurements (especially for B), which is caused by the mutual components' influence; a correction for this effect as prescribed by Halbwachs *et al.* [8] brings Tycho photometry in good agreement with that of Eggen.

The Bright Star Catalogue [9] records a spectral type of G1 V for A, but the only actual MK spectral classification that we have been able to retrieve is G5 V given by Harlan [10]. It seems likely that the Bright Star Catalogue simply dressed up the Mount Wilson classification [11] of dG1 to look like an MK type. The Mount Wilson authors' interest was to determine absolute luminosities by comparative line-strength measurements made on tracings of slit spectrograms; for HR 7272 A, they obtained $M_V = +4\fm2$, which would accord well with the spectral type they attributed to the star but is uncomfortably bright for G5 V. Now that A is known to be a binary, the difficulties with its spectral classification can be understood better. Elemental abundances in HR 7272 A were recently studied by Feltzing and Gustafsson [12], who found [Fe/H] = +0.06.

The radial velocity of component A is flagged in the Bright Star Catalogue as possibly variable. That is quite surprising inasmuch as only one value of the velocity had been published at that time—by Adams *et al.* [13] on the basis of three Mount Wilson prismatic spectrograms. The individual Mount Wilson velocities were subsequently published by Abt [14], whose listing discloses that the spectrograms were of quite modest dis-

Table 1. Photometry for HR 7272

Primary (A)			Secondary (B)			Reference
V	*B–V*	*U–B*	*V*	*B–V*	*U–B*	
6.74	0.63	0.15	8.12	0.75	0.33	[4, 5]
6.728	–	–	8.038	–	–	[7]
6.734	0.641	–	8.100	0.757	–	[3]

1063-7737/00/2602-0116$20.00

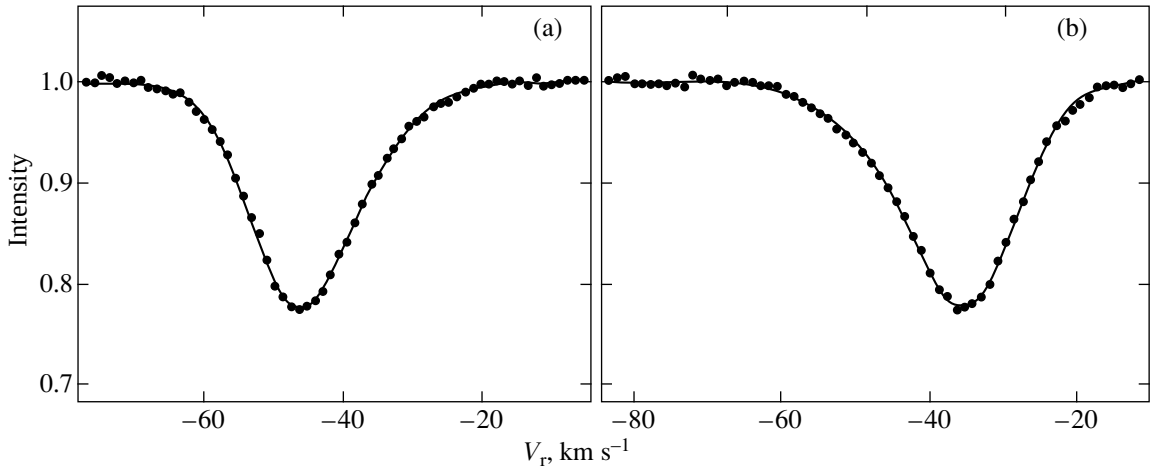

Fig. 1. Correlation dips of HR 7272A showing the two opposite asymmetries: (a) JD 2449242.4 and (b) JD 2450647.6. The fit by the sum of two Gaussians is indicated by the solid line.

persion (36 Å mm^{-1}) and agreed with one another as well as such velocities commonly did.

Beavers and Eitter [15] observed HR 7272 with the Erwin W. Fick Observatory radial-velocity spectrometer at Iowa State University in the years 1976 to 1978—quite intensively in the latter year. They accumulated 17 measurements of A and 13 of B. The mean velocities and their standard deviations, as well as the rms deviation of an individual observation from the mean, were essentially the same for both stars; neither was considered variable, but the observations did not continue for the duration of a complete orbital period of A and none was obtained in the vicinity of one of the nodes.

In 1985, the A component was resolved by speckle interferometry into a $0\farcs1$ binary by McAlister *et al.* [16], who designated it CHARA 84. A second measurement made in the same year showed that it has a rapid orbital motion. In retrospect it is clear that an interferometric orbit could have been determined rather quickly, but in fact this system has been somewhat neglected by the interferometrists. The most recent published measurement [17] was obtained by an advanced image-reconstruction method which allowed the magnitude difference between the components to be determined as $1\fm9 \pm 0\fm1$ at a wavelength of 656 nm.

OBSERVATIONS AND DATA REDUCTION

One of the authors (RFG) placed HR 7272 on his radial-velocity program in 1987, promptly upon the report of the discovery of the Aab subsystem. The object was later included in the Multiple Star Catalogue [18], and AAT started to measure its radial velocity in 1995. Both authors independently determined preliminary elements for the 3.5-year spectroscopic orbit before becoming aware of one another's interest in it.

RFG's observations were made in each season from 1987 to 1997 inclusive and cover nearly three orbital cycles, allowing the period to be determined quite accurately. Most of them were made with the Observatoire de Genevé CORAVEL radial-velocity spectrometer [19] at the 1-m telescope at Observatoire de Haute Provence (OHP); they include three measurements obtained by Dr Carquillat at RFG's request at critical phases in the orbit. There are 38 OHP observations altogether; they were supplemented in the 1996/97 season, when HR 7272 passed through both nodes, by eight observations made with the CORAVEL on the 0.9-m Cambridge telescope. In the orbit solution we adopt the errors of Cambridge observations to be 0.3 and 0.7 km s^{-1} for primary and secondary, respectively.

A correlation radial velocity meter (RVM) [20] was used for the second set of measurements, made by AAT. The observations were made in 1995–1998 with the 70-cm telescope at the Moscow University and with the 1-m telescope of the Simeiz Observatory in Crimea. The velocity zero-point was determined by observations of several IAU velocity standards on each night.

The radial-velocity amplitude is small, and the correlation dips are never fully resolved either with

Table 2. Interferometry of HR 7272 = CHARA 84

Epoch	θ	ρ	Aperture	Δθ	Δρ	Author
1985.5232	173.2	0.094	3.8	1.9	0.001	1
1985.8224	156.7	0.086	3.8	1.1	0.003	2
1989.7059	131.4	0.070	3.8	−3.0	0.002	3
1994.7337	228.2	0.088	6.0	−0.4	−0.002	4
1995.7618	187.9	0.093	2.5	0.1	−0.007	5
1998.777	207.2	0.099	6.0	−0.7	−0.001	6

Note: Authors: 1—McAlister *et al.* [16]; 2—McAlister *et al.* [25]; 3—McAlister *et al.* [26]; 4—Schoeller *et al.* [17]; 5—Hartkopf *et al.* [27]; 6—This paper.

Table 3. Radial velocities and residuals for HR 7272 A as inferred from CORAVEL data

JD +2400000	Primary			Secondary			JD +2400000	Primary			Secondary		
	V_r, km s^{-1}	σ, km s^{-1}	O–C, km s^{-1}	V_r, km s^{-1}	σ, km s^{-1}	O–C, km s^{-1}		V_r, km s^{-1}	σ, km s^{-1}	O–C, km s^{-1}	V_r, km s^{-1}	σ, km s^{-1}	O–C, km s^{-1}
47045.351	–37.61	0.46	0.07	–45.55	1.37	–0.28	49325.261	–36.52	0.43	–0.02	–47.13	1.06	–0.35
47053.350	–38.68	0.46	(–0.91)	–44.26	1.36	(0.90)	49349.225	–34.99	0.42	0.41	–48.45	0.86	–0.26
47234.690	–39.33	0.53	0.35	–43.86	2.09	–1.15	49402.731	–34.68	0.42	0.31	–47.84	0.92	0.86
47469.243	–41.66	0.42	0.43	–	–	–	49476.649	–35.69	0.43	0.04	–48.31	0.99	–0.54
47613.691	–44.09	0.55	–0.30	–36.51	2.22	0.95	49567.460	–36.80	0.43	0.05	–45.78	0.95	0.55
47646.660	–44.17	0.54	0.06	–35.63	2.16	1.27	49698.246	–38.33	0.43	0.01	–45.57	1.02	–1.15
47734.479	–45.67	0.47	–0.12	–36.39	1.46	–1.17	49873.590	–40.31	0.43	–0.16	–41.57	0.98	0.54
47827.306	–47.42	0.44	–0.23	–33.30	1.20	–0.18	50117.647	–43.52	0.43	–0.09	–37.21	1.05	0.71
48125.409	–35.21	0.48	–0.09	–48.25	1.64	0.29	50441.209	–47.56	0.42	0.00	–31.83	0.90	0.81
48145.335	–35.48	0.48	–0.16	–47.13	1.56	1.16	50474.732	–47.97	0.43	0.05	–32.55	1.01	–0.48
48282.735	–37.08	0.58	–0.09	–46.83	2.47	–0.68	50647.571	–35.30	0.42	0.04	–48.90	0.80	–0.64
48559.262	–39.98	0.46	–0.01	–41.94	1.38	0.41	50657.419	–35.34	0.43	–0.20	–49.27	1.03	–0.75
48609.215	–40.29	0.42	0.18	–43.05	0.92	–1.35	50701.384	–35.28	0.42	–0.28	–49.45	0.86	–0.76
48740.646	–41.52	0.28	0.30	–	–	–	50745.340	–36.77	0.42	(–1.37)	–47.88	0.89	(0.30)
48794.536	–41.81	0.32	0.60	–	–	–	50805.219	–36.30	0.43	–0.17	–47.53	0.95	–0.28
48847.503	–43.03	0.46	–0.01	–39.39	1.35	–0.94	50410.73	–47.1	(0.3)	–0.08	–34.8	(0.7)	–1.47
48977.211	–44.94	0.43	–0.22	–35.10	1.05	1.18	50508.70	–47.7	(0.3)	0.21	–32.5	(0.7)	–0.30
49036.701	–45.74	0.44	–0.09	–34.26	1.11	0.83	50538.70	–46.6	(0.3)	–0.12	–33.6	(0.7)	0.43
49176.577	–47.81	0.43	0.19	–32.60	1.02	–0.51	50554.63	–44.9	(0.3)	–0.06	–36.4	(0.7)	–0.27
49242.418	–46.44	0.42	0.04	–34.01	0.87	0.02	50571.60	–42.0	(0.5)	0.47	–	–	–
49269.364	–43.45	0.45	–0.10	–36.80	1.24	1.23	50580.57	–41.1	(0.5)	0.02	–	–	–
49287.280	–40.41	0.46	0.26	–43.82	1.37	–2.37	50616.55	–36.8	(0.3)	0.06	–46.5	(0.7)	–0.18
49317.267	–37.45	0.43	–0.34	–46.53	1.04	–0.53	50636.48	–35.7	(0.3)	0.00	–46.9	(0.7)	0.90

Note: The first 38 observations were obtained at the Observatoire de Haute Provence; the last eight, at Cambridge.

CORAVEL or with RVM: The blend of Aa and Ab just changes its contrast and shape with orbital phase. The situation is illustrated in Fig. 1, which shows examples of correlation dips at both nodes. When reducing CORAVEL data, we fitted the blended dips with double Gaussians of fixed width and contrast. Except for three OHP and two Cambridge observations, all taken very close to times when the velocities of the two components would have been identical, all CORAVEL dips could be "split" to yield the velocities of both stars. The dips of both primary and secondary are very narrow, and the minimum possible width (corresponding to zero rotational velocity) was adopted. As for contrasts, we tried several combinations that would provide the correct overall dip contrast and the best representation of the asymmetric dip "shoulders" at the times of maximum velocity difference (nodal passages). Our final choice of individual dip contrasts was guided by the interferometric measurement of the magnitude difference between Aa and Ab [17].

The RVM data were not processed in the same manner: The dips were fitted by a single Gaussian. Thus, RVM velocities represent a blend dominated by the primary component. The contribution of the secondary reduces the apparent amplitude of RV variation by ~10%. Only CORAVEL velocities were used in the final orbit adjustment.

The five speckle-interferometric measurements and their residuals to our orbit are given in Table 2. The last measurement has not yet been published; it was obtained by Balega *et al.* at the 6-m telescope in October 1998, when a preliminary orbital solution already existed.

CORAVEL radial velocities of HR 7272 A and their residuals are given in Table 3, and RVM velocities in Table 4. In Table 4, we also give the individual velocities of the visual secondary B; its mean value is –40.65 ± 0.16 (CORAVEL, n = 9) or –40.36 ± 0.17 km s^{-1} (RVM, n = 22). CORAVEL shows remarkably constant radial velocity of B, while RVM data suggest a low-amplitude (<1 km s^{-1}) variability. In fact, this variability is caused by the problems with RVM velocity zero point encountered in 1997, which show up in the velocities of A as well.

Table 4. Other radial-velocity measurements for HR 7272 A and B

JD +2400000	V_r, km s^{-1}	σ, km s^{-1}	Component, instrument	JD +2400000	V_r, km s^{-1}	σ, km s^{-1}	Component, instrument*
1. HR 7272A, RVM				50333.259	–41.33	0.23	BR
49980.304	–41.35	0.14	AR	50344.285	–39.54	0.23	BR
49999.292	–40.96	0.15	AR	50352.274	–39.98	0.15	BR
50327.309	–43.94	0.14	AR	50357.296	–40.52	0.16	BR
50333.257	–45.28	0.19	AR	50530.600	–41.42	0.40	BR
50344.281	–43.94	0.17	AR	50596.442	–41.06	0.27	BR
50352.238	–44.43	0.15	AR	50633.391	–39.66	0.16	BR
50357.293	–44.83	0.21	AR	50639.371	–39.91	0.16	BR
50530.597	–47.00	0.30	AR	50647.357	–40.47	0.24	BR
50596.438	–40.06	0.16	AR	50655.413	–40.83	0.29	BR
50614.499	–38.61	0.16	AR	50667.456	–41.75	0.30	BR
50633.388	–36.98	0.13	AR	50700.238	–41.69	0.16	BR
50639.367	–36.48	0.12	AR	50706.386	–38.87	0.18	BR
50647.353	–36.76	0.16	AR	50758.251	–40.55	0.23	BR
50655.412	–35.04	0.26	AR	50773.113	–39.80	0.31	BR
50667.458	–34.45	0.27	AR	50902.537	–39.82	0.22	BR
50700.233	–35.74	0.21	AR	50933.482	–40.29	0.31	BR
50706.383	–34.25	0.18	AR	51057.270	–39.83	0.30	BR
50758.244	–36.74	0.22	AR	51065.294	–40.48	0.21	BR
50773.106	–35.79	0.22	AR	3. HR 7272B, CORAVEL			
50798.106	–37.82	0.33	AR	47469.245	–40.48	0.33	BC
50902.533	–37.82	0.18	AR	47613.690	–40.63	0.39	BC
50933.478	–38.85	0.28	AR	47827.310	–40.92	0.35	BC
51057.267	–39.39	0.15	AR	48125.413	–40.64	0.37	BC
51065.299	–40.80	0.15	AR	48145.338	–40.72	0.35	BC
2. HR 7272B, RVM				48282.736	–40.30	0.53	BC
49980.306	–40.54	0.20	BR	48740.655	–40.58	0.33	BC
49999.285	–41.28	0.12	BR	48977.215	–40.48	0.40	BC
50327.311	–38.83	0.26	BR	50657.424	–41.00	0.40	BC

* Components: A—visual primary, and B—visual secondary. Instruments: R = RVM and C = CORAVEL (OHP).

THE ORBIT

The available data are sufficient to determine the full set of ten orbital elements (visual and spectroscopic). As usual, the elements and their formal errors were found by a least-squares fit, with weights inversely proportional to the squares of measurement errors. The errors of most speckle measurements are, however, not provided by their authors. We ascribed an error of $0\overset{''}{.}003$ to all measurements except that of 1995.76, which was given an error of $0\overset{''}{.}006$ because of the smaller telescope aperture used. The errors of Cambridge velocities (given in Table 3 in parentheses) are also provided only for the purpose of weighting.

The initial least-squares orbit solution have clearly indicated that the radial velocity residuals for the primary are appreciably smaller than what could be expected from their formal errors. This degrades the overall accuracy of the solution, because the poorly measured radial velocities of the secondary receive a relatively higher weight. So, the final solution was

Table 5. Orbital elements for HR 7272 A

Period P	1296.3 ± 1.1 d. (3.55 years)
Periastron epoch T	JD 2450572.2 ± 1.5 (1997.337)
Eccentricity e	0.589 ± 0.004
Semimajor axis a	$0\overset{''}{.}0735 \pm 0\overset{''}{.}0026$
Node	$276\overset{\circ}{.}7 \pm 1\overset{\circ}{.}5$
ω_A	$262\overset{\circ}{.}5 \pm 0\overset{\circ}{.}8$
Inclination i	$150\overset{\circ}{.}1 \pm 3\overset{\circ}{.}7$
K_1	6.57 ± 0.04 km s^{-1}
K_2	8.39 ± 0.17 km s^{-1}
System velocity	-41.01 ± 0.03 km s^{-1}
M_1	$1.07 \pm 0.37 M_\odot$
M_2	$0.84 \pm 0.29 M_\odot$
Orbital parallax	$0\overset{''}{.}025 \pm 0\overset{''}{.}008$
Residuals	
Primary	0.20 km s^{-1}
Secondary	0.80 km s^{-1}
P.A.	$1\overset{'}{.}5$
Separation	$0\overset{''}{.}003$

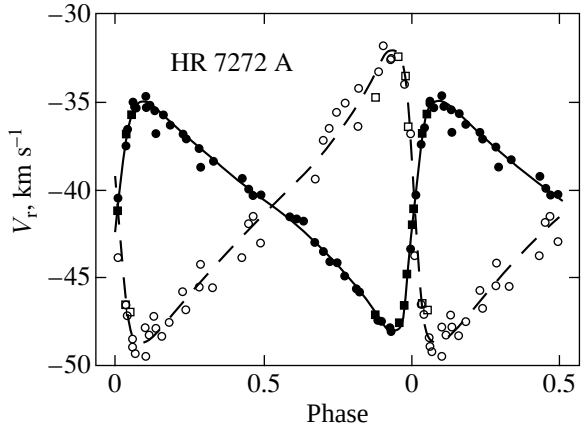

Fig. 2. Radial-velocity curve of HR 7272 A. The primary is represented by the solid line and filled circles; the secondary is represented by the dashed line and open circles. The Cambridge observations are indicated by filled and open squares.

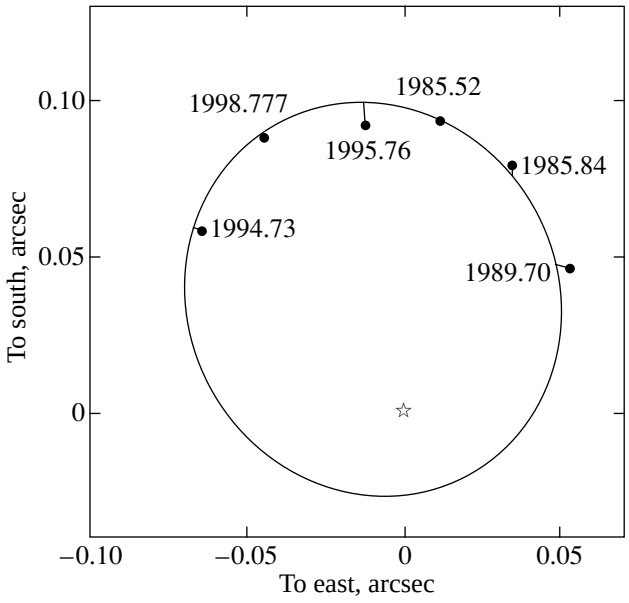

Fig. 3. Interferometric observations of HR 7272 A = CHARA 84 are connected with their expected positions on the orbit. The primary is designated by a star at the coordinate origin.

obtained by renormalizing the weights of primary and secondary velocities and of the speckle observations in such a way that their respective χ^2 are equal to their number of observations.

Table 6. Physical parameters of the components (model)

Component	Aa	Ab	Aa + Ab	B
Spectral type	G1V	K1V	–	G8V
V	6.90	8.90	6.74	8.12
$B–V$	0.61	0.87	0.64	0.75
Mass, $M_\odot$	1.1	0.79	1.89	0.87
M_V	3.96	5.96	–	5.18

We gave zero weight to the velocities derived from blended dips, as well as to the CORAVEL observations at JD 2447053 and JD 2447045. There seems to be nothing abnormal about these two rejected points, but their inclusion into the orbital solution increases the primary rms residuals from 0.2 to 0.3 km s^{-1} and reduces the primary amplitude significantly, to 6.50 km s^{-1}. The rejected observations might have been affected by the visual secondary which was separated by only 16″ along the CORAVEL slit.

The orbital elements are given in Table 5. We also give the orbital masses and the orbital parallax, their errors computed using the full covariance matrix of the least-squares problem. The rms residuals (error of unit weight) in radial velocity, position angle and separation can be found in Table 5 as well. Figure 2 shows the radial-velocity curve. The visual orbit is plotted in Fig. 3.

The formal errors in K_1 and K_2 are misleading: The true uncertainties are much larger, particularly for K_2, because the severe mutual blending (cf. Fig. 1) prevented us from measuring the dip parameters directly and we had to assume them in the radial-velocity reductions. An alternative set of reductions with reduced contrast of the secondary dip (and increased contrast of the primary) leads to velocity semi-amplitudes of 6.10 and 11.12 km s^{-1} or a mass ratio of 0.55 (to be compared to 0.78 for the orbital elements in Table 5).

Looking at Fig. 3, we remark that the available interferometric observations cover only about one half of the orbital ellipse. That is understandable, because the system spends most of the time away from periastron. The next periastron passage is predicted for November 20, 2000. The closest separation is expected to be 26 mas, so the system should remain resolvable at the 6-m telescope. More complete interferometric coverage of the orbit would result in much more reliable determination of the inclination (masses derived from the combined orbit are proportional to $\sin^3 i$). The blame for the low accuracy of the orbital masses is thus shared between uncertain radial-velocity reductions and insufficient speckle coverage.

SYSTEM MODEL AND COMPONENT PARAMETERS

The adopted parameters of all three components of HR 7272 are given in Table 6. The magnitude difference of $1\overset{m}{.}9 \pm 0\overset{m}{.}1$ measured by Schoeller *et al.* [17] in the red must correspond to a difference of about $2\overset{m}{.}0$ in the V band. The visual magnitudes of Aa and Ab are then $6\overset{m}{.}90$ and $8\overset{m}{.}90$. We selected the spectral types matching both this difference and the combined $B–V$ color. The masses in Table 6 correspond to the spectral types; they are taken from [21] and agree well with the directly derived orbital masses.

The dynamical parallax computed with the mass sum of $1.89 M_\odot$ is 25.6 mas. It differs significantly from

the Hipparcos parallax, $\pi_{HIP} = 0\farcs0204 \pm 0\farcs0016$. The liability of Hipparcos parallaxes to vitiation through unrecognized orbital motion was explicitly pointed out by the Hipparcos authors ([3], vol. 1, p. 79). Similar cases of binaries with periods of the order of a year and wrong Hipparcos parallaxes were noted by Shatskii and Tokovinin [22] and Griffin and Griffin [23]. The dynamical parallax places Aa and B about $0\fm6$ and $0\fm4$ above the main sequence as defined by the standard relations for dwarf stars [21]. Hence, the components may be slightly evolved.

The equivalent width *EW* of the correlation dip of the visual secondary B, as measured by RVM, is 3.03 ± 0.04 km s^{-1}. According to the calibration of RVM [24], the *EW* expected for $B–V = 0.75$ is 3.06 km s^{-1}. The agreement implies that the star has a normal (solar) metal abundance, in accord with Feltzing and Gustafsson [12]. The components of the Galactic velocity $(U, V, W) = (–48.5, –24.1, –1.0)$ km s^{-1}, as calculated with our dynamical parallax and the Hipparcos proper motion, indicate that the object belongs to a disk population of intermediate age. The rotational velocities of all components must be very small (less than $\lesssim 1$ km s^{-1}), as evidenced by their narrow dips.

CONCLUSION

The first combined spectroscopic–interferometric orbit for HR 7272 A = CHARA 84 is given. Orbital masses and parallax are still too uncertain to be of value. However, the new orbit allows us to predict the future orbital motion and to plan further interferometric observations around the time of the next periastron passage in November 2000. If they can be supplemented with high-resolution spectroscopy to measure the mass ratio with more reliability, orbital masses with an accuracy of a few percent may be obtained. The comparison of masses and luminosities with evolutionary tracks will then be interesting for this triple system where two components seem to be overluminous.

ACKNOWLEDGMENTS

RFG is grateful to Dr M. Mayor and the Observatoire de Genevé for the use of CORAVEL and to Dr Carquillat for the observations in Table 3. AAT thanks Drs. Sachkov, Gorynya and Glushkova for some measurements made at his request in 1997. This study was supported in part by the UK SERC/PPARC with respect to travelling expenses. A support of the Russian program “Astronomy” is acknowledged by AAT.

REFERENCES

1. F. G. W. Struve, *Catalogues 795 Stellarum Duplicium et Multiplicium* (Dorpat., Typographia Academia, 1822).
2. R. G. Aitken, *New General Catalogue of Double Stars* (Carnegie Inst., 1932), No. 417.
3. *The Hipparcos and Tycho Catalogues* (European Space Agency, 1997), SP-1200.
4. O. J. Eggen, Roy. Obs. Bull., No. 120, E350 (1966).
5. O. J. Eggen, Roy. Obs. Bull., No. 137, E263 (1968).
6. J. R. Sowell and J. M. Wilson, Publ. Astron. Soc. Pac. **105**, 36 (1993).
7. E. H. Olsen, Astron. Astrophys., Suppl. Ser. **102**, 89 (1993).
8. J. L. Halbwachs, S. Piquard, P. Virelizier, *et al.*, in *Proceedings of ESA Symposium Hipparcos-Venice 97*, ESA SP-402 (1997), p. 263.
9. D. Hoffleit and C. Jaschek, *Bright Star Catalogue*, 4th ed. (Yale University Observatory, New Haven, 1982).
10. E. A. Harlan, Astron. J. **79**, 682 (1974).
11. W. S. Adams, A. H. Joy, M. L. Humason, *et al.*, Astrophys. J. **81**, 187 (1935).
12. S. Feltzing and B. Gustafsson, Astron. Astrophys. Suppl. Ser. **129**, 237 (1998).
13. W. S. Adams, A. H. Joy, R. F. Sanford, *et al.*, Astrophys. J. **70**, 207 (1929).
14. H. A. Abt, Astrophys. J., Suppl. Ser. **26**, 365 (1973).
15. W. I. Beavers and J. J. Eitter, Astrophys. J., Suppl. Ser. **62**, 147 (1986).
16. H. A. McAlister, W. I. Hartkopf, D. J. Hutter, *et al.*, Astron. J. **93**, 183 (1987).
17. M. Schoeller, I. I. Balega, Yu. Yu. Balega, *et al.*, Pis’ma Astron. Zh. **24**, 337 (1998) [Astron. Lett. **24**, 283 (1998)].
18. A. A. Tokovinin, Astron. Astrophys., Suppl. Ser. **124**, 75 (1997).
19. A. Baranne, M. Mayor, and J. L. Poncet, Vistas in Astron. **23**, 279 (1979).
20. A. A. Tokovinin, Astron. Zh. **64**, 196 (1987).
21. K. R. Lang, *Astrophysical Data: Planets and Stars* (Springer, 1992).
22. N. I. Shatskii and A. A. Tokovinin, Pis’ma Astron. Zh. **24**, 780 (1998) [Astron. Lett. **24**, 673 (1998)].
23. R. E. M. Griffin and R. F. Griffin, Mon. Not. R. Astron. Soc. **305**, 641 (1999).
24. A. A. Tokovinin, Pis’ma Astron. Zh. **16**, 52 (1990) [Sov. Astron. Lett. **16**, 24 (1990)].
25. H. A. McAlister, W. I. Hartkopf, D. J. Hutter, *et al.*, Astron. J. **93**, 688 (1987).
26. H. A. McAlister, B. D. Mason, W. I. Hartkopf, *et al.*, Astron. J. **106**, 1639 (1993).
27. W. I. Hartkopf, H. A. McAlister, B. D. Mason, *et al.*, Astron. J. **114**, 1639 (1997).

Translated by A. Tokovinin

Astronomy Letters, Vol. 26, No. 2, 2000, pp. 122–128. Translated from Pis'ma v Astronomicheskiĭ Zhurnal, Vol. 26, No. 2, 2000, pp. 153–160.

Formation of SCR Energy Spectra during Stochastic Acceleration with Allowance for Coulomb Losses

V. M. Ostryakov[1], Yu. Yu. Kartavykh[1], and G. A. Koval'tsov[2]

[1] *St. Petersburg State Technical University, ul. Politekhnicheskaya 29, St. Petersburg, 195251 Russia*
[2] *Ioffe Physicotechnical Institute, Russian Academy of Sciences, ul. Politekhnicheskaya 26, St. Petersburg, 194021 Russia*

Received January 27, 1999; in final form, July 8, 1999

Abstract—The stochastic acceleration of heavy ions by Alfvén turbulence is considered with allowance for Coulomb losses. The pattern of energy dependence of these losses gives rise to characteristic features in the energy spectra of the accelerated particles at energies of the order of several MeV nucleon^{-1}. The manifestation of these features in the spectra is sensitive to the temperature and density of the medium, which can serve as a basis for plasma diagnostics in the flare region. Some impulsive solar energetic particle events during which features in the spectra of ^{3}He and ^{4}He were observed are considered as an example. *© 2000 MAIK "Nauka/Interperiodica".*

INTRODUCTION

Presently, there are extensive experimental data on directly measured energy spectra of solar energetic particles and secondary emissions from flare regions. This makes it possible to theoretically model their generation in such regions. The nonthermal spectra of ions are formed in stiff competition of their acceleration and energy losses. Among the latter, we note ionization losses and adiabatic (during the expansion of a magnetic arch) losses, as well as losses associated with the Coulomb deceleration of heavy ions in plasma. We take into account only the Coulomb losses, which are probably most important in the hot plasma of solar flares. As was noted by Korchak [1], the energy dependence of these losses for different particles must manifest itself in their nonthermal spectra, i.e., during their acceleration. More specifically, since the Coulomb losses have a maximum at energies of ~ 0.2–10 MeV nucleon^{-1} and are vanishingly small at low and high energies, characteristic dips must appear in the spectra in this energy range. The profile of such a feature must be very sensitive to the temperature T and density n of the background medium in which the acceleration takes place. This, in turn, can serve as an important tool for diagnosing the flare plasma. Conversely, the absence of such a feature allows an upper limit on the plasma density to be estimated (provided that the characteristic particle acceleration times are known in order of magnitude).

Here, we discuss the stochastic acceleration of heavy particles by Alfvén turbulence by including Coulomb losses in the analysis and study the effect of basic plasma parameters (T and n) on the resulting nonthermal ion spectra. By comparing computed and observed spectra, we determine the characteristic plasma parameters that could explain the measured spectra with their characteristic features at energies of ~1 MeV nucleon^{-1}. Moreover, neglecting the energy losses of particles during their acceleration causes significant difficulty in interpreting some features in the observed spectra (a steepening and flattening of the spectra, characteristic dips, etc.; see below). Note also that the stochastic mechanism of particle generation by Alfvén turbulence is typical of impulsive solar cosmic ray (SCR) events, which are considerably enriched by heavy elements (in particular, by ^{3}He) and exhibit a high electron-to-proton flux ratio in interplanetary space [2].

A MODEL OF STOCHASTIC ACCELERATION

Let us consider the stochastic acceleration of heavy particles by Alfvén turbulence with allowance for Coulomb losses. We assume that the acceleration and spatial diffusion take place under the effect of this turbulence in a one-dimensional region of size L with the x axis directed along it ($0 \le x \le L$). The acceleration region is uniformly filled with thermal plasma, in which the turbulence is distributed uniformly and the particles are injected at point x_0 with momentum p_0 (or energy E_0, which was taken to be 50–100 keV nucleon^{-1}). In what follows, E and p are measured per nucleon. The evolution of the distribution function $f(p, x, t)$ obeys the Fokker–Planck equation with appropriate boundary and initial conditions:

$$\frac{\partial f}{\partial t} = \frac{1}{p^2}\frac{\partial}{\partial p}p^2 D_p \frac{\partial f}{\partial p} + \chi\frac{\partial^2 f}{\partial x^2} - \frac{1}{p^2}\frac{\partial}{\partial p}\left(p^2\left(\frac{dp}{dt}\right)_c f\right),$$
$$f|_{x=0} = f|_{x=L} = 0, \qquad (1)$$
$$-\left(4\pi p^2 D_p \frac{\partial f}{\partial p}\right)\Bigg|_{p=p_0} = \delta(x-x_0)\delta(t), \quad f|_{t=0} = 0,$$

1063-7737/00/2602-0122$20.00 © 2000 MAIK "Nauka/Interperiodica"

where $(dp/dt)_c$ is the Coulomb friction force. In the nonrelativistic case, the diffusion coefficients in momentum and coordinate space for one-dimensional Alfvén waves propagating along a regular magnetic field B are, respectively, [3, 4]

$$D_p = D_p^0\left(\frac{Q}{A}\right)^{2-s}E^{\frac{s-1}{2}}, \quad \chi = \chi^0\left(\frac{A}{Q}\right)^{2-s}E^{\frac{3-s}{2}}, \quad (2)$$

where s is the index of the turbulence spectrum with energy density $W(k) = W_0k^{-s}$ in a unit interval of wave numbers k, $k_{min} \le k \le k_{max}$; Q is the charge of the accelerated ion; and A is its mass number. Here, $k_{max} \sim \omega_{Bp}/V_A$ is determined by the condition for the cyclotron damping of Alfvén waves in plasma [5], where ω_{Bp} is the proton gyrofrequency and V_A is the Alfvén velocity. Since the bulk of the turbulence energy for a falling turbulence spectrum is contained on large spatial scales, k_{max} does not affect the estimate of its total energy. In addition, for the typical plasma parameters obtained in our calculations (see below), k_{max} corresponds to ion energies that are well below E_0. Hence, this quantity has no effect on our calculations and may be set equal to infinity. As for the parameter k_{min}, it is clear that $k_{min} \equiv 2\pi/l \ge 2\pi/L$ (l is the main turbulence scale, which largely determines the characteristic ion acceleration time). Below, we assume that $l \sim 0.1L$. If we adopt $l \sim L$, then the accelerated-particle spectra cannot be computed in terms of the model of spatially homogeneous turbulence with random phases. Rejecting this model would considerably complicate the statement of the problem, leading it away from the essence of the issues considered here. Furthermore, the chosen value of k_{min} corresponds to the far relativistic range of particle energies, which is not considered here. As for the Coulomb losses of an ion in hydrogen plasma of temperature T and density n, in the nonrelativistic case, they are [6, 7]

$$\left(\frac{dp}{dt}\right)_c = -\frac{C}{p^2}\zeta(p),$$

$$\zeta(p) = \Phi\left(\frac{p}{p_T}\right) + \frac{m_e}{m_p}\Phi\left(\sqrt{\frac{m_p}{m_e}}\frac{p}{p_T}\right) - \frac{p}{p_T}\left[\left(1+\frac{m_e}{Am_p}\right)\Phi'\left(\frac{p}{p_T}\right) + \left(1+\frac{1}{A}\right)\sqrt{\frac{m_e}{m_p}}\Phi'\left(\sqrt{\frac{m_p}{m_e}}\frac{p}{p_T}\right)\right], \quad (3)$$

where $C = \frac{4\pi e^4\Lambda m_p^2}{m_e}\frac{Q^2}{A}n$, $p_T = m_pV_e = m_p\sqrt{\frac{2kT}{m_e}}$, $\Phi(x)$, and $\Phi'(x)$ are the probability integral and its derivative; m_e and m_p are the electron and proton masses, respectively; Λ is the Coulomb logarithm, and e is the electron charge. The first of the free terms and of the terms in square brackets in (3) dominate and determine the deceleration by the plasma electron component, while the second determine the deceleration by the plasma proton component. The positions of the maxima of the Coulomb losses during the ion deceleration by electrons ($E_{max,e}$) and protons ($E_{max,p}$) are determined by temperature: $E_{max,e} \approx (9/8)(p_T^2/m_p)$, $E_{max,p} \approx (m_e/m_p)E_{max,e}$. These maxima are approximately equal to

$$\left(\frac{dE}{dt}\right)_{max,e} \approx \frac{0.525}{m_pp_T}C, \quad \left(\frac{dE}{dt}\right)_{max,p} = \sqrt{\frac{m_e}{m_p}}\left(\frac{dE}{dt}\right)_{max,e}. \quad (4)$$

These maxima at a low acceleration rate can produce a Coulomb barrier, which hampers the gain of energy by the accelerated particles and gives rise to features in the particle spectra [1].

We integrate the Fokker–Planck equation (1) over time and change to the dimensionless variables $q = \frac{p}{p_1}$, $y = \frac{x}{L}$:

$$\frac{1}{q^2}\frac{\partial}{\partial q}q^{s+1}\frac{\partial\tilde{N}}{\partial q} + \frac{\tau_a}{\tau_d}q^{3-s}\frac{\partial^2\tilde{N}}{\partial y^2} + \frac{\tau_a}{\tau_c}\frac{1}{q^2}\frac{\partial}{\partial q}(\zeta(p_1q)\tilde{N}) = 0,$$
$$\tilde{N}\big|_{y=0} = \tilde{N}\big|_{y=1} = 0, \quad (5)$$
$$-\left(4\pi q^{s+1}\frac{\partial\tilde{N}}{\partial q}\right)\Big|_{q=q_0} = \frac{\tau_a}{Lp_1^3}\delta(y-y_0),$$

where $\tilde{N} = \int_0^\infty f(p, x, t)dt$, $y_0 = x_0/L$. The quantities τ_a, τ_d, and τ_c mathematically represent the times that scale the problem:

$$\tau_a = \frac{p_1^2}{D_p(p_1)}, \quad \tau_d = \frac{L^2}{\chi(p_1)}, \quad \tau_c = \frac{p_1}{(C/p_1^2)}; \quad (6)$$

below, p_1 is assumed to correspond to an energy of 1 MeV nucleon^{-1}. Their meaning is clear from relations (6): They are, respectively, the characteristic times of particle acceleration, diffusion (or confinement) in the region, and particle energy losses during the propagation. We see from the first equation in (5) that the accelerated-particle spectrum is determined by the ratios of these times τ_a/τ_c and τ_a/τ_d, temperature T involved in the function $\zeta(p_1q)$, turbulence spectral index s, initial particle-injection momentum p_0, and coordinate y_0 of the injection point. Note that we chose the initial particle energy E_0 in such a way that the Alfvén turbulence was effective enough to accelerate the particles ($V > V_A$). As for the energy gain from thermal energies up to E_0, this is the separate problem of preacceleration (see [2] and references therein) which was not considered here.

Note that the physical acceleration and diffusion times characterizing the problem in question differ from the times scaling this problem. A careful analysis shows that these physical times are approximately an

order of magnitude shorter than those given by formulas (6). For example, the mean time of particle confinement in the acceleration region for injection at point $y_0 = 0.5$ yields $L^2/(8\chi)$ [8], while the acceleration time of particles with velocity V turns out to be $E/(dE/dt)_{acc} = \tau_a/(2(s+2))$, where $(dE/dt)_{acc} = (V/p^2) \times d(Vp^2D_p)/dE$ is the mean rate of energy gain [9]. Nevertheless, our subsequent estimates are based on relations (6). As regards the physical acceleration and diffusion times typical of solar flares, they can be estimated independently from, respectively, the rise and decline in the hard X-ray and gamma-ray emissions from flare regions. These times can be in the range 0.1–10^3 s, thereby specifying a rather wide range of their ratio that affects the resulting spectrum. Meanwhile, the characteristic time of Coulomb losses can be estimated from the density of the plasma in which the particle acceleration takes place. It is the shortness of this time compared to τ_a and τ_d (in other words, the significance of Coulomb losses) that gives rise to the features in the energy spectra discussed below. For example, according to relation (6), for plasma densities of 10^{10}–10^{12} cm^{-3}, $\tau_c \approx (0.3\text{–}30)A/Q^2$ s for ions with an energy of 1 MeV nucleon^{-1}.

We now briefly describe the procedure for solving the problem formulated above by the Monte Carlo method [10]. This procedure, as applied to stochastic acceleration, was previously described in detail by Kartavykh *et al.* [11–13]. Thus, according to Eq. (1), a particle with momentum p_0 injected at point y_0 changes its coordinate and energy with time. If the time interval Δt in which the scattering occurs is chosen to be sufficiently short, then, replacing the differentials with finite differences, we can determine the particle energy increment in time Δt at the ith discrete step

$$E_i - E_{i-1} \equiv \Delta E = \psi(E_{i-1})\Delta t + (dE/dt)_c\Delta t + dE,$$

where dE is a random variable with a Gaussian distribution with a zero mean and variance $\delta^2 = 2\varphi(E_{i-1})\Delta t$ (the functions ψ and φ can be easily derived from Eqs. (1) by changing to an energy variable; see [13]). Similarly, we have for the increment of the spatial coordinate: $x_i - x_{i-1} = dx$ (dx is also a random variable with a Gaussian distribution with a zero mean and variance $\delta^2 = 2\chi\Delta t$). The particle escape through the boundaries of the acceleration region is assumed to be free (there is no reflection from the boundaries), which corresponds to the boundary conditions of the first kind. The particle is considered detected if it has crossed the limits of the spatial interval $[0, L]$, regardless of the number of steps required to reach the boundary points; having gone outside the above boundaries, it can no longer return to the acceleration region. This corresponds to the steady-state formulation of the problem. The particles that have escaped from the region under consideration represent the population of particles whose energy spectrum is studied here.

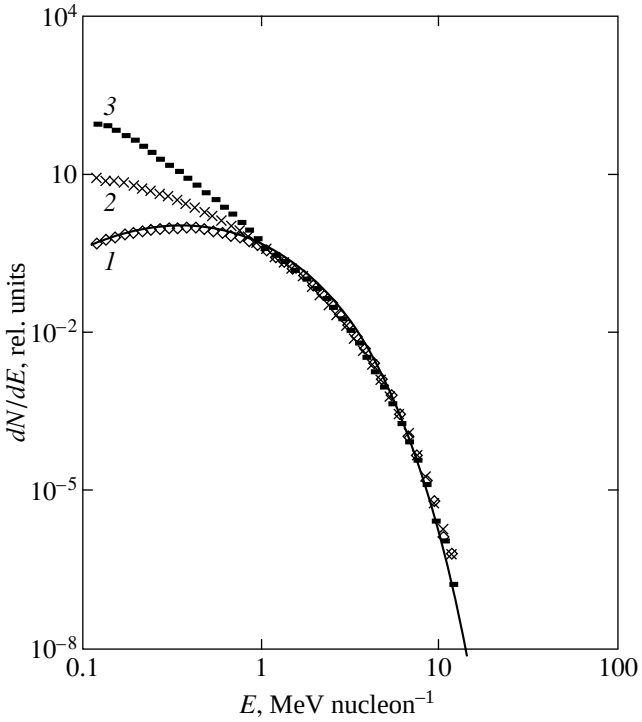

Fig. 1. Energy spectra of ^{4}He for $T = 1.4 \times 10^6$ K, $\tau_a/\tau_d = 2$, and $\tau_a/\tau_c = 0$ (no Coulomb losses, curve *1*), $\tau_a/\tau_c = 3$ (curve *2*), $\tau_a/\tau_c = 5$ (curve *3*). The solid line represents the analytic solution in the absence of Coulomb losses [4].

RESULTS OF NUMERICAL CALCULATIONS

Thus, here we consider the time-integrated (stationary) spectrum of the particles that escape from the acceleration region. Note that the stationarity is realized if the lifetime of the accelerating turbulence considerably exceeds the characteristic time of particle escape from this region. Since the time of the subsequent interplanetary propagation exceeds appreciably the duration of operation of the acceleration mechanism, the measured fluxes refer to the spectrum of the particles escaping from the Sun averaged over the flare duration. The temporal formulation of the problem would thus be difficult to compare with observations, although it would undoubtedly present a more general and interesting problem.

By way of illustration, Fig. 1 shows the computed spectra of ^{4}He for the plasma temperature $T = 1.4 \times 10^6$ K and for τ_a/τ_d and τ_a/τ_c given in the figure caption. In the absence of energy losses and for $s = 3/2$, the ion spectra have exponential cutoffs at high energies, in agreement with the well-known analytic solutions of similar problems [4, 14, 15]. Note that most of the observed spectra in impulsive events appear to correspond more closely to the case with such cutoffs. As was noted in the Introduction, allowance for the Coulomb deceleration of particles gives rise to features in the spectra at energies of ~1 MeV nucleon^{-1}, which correspond to the maximum of the function $-(dE/dt)_c$. The solid line in Fig. 1 also represents the analytic solution of Eq. (1) without

Coulomb losses [4], which closely matches our Monte-Carlo solution for this case. Note that the spectrum does not depend on these losses and is determined by τ_a/τ_d alone at sufficiently high energies, at which all curves in Fig. 1 are normalized identically. Their increase, for example, due to an increase of the plasma density in the acceleration region, causes the energy spectrum to steepen at low energies.

The effect of various parameters on the particle energy spectra can be described as follows. The τ_a/τ_d ratio determines the spectrum shape at energies $E \gg E_{\max, e}$, where the Coulomb losses may be neglected, while τ_a/τ_c is related to the height of the Coulomb barrier and determines the spectrum shape in the energy range where these losses are significant. The temperature T is responsible for the width and location of their maximum. Both these parameters (τ_a/τ_c and T) determine the intensities and positions of the features in the energy spectrum attributable to the losses under consideration. At the same time, their effects on the resulting ion spectra are difficult to separate.

Figure 2 shows the computed spectra of the accelerated ^{3}He and ^{4}He as the temperature and density change. We can see the strong effect of the acceleration-region plasma parameters in question on these spectra. Almost all of them have characteristic dips at energies of several MeV nucleon^{-1} if τ_a/τ_c is larger than several units. Such features, which were predicted by Korchak [1] and obtained in our calculations, were actually observed in helium data in a number of ^{3}He-rich solar events [16] and probably for heavier ions, such as oxygen and iron [17–19]. However, it should be noted that many experimental spectra exhibit no such features. This may suggest that either the acceleration was very effective or it took place in a very tenuous medium. The authors of the experiments mentioned above [16] qualitatively attributed the dips to Coulomb losses. However, no quantitative calculations of the spectra of particles with $A \geq 3$ that would explain such dips have been performed up until now (calculations for protons were carried out by Mullan [20], Schlickeiser and Steinacker [21], and Steinacker *et al.* [22]). Such a statement of the problem for helium isotopes nevertheless took place, but the authors assumed a large τ_a/τ_c in their calculations. This yielded very soft energy spectra with no features. Steinacker *et al.* [22] also solved a similar problem with the inclusion of the same processes as in our paper. However, they put the main accent on explaining the energy dependences of the relative heavy-element abundance Fe/O and Fe/C attributable to the Coulomb losses rather than their energy spectra. Note also that, when considering the stochastic acceleration, Ryan and Lee [24] took the energy losses in the form $-(dE/dt)_c \sim p^{-1}$ for convenience of analytic solution. Clearly, this approach yields only regular changes in the spectrum shape over the entire energy range and cannot lead to a dip in a narrow interval. The correct expression for the Coulomb losses was used by Litvinenko [25], who considered their effect on the energy spectra of ^{3}He. In this paper, the possibility of spectrum steepening was analytically shown for the stochastic acceleration by ion-cyclotron waves. As we see from Figs. 1 and 2, such a steepening can actually take place in the case of acceleration by Alfvén waves as well. However, the inverse effect in our analysis, a spectrum flattening (Fig. 2) which occurs at large τ_a/τ_c, is also possible.

Note also that all of the above arguments associated with the formation of the energy distributions assume the subsequent invariability (or an insignificant change) of the spectrum of the particles after their acceleration. This assumption is correct if the other processes of energy change are insignificant. The most important of them is probably adiabatic losses as the ions propagate further in interplanetary space to the point of their detection. These losses, in turn, are small if the mean free path (λ) in the propagation region is ~0.5–1 AU. Such a value of λ is commonly observed under the conditions of the interplanetary medium.

DISCUSSION AND CONCLUSIONS

In the nonrelativistic case where the turbulence spectral index $s < 2$, the diffusion coefficients can be written as [3, 5]

$$\chi = \frac{1}{(2-s)(4-s)}\frac{1}{2\pi^2}\frac{1}{m_p}\left(\frac{Qe}{Ac}\right)^{s-2}\frac{B^s}{W_0}p^{3-s}, \quad (7)$$

$$D_p = \frac{2}{s(s+2)}\pi^2 m_p V_A^2 W_0 B^{-s}\left(\frac{Ac}{Qe}\right)^{s-2}p^{s-1}, \quad (8)$$

where c is the speed of light. Using now formulas (6)–(8) at $s = 3/2$, we obtain

$$\tau_a \approx 6\times 10^{-3}\frac{\left(\frac{n}{10^9\ \mathrm{cm}^{-3}}\right)\sqrt{\frac{l}{10^8\ \mathrm{cm}}}}{(W_T/W_B)\left(\frac{B}{100\ \mathrm{G}}\right)^{5/2}}\sqrt{\frac{A}{Q}}\ \mathrm{s}, \quad (9)$$

$$\frac{\tau_a}{\tau_d} \approx 3\times 10^{-6}\left(\frac{n}{10^9\ \mathrm{cm}^{-3}}\right)\left(\frac{l}{10^8\ \mathrm{cm}}\right)\left(\frac{10^9\ \mathrm{cm}}{L}\right)^2 \times\left(\frac{100\ \mathrm{G}}{B}\right)^2\frac{1}{(W_T/W_B)^2}\frac{A}{Q}, \quad (10)$$

$$\frac{\tau_a}{\tau_c} \approx 2\times 10^{-5}\left(\frac{n}{10^9\ \mathrm{cm}^{-3}}\right)^2\sqrt{\frac{l}{10^8\ \mathrm{cm}}}\left(\frac{100\ \mathrm{G}}{B}\right)^{5/2} \times\frac{1}{(W_T/W_B)}\sqrt{\frac{Q^3}{A}}. \quad (11)$$

Here, the quantity $W_T = \int_{k_{\min}}^{\infty} W(k)dk$ is the total turbulence energy density, and $W_B = B^2/8\pi$ is the energy density of the regular magnetic field.

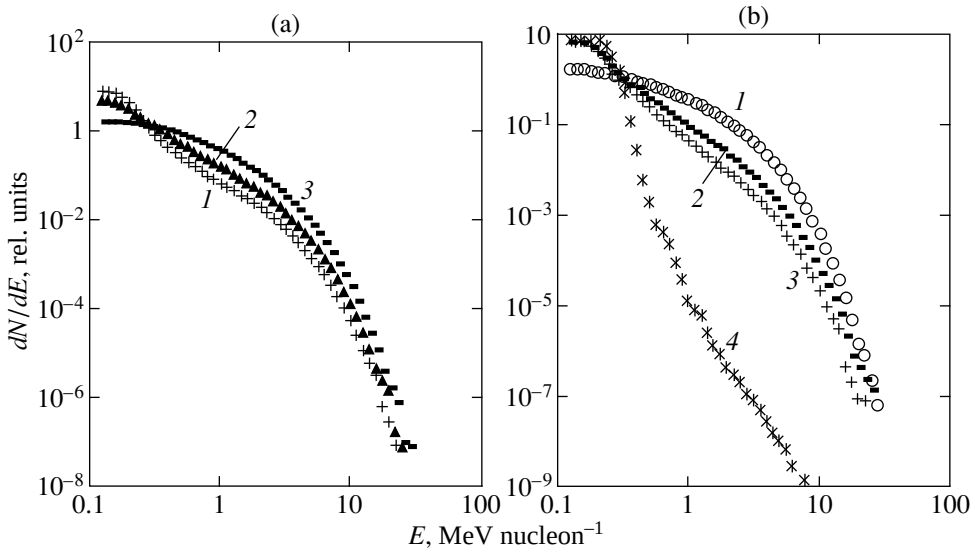

Fig. 2. Dependence of the ^{4}He spectra (a) on temperature for $\tau_a/\tau_d = 0.8$ and $\tau_a/\tau_c = 3.4$: (*1*) $T = 5 \times 10^5$ K; (*2*) $T = 10^6$ K; (*3*) $T = 2 \times 10^6$ K; and (b) on τ_a/τ_c for $T = 10^6$ K and $\tau_a/\tau_d = 0.8$: (*1*) $\tau_a/\tau_c = 2.0$; (*2*) $\tau_a/\tau_c = 4.1$; (*3*) $\tau_a/\tau_c = 4.7$; (*4*) $\tau_a/\tau_c = 14$.

If we now specify τ_a, L, and l, we can determine from formulas (9)–(11) the parameters n, B, and W_T/W_B, which describe the particle acceleration region. As an example of this approach, we computed the spectra for the SCR events of December 9–11, 1977, and December 26–27, 1978 (Fig. 3), which match the observed ones [16]. We took the following parameters in the calculations: a temperature $T \sim 1.4 \times 10^6$ K for both events, as well as $\tau_a/\tau_d = 1.0$, $\tau_a/\tau_c = 7.0$ (for ^{3}He), and $\tau_a/\tau_d = 0.6$, $\tau_a/\tau_c = 8.0$ (for ^{4}He) for the event of December 9–11; for the event of December 26–27, we took $\tau_a/\tau_d = 1.2$, $\tau_a/\tau_c = 6.0$, and $\tau_a/\tau_d = 0.6$, $\tau_a/\tau_c = 8.0$ for ^{3}He and ^{4}He, respectively. If we assume a rapid acceleration in a small volume during the impulsive phase of the flare ($\tau_a \sim 1$ c, $L \sim 10^8$ cm, and $l \sim 0.1L$), this yields $n \sim (1.4–2.4) \times 10^{12}$ cm^{-3}, $B \sim 1400–1500$ G, and $W_T/W_B \sim (3.6–8.5) \times 10^{-3}$. At the same time, for a prolonged acceleration after the impulsive phase of the flare ($\tau_a \sim 10^3$ c, $L \sim 10^{10}$ cm, and $l \sim 0.1L$), we obtain $n \sim (1.4–2.4) \times 10^9$ cm^{-3}, $B \sim 4.5–4.7$ G, and $W_T/W_B \sim (6.4–15) \times 10^{-2}$.

Thus, the features in the spectra of the accelerated particles produced by Coulomb losses allow the parameters of the particle acceleration region to be determined, because they are very sensitive to the plasma temperature and density. This can serve as a basis for diagnosing the flare plasma from the SCR energy spectra. Unfortunately, there is no much experimental evidence for the presence of such features in the spectra.

In the above estimates of the basic physical parameters for the plasma in the acceleration region, specifying the absolute values of τ_a, L, and l was important. As was mentioned above, the first of these quantities can be estimated from the temporal variation of X-ray and gamma-ray emissions from the flare regions. Currently, the characteristic time of rise in these emissions is generally believed to correspond to the acceleration time of both electrons and ions and is ≤1 s (occasionally, a more prolonged acceleration after the impulsive phase of the flare is considered). The spatial scale L of the particle acceleration region is apparently associated with magnetic arch structures, whose sizes are well determined from satellite observations. These observations yield $L \sim 10^8$–10^{10} cm. As for the main turbulence scale l, it is the most uncertain parameter in our analysis. Unfortunately, there are no experimental data on the characteristic scales of Alfvén turbulence and its spectrum in the particle acceleration region. An indirect way of determining l is its estimation from a minimum correlation time of X-ray pulsations from solar flares (see [26]). Without considering this important problem in detail, we acted here at a phenomenological level by relating l to the typical macroscopic scale of the flare region and assuming that $l \ll L$. Since the actual value of l is apparently much smaller than that we chose, the derived ratios W_T/W_B clearly represent an upper limit on the total energy of Alfvén turbulence in the flare plasma.

In conclusion, recall that the impulsive SCR events are characterized by a large electron-to-proton flux ratio in interplanetary space, which, according to the data of Cane *et al.* [27], is 0.02–10 for energies of ~10–20 MeV. The main factor determining this ratio is the conditions of escape of these particles rather than the acceleration itself, because the class of events under consideration belong to the events occurring in closed magnetic configurations. The acceleration of the plasma electron component itself requires a separate analysis, because a type of turbulence other than Alfvén turbulence must be invoked (see, e.g., [2, 28, 29]). In

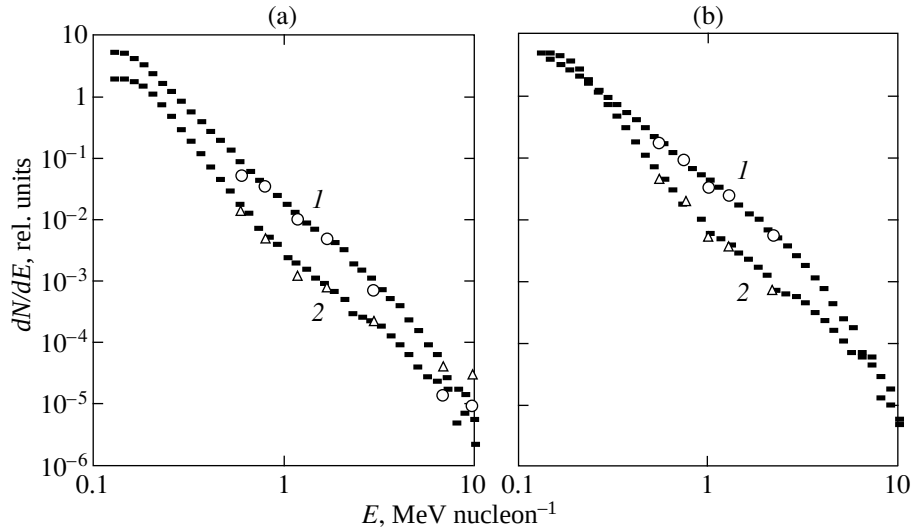

Fig. 3. Computed energy spectra of ^{3}He (curves *1*) and ^{4}He (curves *2*) for the solar events of December 9–11, 1977 (a) and December 26–27, 1978 (b) at $T = 1.4 \times 10^6$ K and the following parameters: (a) $\tau_a/\tau_d = 1.0$, $\tau_a/\tau_c = 7.0$ (for ^{3}He) and $\tau_a/\tau_d = 0.6$, $\tau_a/\tau_c = 8.0$ (for ^{4}He); (b) $\tau_a/\tau_d = 1.2$, $\tau_a/\tau_c = 6.0$ (for ^{3}He) and $\tau_a/\tau_d = 0.6$, $\tau_a/\tau_c = 8.0$ (for ^{4}He). The figure shows experimental data (circles for ^{3}He and triangles for ^{4}He) for these SCR events [16].

addition, much more physical processes than for protons (Coulomb losses, bremsstrahlung and synchrotron radiation, the generation of high-frequency plasma waves, etc.) play an important role in forming the energy spectra of these particles. In our view, it follows from the above discussion that, at the current state of the art in the development of solar-flare physics, the problems of detailed electron and ion acceleration may well be considered independently.

ACKNOWLEDGMENTS

We are grateful to the referees for their remarks that helped improve the text of the paper. This study was supported by the Russian Foundation for Basic Research (project no. 97-02-18073) and by grant no. 97-3.1-3 of the Competitive Center for Fundamental Science at the St. Petersburg State University, Ministry of General and Professional Education of the Russian Federation.

REFERENCES

1. A. A. Korchak, Solar Phys. **66**, 149 (1980).
2. J. A. Miller, P. F. Cargill, A. G. Emslie, *et al.*, J. Geophys. Res. **102**, 14631 (1997).
3. K. Hasselmann and G. Wibberenz, Zeitschrift für Geophys. **34**, 353 (1968).
4. Toptygin, I.N., *Cosmic Rays in Interplanetary Magnetic Fields* [in Russian] (Nauka, Moscow, 1983).
5. V. S. Berezinskii, S. V. Bulanov, V. L. Ginzburg, *et al.*, *Cosmic-Ray Astrophysics* [in Russian], Ed. by V. L. Ginzburg (Nauka, Moscow, 1984).
6. S. T. Butler and M. J. Buckingham, Phys. Rev. **126**, 1 (1962).
7. D. V. Sivukhin, *Problems in Plasma Theory* [in Russian] (Atomizdat, Moscow, 1964), Vol. 4, p. 81.
8. J. A. Miller and D. A. Roberts, Astrophys. J. **452**, 912 (1995).
9. R. Ramaty and N. Mandzhavidze, *High Energy Solar Phenomena—a New Era of Spacecraft Measurements*, Ed. by J. M. Ryan and W. T. Vestrand (AIP, New York, 1994), p. 26.
10. A. Achterberg and W. M. Krulls, Astron. Astrophys. **265**, L13 (1992).
11. Yu. Yu. Kartavykh, G. A. Kovaltsov, and V. M. Ostryakov, Izv. Ross. Akad. Nauk, Ser. Fiz. **59**, 201 (1995).
12. Yu. Yu. Kartavykh, G. A. Kovaltsov, and V. M. Ostryakov, in *Proceedings of 24 ICRC* (Rome, 1995), Vol. 4, p. 26.
13. Yu. Yu. Kartavykh, V. M. Ostryakov, I. Yu. Stepanov, *et al.*, Kosm. Issled. **36**, 465 (1998).
14. M. A. Forman, E. Ramaty, and E. G. Zweibel, *Physics of the Sun*, Ed. by P. A. Sturrock (1986), Vol. II, p. 249.
15. V. M. Ostryakov and M. F. Stovpyuk, Astron. Zh. **74**, 440 (1997).
16. E. Möbius, M. Scholer, D. Hovestadt, *et al.*, Astrophys. J. **259**, 397 (1982).
17. J. E. Mazur, G. M. Mason, B. Klecker, *et al.*, Astrophys. J. **401**, 398 (1992).
18. D. V. Reames, I. G. Richardson, and K.-P. Wenzel, Astrophys. J. **387**, 715 (1992).
19. G. M. Mason, J. E. Mazur, and D. C. Hamilton, Astrophys. J. **425**, 843 (1994).
20. D. J. Mullan, Astrophys. J. **237**, 244 (1980).
21. R. Schlikeizer and J. Steinacker, Solar Phys. **122**, 29 (1989).
22. J. Steinacker, U. Jaekel, and R. Schlikeiser, Astrophys. J. **415**, 342 (1993).

23. L. G. Kocharov and Ya. V. Dvoryanchikov, *Energetic Particles and Photons of Solar Flares* [in Russian], Ed. by G. E. Kocharov (FTI RAN, Leningrad, 1984), p. 63.

24. J. M. Ryan and M. A. Lee, Astrophys. J. **368**, 316 (1991).

25. Yu. E. Litvinenko, *High Energy Solar Physics*, Ed. by R. Ramaty *et al.* (AIP, New York, 1996), p. 498.

26. S. V. Bulanov and V. A. Dogel, Izv. Akad. Nauk SSSR, Ser. Fiz. **47**, 1708 (1983).

27. H. V. Cane, R. E. McGuire, and T. T. von Rosenvinge, Astrophys. J. **301**, 448 (1986).

28. T. N. LaRosa, R. L. Moore, J. A. Miller, *et al.*, Astrophys. J. **467**, 454 (1996).

29. B. T. Park, V. Petrosian, and R. A. Schwartz, Astrophys. J. **489**, 358 (1997).

Translated by G. Rudnitskii

Astronomy Letters, Vol. 26, No. 2, 2000, pp. 61–66. Translated from Pis'ma v Astronomicheskiĭ Zhurnal, Vol. 26, No. 2, 2000, pp. 83–89.

Tidal Structures of $z \sim 1$ Galaxies in the Hubble Deep Field

V. P. Reshetnikov*

Astronomical Institute, St. Petersburg State University, Bibliotechnaya pl. 2, Petrodvorets, 198904 Russia

Received December 29, 1998; in final form, May 20, 1999

Abstract—An analysis of the images of objects in the Northern Hubble Space Telescope Deep Field has revealed twelve galaxies with tidal tails at redshifts from 0.5 to 1.5. The integrated characteristics of the newly discovered tidal structures are found to be similar to those of the tails of local interacting galaxies. The space density of galaxies with tidal tails is found to depend on z as $(1+z)^{4\pm1}$ ($q_0 = 0.05$), according to the data on objects with $z = 0.5$–1.0. The exponent decreases to 3.6 if barred galaxies are included. The change in the rate of close encounters between galaxies of comparable masses (i.e., those that produce extended tidal structures) is estimated. If the rate of galactic mergers is governed by the same process, our data are indicative of the rapid evolution of galaxy merger rate toward $z \sim 1$. © *2000 MAIK "Nauka/Interperiodica".*

1. INTRODUCTION

Gravitational interaction with the ambient medium is a major factor of galaxy evolution. Interactions between galaxies and mergers are relatively rare events at present epoch: Less than 5–10% of all galaxies are members of interacting systems [1, 2].[1] However, such processes were much more intense in the past, as evidenced by both direct analysis of the morphology of distant objects and by various statistical studies (see, e.g., [5]).

The key problem in understanding the role of interaction in galaxy evolution is knowledge of the rate of interactions and mergers at different epochs. The z dependence of this rate is usually parameterized in the form of a power-law relation, $(1+z)^{\alpha}$ [6]. Recent studies yield α ranging from 1 to 4 with ~3 considered to be the most probable value [5]. The rate of galaxy mergers was usually determined by analyzing the occurrence of close galaxy pairs at different z [7, 8] and studying the spatial and angular correlation functions (see, e.g., [9]). There is another (morphological) approach, which consists in analyzing the morphology of distant objects with the aim of directly determining the fraction of interacting and merging galaxies (see, e.g., [10]). A modification of this method is statistical analysis of samples with different z consisting of peculiar galaxies whose structure is due to gravitational interaction and external accretion: ring galaxies [11], galaxies with polar rings [12], etc.

In this paper, we report the results of statistical analysis of galaxies with tidal tails located at $z \sim 1$. (Bars have, on the average, lower surface brightness [13] and are identified less clearly, especially in distant galaxies.) Tidal interactions (and tails in particular) are relatively short-lived ($\leq 10^9$ yr) structures that form from peripheral galaxy regions during interaction or merger events. Interaction between galaxies of comparable mass is required to produce extended conspicuous tidal tails [14]. Extended tidal features have usually low surface brightness and are therefore difficult to observe. However, tidal formations are clear indicators of recent gravitational perturbation of the galaxy and it is therefore important to use the data for these formations to estimate the interaction rate during earlier epochs. As shown in [15], the tidal features should remain readily visible in Hubble Space Telescope images out to redshifts of ~1.

2. GALAXY SAMPLE

To analyze the occurrence rate of galaxies with tidal features located at $z \sim 1$, we studied the Northern Hubble Space Telescope Deep Field [16], hereafter referred to as NHDF. NHDF is an image of a small (~6 arcmin^2) field obtained with the F300W, F450W, F606W, and F814W filters (average wavelengths of 2942, 4519, 5934, and 7924 Å, respectively) that is open for public use. A detailed analysis of NHDF *I*-band frames (F814W, hereafter *I*) allowed us to select a total of about 40 objects exhibiting structures similar to tidal tales and bars in local interacting galaxies. A detailed analysis of the images of these galaxies combined with the corresponding redshift data yielded twelve candidate objects with tidal tails in the redshift interval $z = 0.5$–1.5 (Fig. 1). The sizes of the newly identified tidal features are comparable to the optical diameters of galaxies: $d_{\rm tail}/d_{\rm galaxy} = 1.4 \pm 0.7(\sigma)$, and the corresponding ratio for the tails of local interacting galaxies studied in [17] is 1.1 ± 0.8.

The table summarizes the integrated parameters of the objects of our sample. The first column gives the

[1] Note that "small-scale" interactions—between a galaxy and its low-mass satellites—are much more common. For example, the Milky Way Galaxy now interacts with a number of dwarf galaxies [3, 4].

* e-mail: resh@astro.spbu.ru

Parameters of galaxies in the Deep Field

Galaxy (1)	I_{F814W} (2)	B/D (3)	z_{ph} (4)	M_B (5)	h, kpc (6)	$\mu(I)$ (7)	$\mu(B)$ (8)
2-575.0	25.59	0.11	0.52 0.55	–15.4	0.5	25.9	25.1
2-856.0	25.24	0.85	0.96 0.96	–17.7	0.9	26.0	23.9
3-37.0	24.28		0.92 0.93	–18.5		25.7	23.7
3-79.0	24.29	0.0	1.16 1.04	–19.5	1.25	26.2	23.3
3-239.0	25.81	0.67	1.40 1.15	–19.0	2.9	26.2	22.4
3-404.1	24.61	0.37	0.80 1.07	–17.6	1.7	25.7	24.1
3-670.0/1	24.97	0.0	0.76 0.73	–17.1	0.4	26.6	25.1
3-712.0	25.08	0.18	0.68 0.48	–16.7	1.0	25.6	24.3
3-888.0/1	24.26	0.69	1.12 1.09	–19.4	2.8	25.4	22.6
3-908.1	23.93	0.0	0.48 0.48	–16.9	1.5	25.3	24.7
4-322.1	25.28	0.15	1.44: 1.41	–19.7:	1.4:	25.6	21.6:
4-522.0	25.30	0.14	1.04 1.24	–18.0	1.0	25.7	23.3

name of the galaxy according to [16]; the second column, the total magnitude in the *I* band of the *A*B system[2] [19] (we adopted the magnitude of the 3-37.0 galaxy from [20]); the third column, the observed *I*-band bulge-to-disk luminosity ratio, B/D, according to [19]. The average ratio for the galaxies considered is B/D = 0.3, which is typical of Sb-type galaxies [21].

The fourth column of the table gives the estimated photometric redshifts (spectroscopic data are unavailable) for the sample galaxies according to [20]. The latter authors used seven-color *UBVRIJHK* photometry (the first row) to infer *z*. (The redshift of 4-322.1 is marked by a colon because it refers to the neighboring 4-322.2 galaxy). The second row gives redshift estimates for each object inferred from empirical relationships between the galaxy color indices and spectroscopic redshifts [22]. The average difference of the redshifts *z* estimated by two methods is $\Delta z \approx 0.01 \pm 0.14(\sigma)$ for the galaxies considered. The scatter seems to reflect the actual accuracy of photometric redshifts for individual galaxies, which is quite sufficient for various statistical analyses.

The fifth column of the table gives the *B* band absolute magnitudes of program galaxies in the local (rest) frame inferred from apparent *I*-band magnitudes in accordance with [23]:

$$M_B = I - 5\log(D_L/10\,\mathrm{pc}) + 2.5\log(1+z) + (B-I_z) + 0.17,$$

where

$$D_L = \frac{c}{H_0 q_0^2}[q_0 z + (q_0 - 1)(\sqrt{2q_0 z + 1} - 1)] \quad (1)$$

is the photometric distance [24]; *c*, the speed of light; H_0, the Hubble constant (hereafter we adopt H_0 = 75 km s^{-1} Mpc^{-1}); and q_0, the deceleration parameter ($q_0 = 0.05$). Term $B - I_z$ in the formula for M_B is a correction that allows the *B* magnitude to be inferred from the *I* magnitude of an object with redshift *z* (see Fig. 1 in [23]). In our computations we adopted the $B - I_z$ correction for Sbc galaxies and redshifts *z* from [20]. The sixth column gives the exponential scale lengths (h) of galaxy disks as inferred in [19]. The mean values of these parameters—$\langle M_B \rangle = -18.0 \pm 1.3$ and $\langle h \rangle = 1.4 \pm 0.8$ kpc—are typical of relatively compact and not too massive galaxies.

3. PARAMETERS OF TIDAL TAILS

The faint structures emerging from the galaxies under study do not guarantee that these features are actually tidal tails and not, for example, random projections of more distant galaxies. To determine the nature of the features identified, we performed their photometry within circular apertures centered on the brightest regions of the candidate tails. The seventh column of the table gives the observed *I*-band surface brightness of the features measured. The eighth column gives the rest-frame *B*-band surface brightness inferred from observed $\mu(I)$ computed in accordance with [25]:

$$\mu(B) = \mu(I) - 2.5\log(1+z)^3 + (B - I_z) + 0.17.$$

The second term on the right-hand side of this formula characterizes the cosmological decrease of surface brightness and the third term, the color correction (see Section 2). The color indices of tidal tails of local interacting galaxies are close to those of late-type spirals [13, 17]. We therefore computed $\mu(B)$ using the $B - I_z$ corrections for Sbc-type galaxies (see [23]).

The mean rest-frame surface density of candidate tidal tails is $\langle \mu(B) \rangle = 23.7 \pm 1.0$, which agrees with the result for local interacting galaxies obtained in a similar way, $\langle \mu(B) \rangle = 23.8 \pm 0.8$ [17].

Figure 2a shows the distribution of $\mu(I)$ for candidate tidal tails in our sample compared with the $\mu(B)$ distribution for local interacting galaxies according to [17]. The figure clearly demonstrates the effect of observational selection on the choice of tidal features in the Deep Field: The $\mu(I)$ distribution exhibits a peak at $\mu(I) \approx 25.5$ followed by a decrease when passing to the features with lower surface brightness. Figure 2b shows the computed rest-frame *B*-band surface brightness (dashed line). As is evident from the figure, the candidate tidal features in the Deep Field occupy more or less the same surface brightness interval as the tails of local interacting galaxies. Observational selection in Fig. 2b manifests itself in the fact that the tidal tails of

[2] The *B* and *I* magnitudes in the AB system of [18] are related to the standard *B*, *I* magnitudes by $B_{AB} = B - 0.17$ and $I_{AB} = I + 0.48$.

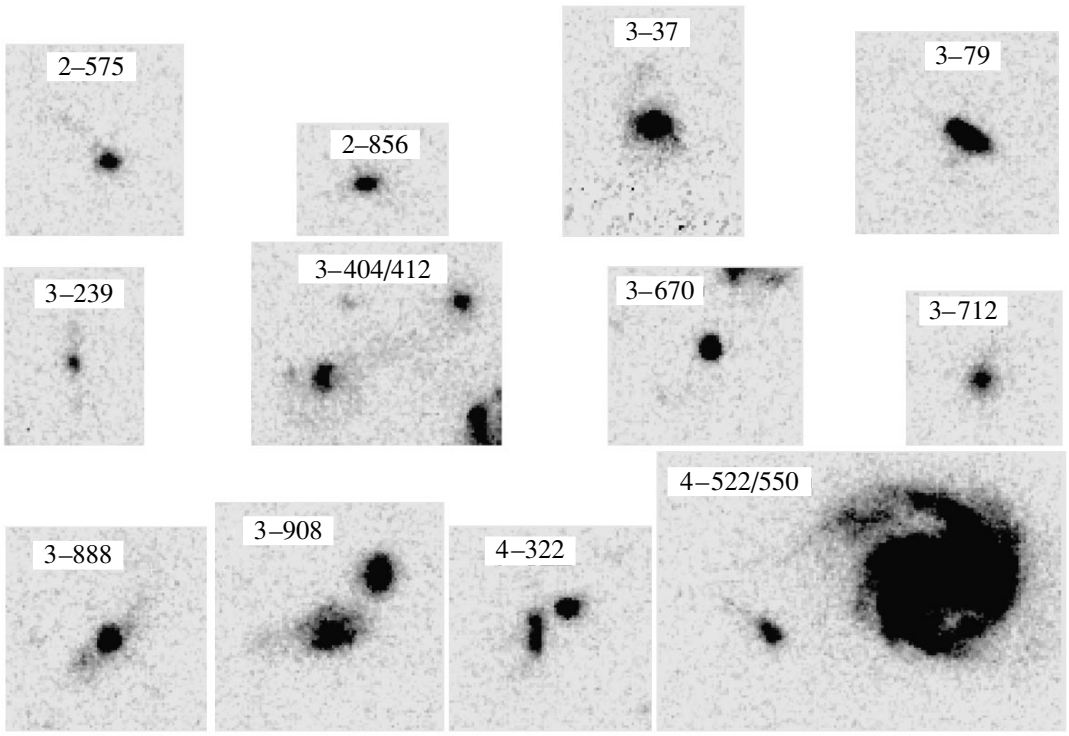

Fig. 1. A reproduction of galaxies with presumed tidal tails in the Hubble Deep Field. Images based on *I*(F814W)-band Deep Field frames. Image size is $17\farcs2 \times 11\farcs8$ arcsec^2, orientation is arbitrary.

galaxies located at z = 0.5–1.0 are concentrated on the right-hand side of the graph outlined by the solid line ($\mu(B)$ = 23.5–25.5), whereas only the tidal tails with very high surface brightness ($\mu(B)$ = 21.5–23.5) could be identified in more distant galaxies at z = 1.0–1.5. Clearly, our sample of galaxies with tidal tails is much more complete in the z = 0.5–1.0 interval (seven objects) than in the z = 1.0–1.5 interval (five galaxies).

4. REDSHIFT DEPENDENCE OF THE SPACE DENSITY OF GALAXIES WITH TIDAL TAILS

As was noted above, the morphological and photometric parameters of the candidate galaxies with tidal tails in the Deep Field are similar to those of local tidal features. This similarity makes the parameters in question a potentially useful tool for estimating the redshift dependence of the space density of this class of galaxies (and, consequently, of the rate of interactions resulting in the formation of tails). To this end, we used the method suggested by Lavery [11] and later by Reshetnikov [12] to estimate the space density at $z \sim 1$ of ring and polar ring galaxies, respectively.

The volume element can be written as a function of redshift z (see, e.g., [26]):

$$dV = \frac{c}{H_0}(1+z)^{-2}\frac{D_L^2}{E(z)}d\Omega dz, \qquad (2)$$

where D_L is the photometric distance [see (1)] and

$$E(z) = (1+z)\sqrt{2q_0 z + 1}$$

if the cosmological constant $\Lambda = 0$. We adopted the following standard (power-law) redshift dependence of the space density of galaxies with tidal fields:

$$n(z) = n_0(1+z)^{\alpha}, \qquad (3)$$

where $n_0 = n(z = 0)$ is the local space density of such galaxies. The expected number of objects of the type considered within solid angle $d\Omega$ and given interval of redshifts z can be estimated by integrating equations (2) and (3) over z.

According to [27], the proportion of galaxies with tails among the members of binary systems is 94/974 ≈ 0.1. On the other hand, physical pairs contain only ~0.1 of all galaxies in the local Universe [27]. Therefore, if most of the present-epoch galaxies with tidal tails are located in binary systems [28], the proportion of such galaxies is $\sim 0.1 \times 0.1 = 0.01$. To estimate the total number of galaxies in the surrounding Universe, we used the galaxy luminosity function by Marzke *et al.* [29]. The parameters of the luminosity function (i.e., the parameters of the Schechter function fit) are: $M_B^* = -20.05$, $\phi^* = 5.4 \times 10^{-3}$ Mpc^{-3}, and $\beta = -0.12$. We integrated the luminosity function between $M_B = -15.4$ and -19.7 (see table) and found that the galaxy space density is 0.025 Mpc^{-3}. Therefore, $n_0 = 0.01 \times 0.025 = 2.5 \times 10^{-4}$ Mpc^{-3}. The area

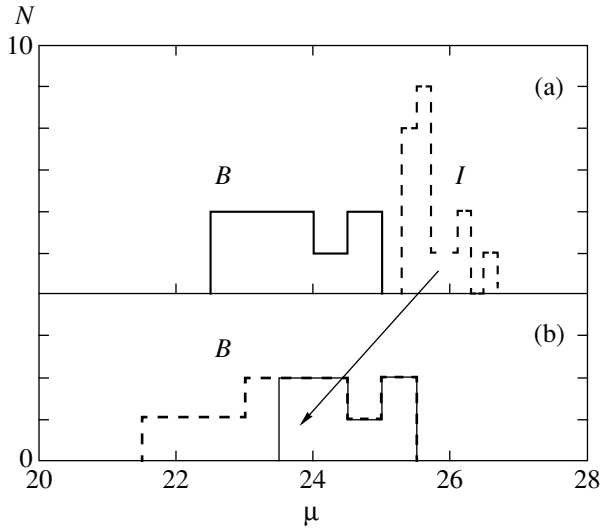

Fig. 2. (a) Distribution of the observed surface brightness of tidal tails of the Deep-Field galaxies: *I* filter (dashed line) and *B* filter (solid line). (b) The same distribution for Deep-Field galaxies transformed into the rest-frame *B*-band surface brightness. The arrow connects the initial and transformed distributions.

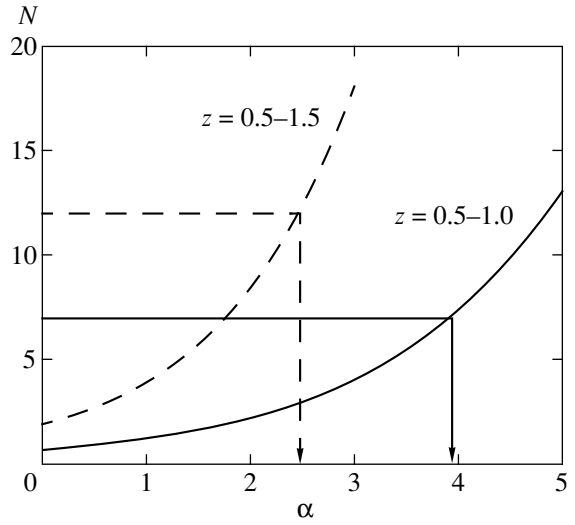

Fig. 3. The expected number of galaxies with tidal tails in the Deep Field as a function of α for two redshift intervals: 0.5–1.0 (solid line) and 0.5–1.5 (dashed line).

of the Deep field portion searched for tidal features is 5.59 arcmin^2; i.e., the solid angle is $\Omega = 4.73 \times 10^{-7}$ sr.

We found the expected number of galaxies with tidal tails in different redshift intervals as a function of exponent α. Solid line in Fig. 3 shows how the number of z = 0.5–1.0 galaxies in the Deep Field depends on exponent α. As is evident from the figure, seven observed objects imply α = 4.0. We now assume that the distribution of the number of galaxies with tidal fields obeys the Poisson law and estimate the standard error of the number of observed galaxies as $\pm\sqrt{7} = 2.65$. This error translates into a scatter of (+0.53, –0.80) in exponent α. The actual error (e.g., due to the uncertainty in n_0)[3] can be much larger and must be as high as ±1. Note that two potential error sources—underestimation of n_0 and of the number of galaxies with tails in the Deep Field because of the surface-brightness selection—introduce opposite biases in α and partly cancel each other. The entire sample (12 galaxies) covering the z = 0.5–1.5 interval yields α = 2.5 (+0.3, –0.5). This value, however, must be considered only as a lower limit because observational selection increases at $z \geq 1$ (see Section 3). (α = 4.0 would imply about 30 more galaxies with tidal tails in the z = 1.0–1.5 interval within the Deep Field).

The exponent α thus inferred depends on the adopted cosmological model. For instance, adopting $q_0 = 0.5$ ($\Omega = 2q_0 = 1.0$) would result in a smaller spatial volume and, consequently, in higher inferred exponent α = 5.0 (for z = 0.5–1.0). Nonzero cosmological constant decreases α, e.g., α = 3.4 (z = 0.5–1.0) for $\Omega_\Lambda = 0.7$ and $\Omega_m = 0.3$ ($\Omega = \Omega_\Lambda + \Omega_m = 1.0$) α = 3.4 ($z$ = 0.5–1.0).

To verify the high value of exponent α inferred here, we included barred galaxies in our analysis. We found only four such galaxies in the redshift interval z = 0.5–1.0, and this number implies α = 3.1 (+0.7, –1.2). (We adopted the proportion n_0 of barred galaxies in the local Universe from [27]). Galaxy bars are characterized by lower surface brightness compared to tidal tails [13], and therefore the statistical analyses of these objects yield less reliable estimates for exponent α. The combined sample of galaxies with tidal features (tails + bars) contains a total of 11 objects in the z = 0.5–1.0 interval and yields α = 3.6 (+0.5, –0.6).

5. RESULTS AND DISCUSSION

We analyzed the object images in the Hubble Deep Field and identified a total of 12 candidate galaxies with tidal tails in the redshift interval z = 0.5–1.5. We found the integrated parameters of the tidal features discovered to be similar to those of the tails of local interacting galaxies. We analyzed the data on z = 0.5–1.0 objects and found that the space density of galaxies with tidal tails depends on z as $(1 + z)^\alpha$, where $\alpha = 4 \pm 1$. (The inclusion of barred galaxies has little effect on the inferred exponent α, decreasing it to α = 3.6.) We thus estimated the redshift dependence of the rate of close encounters of galaxies of comparable masses, which are responsible for the formation of tidal tails. If the same process characterizes the merger rate, then our results imply very fast evolution of the galaxy merger rate toward $z \sim 1$. Our result refers to field galaxies, because the Hubble Deep Field was selected in such a way as to avoid distant clusters.

How does our estimate agree with the results of other authors and with theoretical computations? Abraham [5] summarized in his review the observational

[3] A 50% increase of the local space density of galaxies with tidal tails causes α to decrease to 3.3.

evidence for the fact that the galaxy merger rate varies as $(1 + z)^3$ at $z \leq 1$. These data are at variance with the results of recent works (see, e.g., [9, 30–33]) whose authors inferred $\alpha \leq 2$ using various techniques. The discrepancies can be due to various effects. The latter include the poorly understood relation between the redshift dependence of the space density of close galaxy pairs and the merger rate, systematic errors involved in comparing the local and distant-Universe proportions of galaxies in the physical pairs (e.g., due to different selection effects in the samples considered), real spatial variations of the merger rate, etc.

Theoretical computations also fail to give a clear picture. For instance, Lacey and Cole [34] showed that the hierarchically merging halo model implies that the recent merger rate for massive galaxies varied with $\alpha \sim 1$. Carlberg [6] found the merger rate in CDM-like cosmological models to depend on the geometry of the Universe: $\alpha \approx 4.51 \cdot \Omega^{0.42}$, where $\Omega = 2q_0$. In view of the decrease in the mean galaxy mass at earlier epochs, the above formula should be modified as $\alpha \approx 3.2 \cdot \Omega^{0.57}$ [35], implying $\alpha \approx 1$ for $q_0 = 0.05$ and $\alpha \approx 3$ for $q_0 = 0.5$. The dependence of the galaxy merger and interaction rate on the geometry of the Universe was also illustrated by Governato *et al.* [36]. The above authors found that $\alpha = 2.5 \pm 0.42$ for CDM model with $q_0 = 0.15$ and $\alpha = 4.2 \pm 0.28$ for $q_0 = 0.5$. Therefore, despite the discrepancy between the current theoretical estimates, they predict high exponents α for cosmological models whose mean density is close to the critical density and relatively low rate of mergers and interactions at large z for $q_0 \ll 0.5$. The observational estimates of exponent α is thus an interesting cosmological test.

An exponent $\alpha \leq 2$ in the redshift dependence of the rate of galaxy mergers and interactions would imply (see Fig. 3) that there must be no more than two galaxies with tidal tails in the redshift interval $z = 0.5$–1.0. This is clearly at variance with the number of actually observed objects. This discrepancy can be resolved by assuming that the proportion of close galaxy encounters, which result in tidal features but not mergers, increases with z. For instance, Dubinski *et al.* [37] showed that at fixed impact parameters, the parameters of tidal tails (in particular, their sizes) are determined by the mass and distribution of dark matter. Lower average masses of dark halos at $z \sim 1$ could therefore explain the excess of tidal tails in distant objects.

Note finally that the number of galaxies with identified tidal tails is too small to allow any definitive conclusions to be reached about the redshift dependence of the space density of such objects[4]. However, the results that we report in this paper suggest that analyses of tidal features and morphological studies of distant galaxies can become important tools for estimating the galaxy interaction and merger rate at intermediate z.

[4] A preliminary analysis of the Southern Hubble Deep Field yielded approximately the same number of galaxies with tidal tails as in the Northern Field. This means that exponent α inferred from the two fields will remain close to the value inferred from the Northern Deep Field alone.

ACKNOWLEDGMENTS

This study was supported by the Integration program (project no. 578) and the Competitive Center for Fundamental Science of the Ministry of General and Professional Education of the Russian Federation and the Russian Foundation for Basic Research (project nos. 97-02-18212 and 98-02-18178).

REFERENCES

1. A. V. Zasov, Astrofizika **4**, 427 (1968).
2. I. D. Karachentsev and V. Yu. Terebizh, Astrofizika **4**, 443 (1968).
3. M. E. Putman, B. K. Gibson, L. Stiavely-Smith, *et al.*, Nature **394**, 752 (1998).
4. M. Mateo, E. W. Olszewski, and H. L. Morrison, Astrophys. J. Lett. **508**, L55 (1998).
5. R. G. Abraham, *Galaxy Interactions at Low and High Redshifts*, Ed. by J. E. Barnes and D. B. Sanders (Kluwer Acad., Dordrecht, 1998), p.11.
6. R. G. Carlberg, Astrophys. J. Lett. **359**, L1 (1990).
7. S. E. Zepf and D. C. Koo, Astrophys. J. **337**, 34 (1989).
8. J. M. Burkey, W. C. Keel, R. A. Windhorst., *et al.*, Astrophys. J. Lett. **429**, L13 (1994).
9. L. W. Neuschaefer, M. Im, K. U. Ratnatunga, *et al.*, Astrophys. J. **480**, 59 (1997).
10. R. G. Abraham, N. R. Tanvir, B. X. Santiago, *et al.*, Mon. Not. R. Astron. Soc. **279**, L47 (1996).
11. R. J. Lavery, P. Seitzer, N. B. Suntzeff, *et al.*, Astrophys. J. Lett. **467**, L1 (1996).
12. V. P. Reshetnikov, Astron. Astrophys. **321**, 749 (1997).
13. J. M. Schombert, J. F. Wallin, and C. Struck-Marcell, Astron. J. **99**, 497 (1990).
14. A. Toomre and J. Toomre, Astrophys. J. **178**, 623 (1972).
15. J. E. Hibbard and W. D. Vacca, Astron. J. **114**, 1741 (1997).
16. R. E. Williams, B. Blacker, M. Dickinson, *et al.*, Astron. J. **112**, 1335 (1996).
17. V. P. Reshetnikov, Pis'ma Astron. Zh. **24**, 189 (1998).
18. J. B. Oke, Astrophys. J., Suppl. Ser. **27**, 21 (1974).
19. F. R. Marleau and L. Simard, Astrophys. J. **507**, 585 (1998).
20. A. Fernández-Soto, K. M. Lanzetta, and A. Yahil, Astrophys. J. **513**, 34 (1999).
21. F. Simien and G. de Vaucouleurs, Astrophys. J. **302**, 564 (1986).
22. Y. Wang, N. Bahcall, and E. L. Turner, Astron. J. **116**, 2081 (1998).
23. S. J. Lilly, L. Tresse, F. Hammer, *et al.*, Astrophys. J. **455**, 108 (1995).
24. W. Mattig, Astron. Nachr. **284**, 109 (1958).
25. S. Lilly, D. Schade, R. Ellis, *et al.*, Astrophys. J. **500**, 75 (1998).

26. P. J. E. Peebles, *Principles of Physical Cosmology* (Princeton Univ., Princeton, 1993).
27. I. D. Karachentsev, *Double Galaxies* (Nauka, Moscow, 1987).
28. A. Toomre, *The Evolution of Galaxies and Stellar Populations*, Ed. by B. M. Tinsley and R. B. Larson (Univ. Observ., New Haven, 1977), p. 401.
29. R. O. Marzke, L. N. da Costa, P. S. Pelligrini, *et al.*, Astrophys. J. **503**, 617 (1998).
30. D. Woods, G. G. Fahlman, and H. B. Richer, Astrophys. J. **454**, 32 (1995).
31. W. C. Keel and W. Wu, Astron. J. **110**, 129 (1995).
32. N. Roche and S. A. Eales, astro-ph/9803331 (1998).
33. W. Wu and W. C. Keel, Astron. J. **116**, 1513 (1998).
34. C. Lacey and S. Cole, Mon. Not. R. Astron. Soc. **262**, 627 (1993).
35. R. G. Carlberg, C. J. Pritchet, and L. Infante, Astrophys. J. **435**, 540 (1994).
36. F. Governato, J. R. Gardner, J. Stadel, *et al.*, astro-ph/9710140 (1997).
37. J. Dubinski, C. Mihos, and L. Hernquist, Astrophys. J. **462**, 576 (1996).

Translated by A. Dambis

Astronomy Letters, Vol. 26, No. 2, 2000, pp. 67–76. Translated from Pis'ma v Astronomicheskiĭ Zhurnal, Vol. 26, No. 2, 2000, pp. 90–101.

Burning Regimes for Thermonuclear Supernovae and Cosmological Applications of SNe Ia

E. I. Sorokina[1]*, S. I. Blinnikov[1, 2], and O. S. Bartunov[1]

[1] *Sternberg Astronomical Institute, Universitetskiĭ pr. 13, Moscow, 119899 Russia*
[2] *Institute of Theoretical and Experimental Physics, ul. Bol'shaya Cheremushkinskaya 25, Moscow, 117259 Russia*

Received June 16, 1999

Abstract—The method of multigroup radiation hydrodynamics is used to compute light curves for thermonuclear supernovae. Opacities are computed by taking into account spectral lines and expansion. *UBVI* fluxes are predicted. Our computed times of brightness rise to a maximum in *B* and *V* have been found to agree with observations better than those of other authors. The validity of our results is justified physically. The nuclear burning regime is shown to affect significantly the slope of the light curve in *B* and, to a slightly lesser extent, in *V*. If the prevailing burning regime during supernova explosions changed with age of the Universe, then the conclusion about a positive cosmological constant Λ drawn from observations of Type Ia supernovae may prove to be wrong. *© 2000 MAIK "Nauka/Interperiodica".*

INTRODUCTION

Type Ia supernovae (SNe Ia) have long been recognized to be among the most convenient objects for measuring distances and determining the geometry of the Universe [1]. There are several reasons for this. First, these are extremely luminous objects; fairly rich information about SNe Ia can be obtained even if they explode in very distant galaxies with large redshifts *z*. Second, judging by their spectra and the shapes of the light curves, SNe Ia seem to be quite a homogeneous class at first glance. However, a closer examination reveals clear differences within this class of objects.

Pskovskii [2] showed that there was a relationship between the peak luminosity of SNe Ia and the rate of subsequent brightness decline. Subsequently, this relationship was intensively studied by many researchers of SNe Ia using observations of nearby supernovae with small *z* [3–5].

In recent years, the observing techniques have reached a level that it became possible to detect and study supernovae with large redshifts. The first results were obtained by Nørgaard-Nielsen *et al.* [6]: In several years of observations with a 1-m telescope in Chile, they discovered only two supernovae with $z \sim 0.3$.

There are presently several groups of researchers in the world which observe distant supernovae with the largest ground-based telescopes and the Hubble Space Telescope. The observing techniques have developed to an extent that each group can discover ten or more supernovae with large *z* in two weeks of scheduled observations. The work of these groups made it possible to estimate various cosmological parameters from observations of distant supernovae: the Hubble constant H_0, the relative density of matter Ω_m, and the vacuum energy Ω_Λ, as well as to calculate such quantities inferred from them as the deceleration parameter *q* of the Universe, the ratio of local H_0 to global one, etc. For example, Kim *et al.* [7] estimated H_0 from the first seven SNe Ia with $z \geq 0.35$ and refuted the hypothesis that the local value of H_0 exceeds appreciably its mean. Perlmutter *et al.* [8] used the same data to estimate the possible matter-to-vacuum density ratio.

Several more interesting studies have recently been carried out using slightly larger samples of distant supernovae [9–13]. These studies yielded an unexpected result: An analysis of observational data strongly suggests that the Universe is currently expanding with acceleration.

Note, however, that all studies on distant supernovae used the "peak luminosity–brightness decline rate" relations inferred by analyzing nearby objects, but the deviations of individual objects from such a relation cannot be explained by observational errors alone even for nearby SNe Ia.

The slowdown in brightness decline with increasing peak luminosity can be theoretically explained by the fact that both these factors are determined mainly by the amount of ^{56}Ni produced during the explosion. The peak brightness of SNe Ia is determined by the amount of ^{56}Ni, because the light curve is mainly shaped by its radioactive decay. On the other hand, a large amount of nickel must greatly increase the opacity of matter. It takes a longer time for the radiation to diffuse through the stellar matter, and the slope of the light curve becomes gentler. However, the descent on the light

* e-mail: sorokina@sai.msu.su

curve is explained not only by the amount of nickel but also by its distribution (and the distribution of other heavy elements) inside a freely expanding star, as well as by the expansion velocity of the matter. These distribution and velocity, in turn, depend on how the burning propagated through the star.

The theory of burning in supernovae has been intensively developed since the studies by Arnett [14], Ivanova *et al.* [15], and Nomoto *et al.* [16]. Many models have been proposed for the explosions of SNe Ia (see, e.g., [17, 18] and references therein) with various (Chandrasekhar and sub-Chandrasekhar) masses, various burning regimes (detonation, deflagration, and their various combinations), various explosion energies and expansion velocities of matter. Since the chemical elements are produced by burning in different ratios and have different distributions over the star in these theoretical models, calculations of the subsequent supernova evolution yield different theoretical light curves. By comparing the computed and observed light curves, we can judge precisely which explosion models are preferred in nature. It is probably the realization of different supernova explosion scenarios that leads to a scatter in the relations between the observed explosion parameters and explains the existence of objects which deviate from these relations by an amount exceeding the observational errors.

In this paper, we compute light curves for two widely known models of SNe Ia: W7 [19] and DD4 [20]. The models contain a similar amount of ^{56}Ni, but it was produced in different burning regimes and, consequently, has a different distribution. A new result is that, for similar absolute magnitudes at maximum light, the supernovae exploded in these two ways behave completely differently after the maximum. In model W7, the *B* brightness declines too slowly and is inconsistent with observations of typical SNe Ia. We discuss reasons for the difference between our light curve for this model and the light curves computed by other authors.

While exploring the possibility of using SNe Ia in cosmology, we infer that the currently available statistics of distant supernovae do not allow firm conclusions about the geometry of the Universe to be drawn. Ground-based experiments show that the burning regime during an explosion cannot always be accurately predicted in advance. The situation is similar for supernovae: It may well be that a difference in the initial conditions changes only the probability that the burning will follow a particular way but does not determine it exactly. Since the burning regime strongly affects the shape of the light curve, the decline rate cannot be reliably predicted given the initial conditions alone. The probability of a particular brightness decline rate, which plays such an important role in determining the cosmological parameters, can be ascertained only by accumulating sufficiently large observational statistics of SNe Ia at different *z*.

METHOD OF CALCULATIONS

We used the approximation of multigroup radiation hydrodynamics to model the light curves. All calculations were performed with the STELLA code [21, 22] by assuming local thermodynamic equilibrium (LTE) for level populations and for ionization states.

The STELLA code solves differential equations for the angular moments of intensity averaged over fixed frequency bands. In our calculations, we used as many as 200 Lagrangian zones in mass and as many as 100 groups in frequency. Such a large number of energy zones allows the nonequilibrium continuum radiation to be computed fairly accurately. In this case, there is no need to assign a temperature to the radiation: The photon energy distribution can be arbitrary.

A simultaneous solution of the hydrodynamic equations and transfer equations for all frequencies allows us to determine the photometric fluxes in self-consistent calculations, when no additional estimates of the thermalization depth (as in single-group models) are required. When solving the set of equations, we also calculate the variable Eddington factors in which the scattering and the Doppler effect for each frequency group in each mass zone were properly taken into account. We compute the gamma-ray transfer and allow for the nonlocal absorption of the energy released during radioactive decay of nuclei in the single-group approximation. Here, we follow [23] and treat the gamma-ray opacity as pure absorption. The above authors considered this issue in detail by using, in particular, the model of thermonuclear supernova W7 and showed this approximation to be excellent: The gamma-ray deposition depends only slightly on optical depth, so the computational error in the heating rate does not exceed 10% within $t = 1200$ days after the explosion if the effective opacity is assumed to be $\kappa_\gamma = 0.050Y_e$ (Y_e is the total number of electrons per baryon).

The equation of state includes equilibrium ionization and recombination. The line opacity was treated according to [24] as the opacity during expansion.

The principal limitation of our code for modeling the light curves is the LTE approximation. To model the departures from LTE, we used the approximation of line absorption following the non-LTE computations by Baron *et al.* [25]. A discussion can be found in [22]. We do not claim to reproduce the light curves in this approximation absolutely accurately, especially two months after the explosion. However, our experience in modeling the light curves for other supernovae [22, 26, 27] shows our results to be reliable at the epoch of maximum and a month after it. A more important point is that here we are interested in relative changes of the light curve for the two classical burning regimes, and the reliability of reproducing such relative changes is beyond question.

BURNING REGIMES FOR THERMONUCLEAR SUPERNOVAE

It has now been firmly established that the SN Ia light curve is shaped by radioactive decay of ^{56}Ni to yield ^{56}Co and then ^{56}Fe. A thermal explosion in a degenerate carbon–oxygen mixture readily produces the required amount of ^{56}Ni and releases the required energy. However, the burning regimes for supernovae have been the subject of much controversy so far.

Arnett [14] computed the first models of supersonic burning, i.e., detonation. Subsequently, Ivanova *et al.* [15] obtained a subsonic, spontaneously propagating flame (deflagration) with pulsations, which then turns into detonation. Nomoto *et al.* [16] modeled the deflagration propagating by convective heat transport. The two burning regimes have their advantages and disadvantages in explaining the supernova phenomenon (see, e.g., the review article by Woosley and Weaver [28]).

In the case of instantaneous detonation starting near the stellar center, virtually all of the stellar matter would burn out up to the iron-peak elements [14]. This is evidently inconsistent with observations, which imply that the intermediate-mass elements in the ejection are fairly abundant. The burning must therefore be subsonic at some phase. In this case, another problem arises: It turns out that the burning must be considerably faster than that predicted by an analysis of the propagation of a laminar flame [29].

From a microscopic point of view, a one-dimensional nuclear flame is a wave described in the same way as was done by Zeldovich and Frank-Kamenetsky [30], although nuclear kinetics and a very high conductivity of the presupernova's dense matter slightly complicates this description. The velocity of the flame propagating in the presupernova by heat conduction is too low to correctly explain the supernova expansion: The Mach number for the flame proves to be $\leqslant 0.01$ [29].

The rate of nuclear burning can be naturally accelerated through the development of instabilities inherent in the flame front. As was explained by Landau in his classical paper [31], the front surface becomes corrugated and wrinkled because of hydrodynamic instability; i.e., the burning takes place on a larger area than a planar flame, and the front is therefore accelerated. In the limiting case, instabilities can cause a change of the burning regime from slow deflagration to detonation. The role of Landau instability for supernovae was pointed out in [32, 33]. As the instability grows, the front becomes corrugated and fractal. Blinnikov and Sasorov [34] performed a detailed analysis of the nonlinear phase of Landau instability and calculated the fractal dimension of the flame front.

Since the flame propagates in a gravitational field and since the burned matter is less dense than the combustible, Rayleigh–Taylor (RT) instability is commonly assumed to perturb the front shape (see [35–39]). RT instability generates a turbulent cascade that accelerates the flame and causes additional difficulties in modeling supernova explosions [40–42]. Turbulent mixing of hot burning products and cold fuel can switch on detonation following the period of slow expansion of a partially burned, degenerate star [42]. In this case, the transition to detonation can occur via the intermediate stage of spontaneous burning propagation [43]. However, the most recent computations by Reinecke *et al.* [44] show that the RT instability alone is not enough for the explosion: The expansion velocity is found to be too low. Additional turbulence sources are apparently required.

Of course, the burning cannot be completely simulated numerically, because this would require allowing for an enormous range of scales, from a flame thickness of $\sim 10^{-5}$ cm to a white-dwarf size of $\sim 10^{9}$ cm. Moreover, the behavior of turbulent gas inevitably becomes chaotic, and even small differences in the initial conditions may lead to a very large difference between the results. This is well known from ground-based experiments: A detonation explosion can occur at some time after tens or even hundreds of cases of slow burning, although the conditions in which the experiment was carried out remain virtually unchanged [45].

THEORETICAL SUPERNOVA MODELS AND LIGHT CURVES

We computed the theoretical light curves of supernovae by using initial models corresponding to the two different burning regimes: The classical deflagration model W7 [19] and the delayed detonation model DD4 [20]. Table 1 compares the basic parameters of these models, and Table 2 compares their chemical compositions after the explosion. Figures 1 and 2 show the distributions of density, velocity, and main chemical elements in exploded-star mass for these two models. As is evident from these figures and tables, the selected models have approximately equal hydrodynamic parameters, and the differences in chemical compositions are attributable to the difference between the burning regimes of the white dwarf (although the amounts of ^{56}Ni are nearly equal, we have the resulting light curves with almost coincident maxima). Both models are one-dimensional and highly simplified, whereas any individual SNe Ia must be a fairly complex three-dimensional fractal object. Our computed light curves, nevertheless, reproduce well the behavior of fluxes in different filters.

Figure 3 shows the results of our computations for models W7 and DD4 and observational data for two real supernovae, SN 1992A [46] and SN 1998bu [47]. The graphs clearly show that, while the absolute luminosities at maximum light are equal, the post-maximum decline rates in *B* for these two models differ markedly. Such differences are considerably less pronounced in *V*; model computations yield a closer similarity in the behavior of the light curves.

These differences are difficult to explain by a single factor: There are many physical parameters affecting the radiation. These parameters are almost equal in our models at each instant of time. However, it is probably a set of such insignificant differences that ultimately produces a marked difference between the light curves. For example, Fig. 2 shows small differences between the distributions of ^{56}Ni in the outer layers and of lighter elements closer to the center. As a result, the gamma-ray deposition and soft-photon diffusion occur in slightly different ways and determine the difference in the temperature distributions. Figure 4 shows these distributions on day 35 after the explosion, and the filled circles indicate the point at which the optical depth, measured from the outer boundary, reaches 2/3. The temperature at this point for model W7 is about 10% higher than that for DD4, while the radius is slightly larger, which quantitatively explains the *B* flux differences for this time (see Fig. 3).

Let us now look at how the shape of our light curves agrees with actual observations. Several quantitative characteristics can be used to describe the light-curve shape. One of the most widely used characteristics is the dependence $M_{\max}(\Delta m_{15}^B)$, where Δm_{15}^B is the brightness decline in *B* within the first 15 days after the maximum, suggested by Phillips [4]. It is customary to represent this dependence as a linear function of the form $M_{\max} = a + b\Delta m_{15}^B$. However, the coefficients *a* and *b* differ markedly from one another when different authors use different samples of supernovae; besides, the scatter of values turns out to be very large within each sample. The value of *a* is affected by the Hubble constant H_0 assumed in the calculations. In our case, we are more interested in the slope *b*, but the differences for it are great. For example, Phillips [4] inferred $b^B = 2.698 \pm 0.359$ from nine nearby supernovae, whereas Hamuy *et al.* [5], who analyzed only six supernovae from the same sample, derived $b^B = 1.624 \pm 0.582$. At the same time, using 26 distant supernovae discovered when the Calán/Tololo search program was carried out, Hamuy *et al.* [48] give an even lower value, $b^B = 0.784 \pm 0.182$. Such a scatter cannot be explained by observational errors alone; they are considerably smaller. The supernovae do not actually lie on a single straight line but occupy the entire region in the $M_{\max}(\Delta m_{15}^B)$ diagram, and this most likely reflects the actual differences in explosion physics. Our theoretical light curves (at least those computed for DD4) belong to this region. Using the relations derived by Phillips [4] and Hamuy *et al.* [48], we can estimate the magnitudes at maximum corresponding to the decline rates obtained in our models if we fix the Hubble constant. Comparing the resulting values with our models, we obtain for $H_0 = 85$ km s^{-1} Mpc^{-1}:

$$M_{\max}^B = \begin{cases} -18.8(\text{Phillips}) \\ -18.7(\text{Hamuy}) \\ -18.9(\text{model DD4}) \end{cases} \text{for } \Delta m_{15}^B = 1.07;$$

$$M_{\max}^B = \begin{cases} -19.9(\text{Phillips}) \\ -19.0(\text{Hamuy}) \\ -18.7(\text{model W7}) \end{cases} \text{for } \Delta m_{15}^B = 0.66.$$

Thus, model DD4 describes satisfactorily the observations if a short distance scale is adopted, whereas model W7 appears insufficiently bright. For a long distance scale ($H_0 = 65$ km s^{-1} Mpc^{-1}), we have

$$M_{\max}^B = \begin{cases} -19.4(\text{Phillips}) \\ -19.3(\text{Hamuy}) \\ -18.9(\text{model DD4}) \end{cases} \text{for } \Delta m_{15}^B = 1.07;$$

$$M_{\max}^B = \begin{cases} -20.5(\text{Phillips}) \\ -19.6(\text{Hamuy}) \\ -18.7(\text{model W7}) \end{cases} \text{for } \Delta m_{15}^B = 0.66.$$

Both models are now too faint. This may imply that, for the long distance scale, standard models similar to DD4 must contain 30–40% more ^{56}Ni to reach the observed supernova luminosity [48–50]. Thus, moving DD4 into the region of observed luminosities and assuming that the relative difference between the detonation and deflagration models is constant for the same increase in the amount of ^{56}Ni in them, we find that W7 remains about $0^m.5$ fainter than a supernova with the same slope of the light curve, as inferred by Hamuy *et al.* [48]. This difference may prove to be significant for cosmological applications of SNe Ia.

Figure 3 shows that the qualitative behavior of both computed light curves is correct. In particular, the brightness rise times agree with observations: Our computations with the two models yield 16–17 days, whereas the flux from observed SNe Ia increases to maximum in approximately 15–20 days [52–54]. Note that, in previous calculations of multicolor light curves (see, e.g., [17]), the flux increases only for about 10–15 days in most of the models, including W7. Note also that our light curves behave correctly in different spectral bands: The decline rate decreases with increasing wavelength for both models. However, it is also obvious that the brightness decline in the deflagration model is too slow and is inconsistent with observations of real supernovae, whereas the detonation model describes the observations excellently.

Model W7 has been widely used to compute the light curves of Type Ia supernovae and to analyze the subsequent evolution of supernova remnants. It was considered to be one of best models to reproduce the observed fluxes (see, e.g., [55, 56]). The difference between our results for W7 model, especially in the *B* band, and those obtained by other authors is due mainly to the different treatment of expansion opacity in

the energy equation. Blinnikov [57, 58] has described the correct approximation. He showed that there is no expansion effect [59] in the energy equation for photons when allowing for line opacities, that this effect should be included only in the equation of radiation flux. Line opacity far exceeds the contributions of other opacity sources and therefore including the expansion effect in the energy equation, as it was done by Höflich [55] and Eastman [56], results in overestimated energy exchange between matter and radiation. The photons have then their energies artificially redistributed into longer wavelengths, allowing them to leave the system more easily. As a result, we obtain a light curve with steeper declining and rising portions.

As an experiment, we computed a theoretical light curve of W7 model assuming that all opacity sources, spectral lines with expansion effect included, are purely absorptive. We thus "corrupted" the energy equation by artificially enhancing the energy exchange between matter and radiation. Although the altered model yielded "good" decline rate in the *B* band, the side effect was to decrease and thereby underestimate the inferred rise time. Corrupting our initial model made the results very much like those of Höflich. Figure 5 shows how the inclusion of scattering affects theoretical light curves computed in terms of this model. Note that, whereas at short wavelengths the decline rate of the new light curve can be considered satisfactory, this is by no means the case for the *I*-band light curve: It loses altogether its secondary maximum, which is a feature typical of almost all observed SNe Ia. Although the physical processes responsible for this secondary minimum still await a detailed analysis, the lack of minimum clearly indicates the failure of the model to properly allow for the physical processes that play an important role in the supernova radiation.

The corrupted energy equation thus allowed us to reproduce the results of other authors. Our computations with the correct energy equation demonstrate that deflagration model W7 yields a light curve that is too slow for a typical SNe Ia. We can suggest two interpretations for this result. One is that nature never allows pure deflagration to realize, thereby explaining the failure of the corresponding models to yield correct results. An alternative and more likely interpretation is that model W7 is based on oversimplified assumptions, whereas the more accurate deflagration model should allow for the factors ignored in W7 (see [42, 44]).

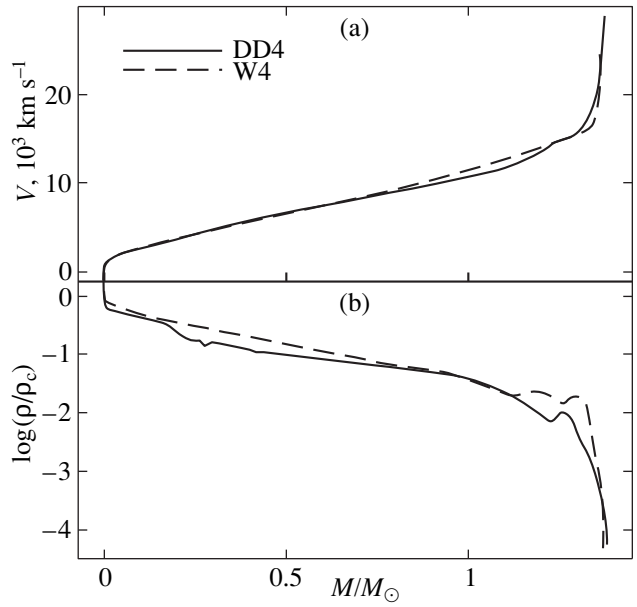

Fig. 1. The mass distributions of velocity (a) and density (b) for the initial models DD4 and W7. The density is in relative units. We started our computations with a central density of 9.76×10^{-9} g cm^{-3} at time $t = 8.16 \times 10^4$ s for DD4 and 7.42×10^{-3} g cm^{-3} at $t = 8 \times 10^2$ s for W7.

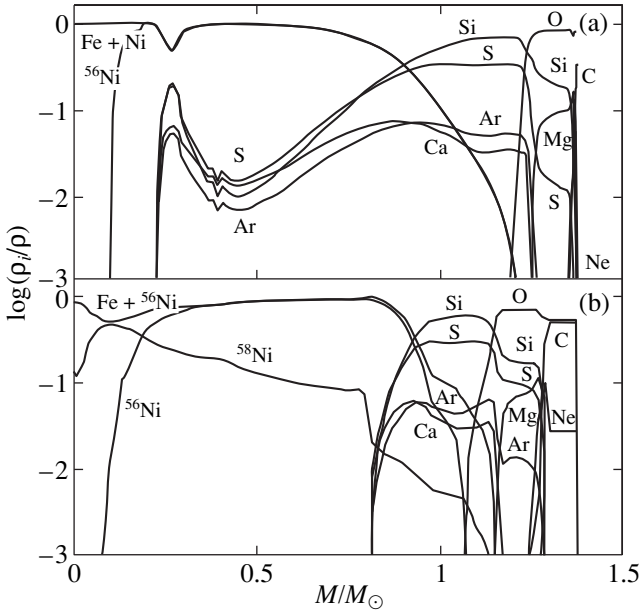

Fig. 2. The distribution of chemical elements in exploding-star mass for models DD4 (a) and W7 (b).

COSMOLOGICAL APPLICATIONS OF SNe IA

The magnitude at maximum light versus decline rate relation stimulated wide use of SNe Ia in cosmology as independent distance indicators and, consequently, as tools for probing the geometry of the Universe and testing various cosmological models. The point is that given the absolute luminosity of an object, simple formula $d_{\rm ph} = (L/4\pi F)^{1/2}$ allows the photometric distance to be determined from observations. At the same time, a theoretical distance can be computed for fixed z as a function of cosmological parameters H_0, Ω_m, and Ω_Λ [60]:

$$d_{\rm th} = \frac{c}{H_0}(1+z)\frac{1}{\sqrt{\Omega_k}}$$

$$\times \sinh\left\{\sqrt{\Omega_k}\int_0^z [\Omega_m(1+z)^3 + \Omega_\Lambda + \Omega_k(1+z)^2]^{-1/2} dz\right\},$$

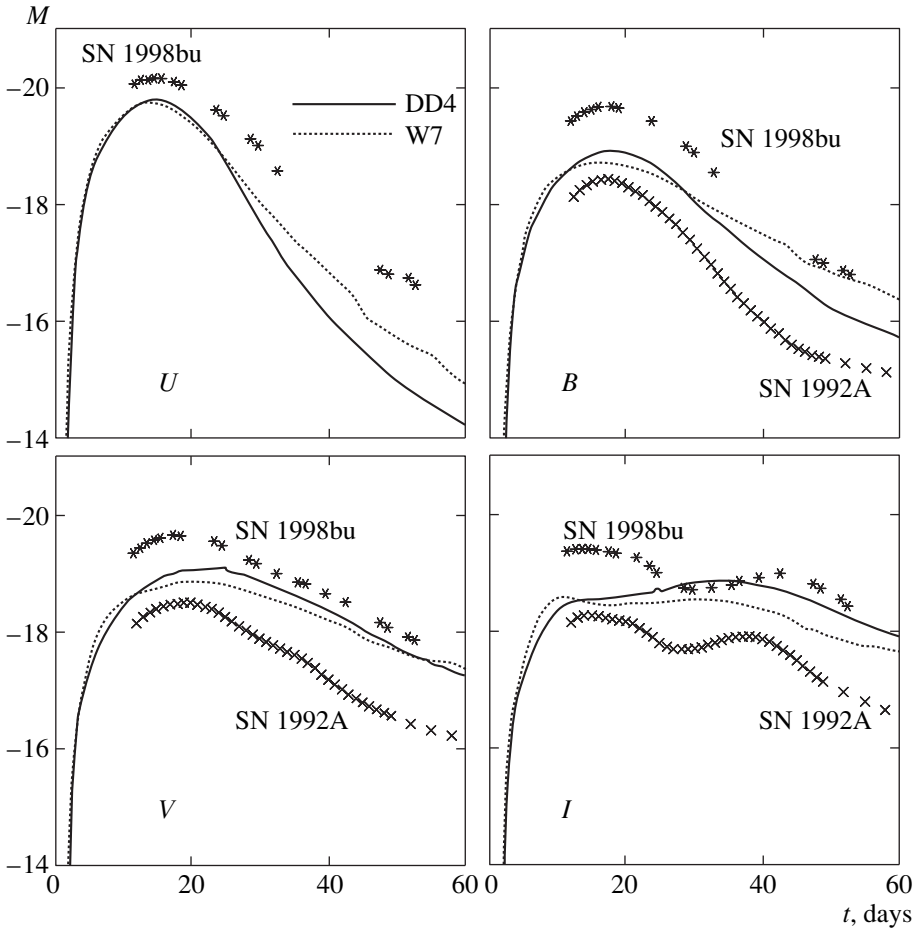

Fig. 3. *U*, *B*, *V*, and *I* light curves computed for models DD4 (solid line) and W7 (dotted line). Also shown are the typical observed light curves of two supernovae: SN 1992A (×) and SN 1998bu (∗). The curves are shifted along the time axis to make the maximum in *B* to coincide with the maximum of the DD4 curve.

where $\Omega_k = 1 - \Omega_m - \Omega_\Lambda$. If $\Omega_k < 0$, the ordinary sine function should be substituted for hyperbolic sine and $\sqrt{\Omega_k}$ should be substituted for $\sqrt{|\Omega_k|}$. The limiting case $\Omega_k \longrightarrow 0$ can be easily derived: The sine vanishes altogether, leaving only the integral term.

At present, several groups of researchers observe supernovae at large *z* and use them to estimate cosmological parameters using, in particular, the magnitude at maximum light versus decline rate relation. Nearby supernovae with good observational data available are used to calibrate this relation (see, e.g., [4]), which is then applied not only to nearby but also to distant objects. However, as was noted above, even nearby supernovae, albeit so similar at first sight, do not form an ideally homogeneous sample. As for evolutionary effects in supernova light curves, their analysis just begins.

To understand how the magnitude at maximum light versus decline rate relation can change for supernovae in younger galaxies, we must analyze the dependence of the light-curve behavior on the chemical composition of the exploding star.

The effect of the pre-explosion initial conditions on the SNe Ia radiation was studied by Dominguez *et al.* [61] and discussed by Riess *et al.* [12], Schmidt *et al.*

Table 1. Model parameters

Model	Burning regime	$M_{\rm WD}(M_\odot)$	E_{51}	$M_{^{56}\rm Ni}(M_\odot)$	Opacity
W7	Deflagration	1.3775	1.20	0.60	Scattering + absorption
W7a	Deflagration	1.3775	1.20	0.60	Pure absorption
DD4	Delayed detonation	1.3861	1.23	0.626	Scattering + absorption

[9], and Drell *et al.* [63] (see also a discussion of various pre-supernova models by von Hippel *et al.* [65] and Livio [64]).

Schmidt *et al.* [9] compared the distances to eight SNe Ia in early-type galaxies with the distances to 19 SNe Ia in late-type galaxies and revealed no significant differences. Here we must point out two circumstances. First, it is difficult to select coeval pre-supernovae in late-type galaxies. Second, the number of known coeval pre-supernovae is too small. We therefore must construct the distributions of SNe Ia at different z, and it is these distributions that we should compare after collecting statistically significant samples.

Dominguez *et al.* [61] found the shape of the light curve to depend on metallicity and C/O ratio in the corresponding pre-supernova. Variations of chemical composition can translate into a bias of up to $\sim 0^m.2$ in the distance modulus as inferred from the *mean* luminosity versus decline rate relation.

Dominguez *et al.* [61] analyzed the effects of metallicity and C/O ratio using only a single set of delayed detonation (DD) models. These authors found that the result is sensitive mostly to variations of ^{56}Ni mass.

When analyzing evolutionary effects in the shape of light curves, the authors of the above papers almost without exception assumed that the progenitor's chemical composition and structure determine completely the light curve of the resulting supernova. However, taking into account only the evolutionary effects is a manifestation of the deterministic approach. Evolution can prove to be less important than such a fundamentally nondeterministic factor as the burning regime in the exploding star. This assumption differs fundamentally from the approach taken by other authors. It is our opinion that burning can lead to substantially different results even if it started from identical (or slightly different) initial conditions. In other words, progenitors of the same age and chemical composition can evolve into very different SNe Ia, as evidenced by observations (see, e.g., [5]). If the distribution of SNe Ia within such samples depends on z, the failure to allow for this effect results in Λ being incorrectly estimated. Figure 3 clearly demonstrates how the absolute magnitude of a SNe Ia and, consequently, its distance, can be incorrectly determined. This figure shows how supernovae with the same maximum luminosity can differ in their decline rates due exclusively to different burning regimes, which are in principle impossible to predict in each particular case (we have already noted this when discussing the theory of burning). We can only identify certain trends, which indeed can depend on the chemical composition and age of the progenitor.

Let us assume that models W7 and DD4 represent two extreme cases of actual explosions of Chandrasekhar-mass white dwarfs. This gives us two alternatives. Either real supernovae represent a continuous sequence between the above two extremes or each supernova can be put into one of the extreme types.

Table 2. Chemical composition of the models (all masses are in $M_\odot$)

Element	W7 (W7a)	DD4
^{56}Ni	5.99×10^{-1}	6.26×10^{-1}
He	2.88×10^{-3}	0
C	4.56×10^{-2}	3.28×10^{-3}
O	1.41×10^{-1}	1.01×10^{-1}
Ne	4.42×10^{-3}	1.20×10^{-3}
Mg	8.64×10^{-3}	8.97×10^{-3}
Si	1.52×10^{-1}	2.58×10^{-1}
S	8.62×10^{-2}	1.56×10^{-1}
Ar	1.60×10^{-2}	3.47×10^{-2}
Ca	1.24×10^{-2}	3.75×10^{-2}
Fe	1.45×10^{-1}	1.59×10^{-1}
^{58}Ni	1.63×10^{-1}	0

Which of these two alternatives is realized in nature is of no importance to us. The only thing that matters is the nondeterministic nature of burning regime. This means that initial conditions allow only the proportions of W7 and DD4 type supernovae and the probabilities of observing certain shapes of light curves to be determined, whereas the exact shape of the light curve cannot in principle be predicted. If, for instance, the fraction of W7-like supernovae was higher at large z than at the present epoch, then treating all Type Ia supernovae as a homogeneous class of objects independently of z can easily result in incorrect absolute luminosities and,

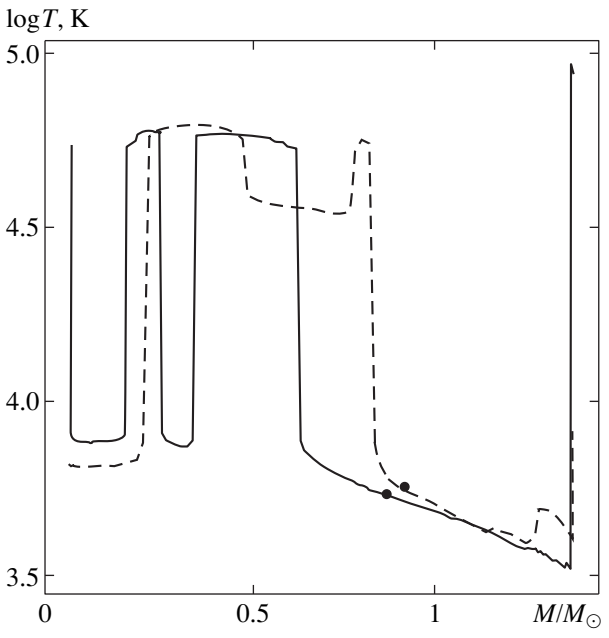

Fig. 4. The temperature distribution on day 35 after the explosion for models DD4 (solid line) and W7 (dotted line). The circles indicate the point at which the optical depth, measured from the outer boundary, reaches 2/3.

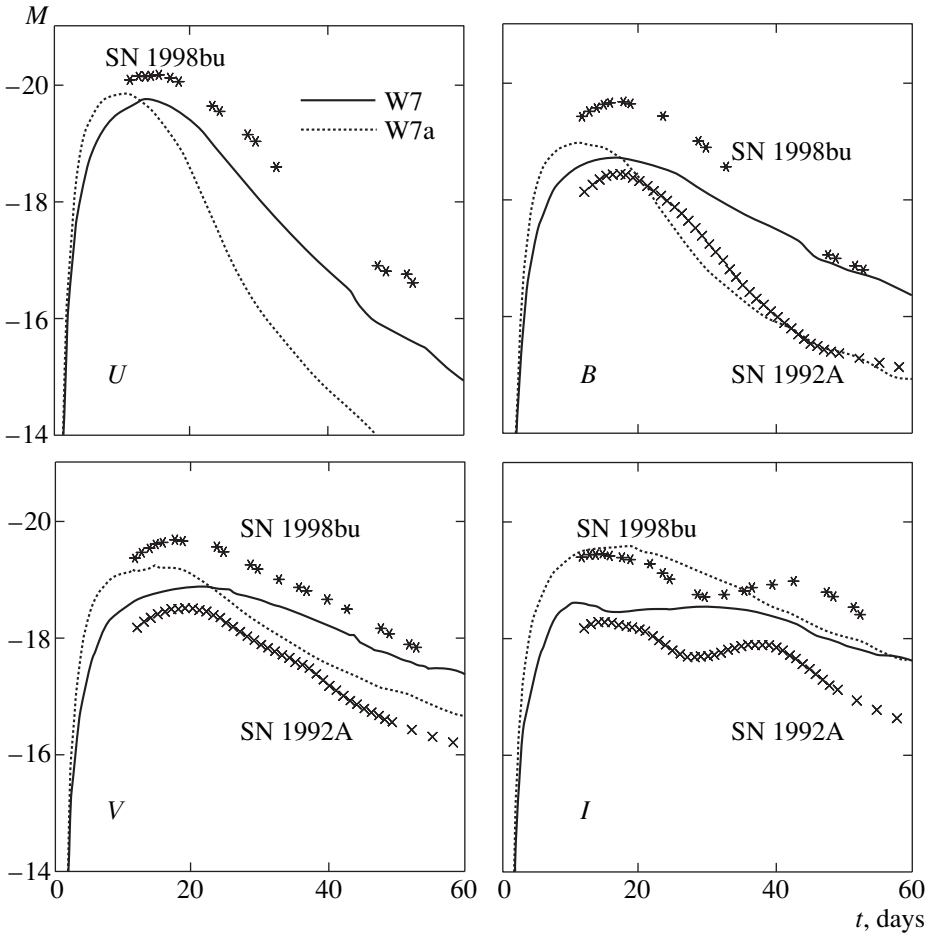

Fig. 5. Comparison of the light curves computed for model W7 (1) by assuming pure absorption for all opacity sources in the energy equation (model W7a, dotted line) and (2) with allowance for scattering and the proper inclusion of line opacity, i.e., without expansion effect, in the energy equation (model W7, solid line).

consequently, incorrect cosmological constant Λ being inferred.

According to one of the recent determinations of cosmological parameters using supernova observations [12], distant supernovae are 10–15% farther than implied by a model with $\Omega_m = 0.2$ and $\Omega_\Lambda = 0$. The above authors argue that the only way to prevent such a distance discrepancy is to assume that $\Omega_\Lambda > 0$. Actually, Λ can be, for instance, equal to zero if the earlier Universe contained a higher proportion of supernovae with slowly propagating burning fronts. In this case, the luminosities of distant supernovae should be, on the average, lower than implied by the maximum luminosity versus decline rate relation calibrated by using supernovae at small z, and the effect of positive Λ can be simulated by a change in explosion physics. It is our opinion that it is still too early to make any stringent statements until we have secured a large enough sample of distant supernovae: A decreased probability of W7 explosion scenario compared to earlier epochs could reconcile the observed and theoretical distances without assuming nonzero Λ.

CONCLUSION

The theoretical light curves of supernovae computed under various assumptions about the thermonuclear burning regimes for a carbon–oxygen white dwarf have led us to conclude that the post-maximum decline rate is very sensitive to the burning regime. Even small differences in the ^{56}Ni distribution, which result in a slightly different heating of matter inside the expanding star, are enough to ensure that the slopes of the light curve are different at coincident maxima.

The burning theory (at least in its present state) does not allow the exact burning regime to be predicted from specified initial conditions, and different burning regimes result in different temperature distributions. The knowledge of initial explosion conditions alone therefore does not determine the exact relation between the absolute magnitude at maximum light and the decline rate but only allows the probability distribution for the light-curve slopes to be determined for each magnitude at maximum light. This probability distribution can depend on initial conditions.

The future burning theory is likely to allow only the proportion between "fast" and "slow" supernovae to be determined, and this proportion might depend strongly on the initial conditions. Astronomers should not sit down and wait until the theory allows such exact predictions but test the distribution function by analyzing decline rates at different z.

What should be done in this situation? First, we must collect statistically sufficient samples of distant supernovae to allow the objects with equal maximum luminosities located at the same distance to be compared. In other words, we should construct for each z the decline-rate distributions for supernovae with different magnitudes at maximum light. The resulting distributions can either agree with or differ significantly from the corresponding distributions for the nearest supernovae. The latter case would mean that the statistical relations derived from nearby objects are absolutely inapplicable to distant supernovae. However, even if the brightest supernovae at, for instance, $z = 1$ are found to have the same decline-rate distribution as the brightest supernovae at $z < 0.1$, this fact would by no means imply that absolute maximum luminosities are the same for the two samples.

Second, the I-band light curves exhibit a larger scatter of individual supernovae, because this band is more sensitive to explosion physics. We can try to find out how the I-band light curve depends on burning regime by computing different theoretical models and comparing them with observed light curves. The flux emitted in the I band at large z will be observed on Earth in the far infrared and, therefore, will be difficult to measure. However, these measurements should be possible with new space telescopes such as the next-generation space telescope [62, 66]. I-band light curves can be useful in determining the explosion model for each particular supernova; however, this problem requires a detailed analysis of nonequilibrium effects in light-curve computations and further development of thermonuclear burning models.

ACKNOWLEDGMENTS

We are grateful to P. Ruiz-Lapuente, S. Woosley, K. Nomoto, and K. Iwamoto for providing the models that we used in our computations and to P. Lundqvist for permitting us to use the computing facilities at the Stockholm observatory and for his hospitality during our stay in Sweden. We are also grateful to D. Tsvetkov for helpful discussions. This study was supported by the INTAS–Russian Foundation for Basic Research (project no. 95-0832 "Thermonuclear Supernovae"), ISTC (grant no. 370-97), and Universidad de Barcelona.

REFERENCES

1. G. Sandage and G. A. Tammann., *Critical Dialogues in Cosmology,* Ed. by N.Turok (Singapore, World Scientific, 1997), p. 130.
2. Yu. P. Pskovskii, Astron. Zh. **54**, 1188 (1977).
3. O. S. Bartunov and D. Yu. Tsvetkov, Astrophys. Space Sci. **122**, 343 (1986).
4. M. M. Phillips, Astrophys. J. Lett. **413**, L105 (1993).
5. M. Hamuy, M. M. Phillips, J. Maza, *et al.*, Astron. J. **109**, 1 (1995).
6. H. U. Norgaard-Nielsen, L. Hansen, H. E. Jorgensen, *et al.*, Nature **339**, 523 (1989).
7. A. G. Kim, S. Gabi, G. Goldhaber, *et al.*, Astrophys. J. Lett. **476**, L63 (1997).
8. S. Perlmutter, S. Gabi, G. Goldhaber, *et al.*, Astrophys. J. **483**, 565 (1997).
9. B. P. Schmidt, N. B. Suntzeff, M. M. Phillips, *et al.*, Astrophys. J. **507**, 46 (1998).
10. P. M. Garnavich, R. P. Kirshner, P. Challis, *et al.*, Astrophys. J. Lett. **493**, L53 (1998).
11. P. M. Garnavich, S. Jha, P. Challis, *et al.*, Astrophys. J. **509**, 74 (1998).
12. A. G. Riess, A. V. Fillipenko, P. Challis, *et al.*, Astron. J. **116**, 1009 (1998).
13. S. Perlmutter, G. Aldering, G. Goldhaber, *et al.*, Astrophys. J. **517**, 565 (1999).
14. W. D. Arnett, Astrophys. Space Sci. **5**, 180 (1969).
15. L. N. Ivanova, V. S. Imshennik, and V. M. Chechetkin, Astrophys. Space Sci. **31**, 497 (1974).
16. K. Nomoto, D. Sugimoto, and S. Neo, Astrophys. Space Sci. **39**, L37 (1976).
17. P. Höflich, A. Khokhlov, J. C. Wheeler, *et al.*, *Thermonuclear Supernovae,* Ed. by P. Ruíz-Lapuente *et al.* (Dordrecht, Kluwer Acad., 1997), p. 659.
18. S. E. Woosley, *Thermonuclear Supernovae*, Ed. by P. Ruíz-Lapuente *et al.* (Dordrecht, Kluwer Acad., 1997), p. 313.
19. K. Nomoto, F.- K. Thielemann, and K. Yokoi, Astrophys. J. **286**, 644 (1984).
20. S. E. Woosley and T. A. Weaver, *Supernovae,* Ed. by J. Audouze *et al.* (Amsterdam, Elsevier Science, 1994), p. 63.
21. S. I. Blinnikov and O. S. Bartunov, Astron. Astrophys. **273**, 106 (1993).
22. S. I. Blinnikov, R. Eastman, O. S. Bartunov, *et al.*, Astrophys. J. **496**, 454 (1998)
23. D. A. Swartz, P. G. Sutherland, and R. P. Harkness, Astrophys. J. **446**, 766 (1995).
24. R. G. Eastman and P. A. Pinto, Astrophys. J. **412**, 731 (1993).
25. E. Baron, P. H. Hauschildt, P. Nugent, *et al.*, Mon. Not. R. Astron. Soc. **283**, 297 (1996).
26. S. I. Blinnikov, P. Lundqvist, O. S. Bartunov, *et al.*, Astrophys. J., 1999 (in press).
27. S. I. Blinnikov, Pis'ma Astron. Zh. **25**, 424 (1999) [Astron. Lett. **25**, 359 (1999)].
28. S. E. Woosley and T. A. Weaver, Ann. Rev. Astron. Astrophys. **24**, 205 (1986).

29. F. X. Timmes and S. E. Woosley, Astrophys. J. **396**, 649 (1992).
30. Ya. B. Zeldovich Ya.B. and D.A. Frank-Kamenetsky, Acta Physicochim. USSR **9**, 341 (1938).
31. L. D. Landau, Zh. Teor. Éksp. Fiz. **14**, 240 (1944); Acta Physicochim. USSR **19**, 77 (1944).
32. S. I. Blinnikov, P. V. Sasorov, and S. E. Woosley, Space Sci. Rev. **74**, 299 (1995).
33. J. C. Niemeyer and W. Hillebrandt, Astrophys. J. **452**, 779 (1995).
34. S. I. Blinnikov and P. V. Sasorov, Phys. Rev. E **53**, 4827 (1996).
35. E. Müller and W. D. Arnett, Astrophys. J. **307**, 619 (1986).
36. S. E. Woosley, *Supernovae*, Ed. by A.G. Petschek, Astron. Astrophys. Library (1990), p. 182.
37. S. E. Woosley, *Gamma-ray Line Astrophysics*, Ed. by P. Durouchoux and N. Prantzos (New York, AIP, 1990), p. 270.
38. E. Livne and W. D. Arnett, Astrophys. J. Lett. **415**, L107 (1993).
39. A. M. Khokhlov, Astrophys. J. Lett. **419**, L77 (1993).
40. J. C. Niemeyer and W. Hillebrandt, Astrophys. J. **452**, 779 (1995).
41. J. C. Niemeyer, Ph.D. Thesis, Garching, MPA-911 (1995).
42. J. C. Niemeyer and S. E. Woosley, Astrophys. J. **475**, 740 (1997).
43. S. I. Blinnikov and A. M. Khokhlov, Pis'ma Astron. Zh. **12**, 318 (1986) [Sov. Astron. Lett. **12**, 131–134 (1986)].
44. M. Reinecke, W. Hillebrandt, and J. C. Niemeyer, Astron. Astrophys., 1999 (in press); astro–ph/9812120.
45. Ch. Meider, *Numerical Simulation of Detonation* (Moscow, Mir, 1985).
46. N. B. Suntzeff, M. M. Phillips, R. Covarrubias, *et al.*, Astron. J. **117**, 1175 (1999).
47. M. Hamuy, M. M. Phillips, N. B. Suntzeff, *et al.*, Astron. J. **112**, 2438 (1996).
48. M. Hamuy, M. M. Phillips, N. B. Suntzeff, *et al.*, Astron. J. **112**, 2391 (1996).
49. W. D. Arnett, Astrophys. J. **253**, 785 (1982).
50. E. Cappellaro, P. A. Mazzali, S. Benetti, *et al.*, Astron. Astrophys. **328**, 203 (1997).
51. P. A. Mazzali, E. Cappellaro, I. J. Danziger, *et al.*, Astrophys. J. Lett. **499**, L49 (1998).
52. J. Maza, IAU Circ. No. 3583 (1981).
53. Yu. P. Pskovskii, Astron. Zh. **61**, 1125 (1984).
54. O. S. Bartunov and D. Yu. Tsvetkov, *Thermonuclear Supernovae*, Ed. by P. Ruíz-Lapuente *et al.* (Dordrecht, Kluwer Acad., 1997), p. 87.
55. P. Höflich, Astrophys. J. **443**, 89 (1995).
56. R. G. Eastman, *Thermonuclear Supernovae*, Ed. by P. Ruíz-Lapuente *et al.* (Dordrecht, Kluwer Acad., 1997), p. 571.
57. S. I. Blinnikov, Pis'ma Astron. Zh. **22**, 92 (1996) [Astron. Lett. **22**, 79 (1996)].
58. S. I. Blinnikov, *Thermonuclear Supernovae*, Ed. by P. Ruíz-Lapuente *et al.* (Dordrecht, Kluwer Acad., 1997), p. 589.
59. A. H. Karp, G. Lasher, K. L. Chan, *et al.*, Astrophys. J. **214**, 161 (1977).
60. S. M. Carroll, W. H. Press, and E. L. Turner, Ann. Rev. Astron. Astrophys. **30**, 499 (1992).
61. I. Domínguez, P. Höflich, O. Straniero, *et al.*, astro-ph/9905047.
62. M. J. Rees, *The Next Generation Space Telescope: Science Drivers and Technological Challenges*, 34th Liege International Astrophys. Colloq. (ESA, 1998), p. 237; astro-ph/9809029.
63. P. S. Drell, T. J. Loredo, and I. Wasserman, Astrophys. J., 1999 (in press); astro-ph/9905027.
64. M. Livio, astro-ph/9903264.
65. T. von Hippel T., G. D. Bothun, and R. A. Schommer, Astron. J. **114**, 1154 (1997).
66. T. Dahlén and C. Fransson, Astron. Astrophys., 1999 (in press); astro-ph/9905201.

Translated by A. Dambis

Astronomy Letters, Vol. 26, No. 2, 2000, pp. 77–87. Translated from Pis'ma v Astronomicheskiĭ Zhurnal, Vol. 26, No. 2, 2000, pp. 102–114.

The Supernova Remnant G78.2+2.1: New Optical and X-ray Observations

T. A. Lozinskaya[1], V. V. Pravdikova[1], and A. V. Finoguenov[2]

[1] *Sternberg Astronomical Institute, Universitetskiĭ pr. 13, Moscow, 119899 Russia*
[2] *Space Research Institute, Russian Academy of Sciences, ul. Profsoyuznaya 84/32, Moscow, 117810 Russia*

Received May 11, 1999; in final form, June 9, 1999

Abstract—New optical and X-ray observations of the supernova remnant (SNR) G78.2+2.1 are presented. CCD Hα observations with a Fabry–Perot interferometer attached to the 125-cm reflector at the Crimean Station of the Sternberg Astronomical Institute are used to obtain the radial-velocity field toward the SNR and in its vicinity. The brightness distribution and X-ray spectrum of the SNR are obtained from archival ROSAT and ASCA X-ray data. The X-ray image of G78.2+2.1 exhibits a shell structure ($\Delta R/R \simeq 0.3$) and is generally similar to its radio image; a comparison with the radio map at $\nu = 1.4$ GHz constructed from archival VLA data reveals the coincidence of features on scales of several arcminutes at the eastern boundary of G78.2+2.1. Weak X-ray emission (an outer shell or a halo of size $\simeq 2°$) has been identified for the first time far outside G78.2+2.1. The X-ray emission from G78.2+2.1 is shown to characterize a young adiabatic SNR [$M_{\mathrm{X-ray}} \simeq 100 M_\odot$, $V_s \simeq 10^3$ km s^{-1}, $t \simeq (5\text{–}6) \times 10^3$ years], which probably expands inside the cavity swept up by the progenitor's stellar wind. Searches for the corresponding radio structure are required to elucidate the nature of the outer X-ray shell or halo. © *2000 MAIK "Nauka/Interperiodica".*

1. INTRODUCTION

The supernova remnant (SNR) G78.2+2.1 (see [1–4] and references therein) lies in the sky area toward the Cyg X complex that is most difficult to study. Since this area has a complex structure, where more than forty H II regions and a large number of shell structures of various scales are concentrated, the SNR G78.2+2.1 was not identified immediately; there is still a confusion of names in present-day literature. The brightest radio source DR4 in the complex and the associated 3′ nebula near γ Cygni [5] were originally believed to be the SNR.

However, the spectroscopic and interferometric observations of the nebula near γ Cygni by Lozinskaya [6] and Johnson [7] showed this to be an H II region rather than a SNR; the ionizing star was also found at its center [8, 9]. To explain the nonthermal radio emission from an "ordinary" H II region, Lozinskaya [10] suggested that it was overrun by an expanding shell, the remnant of a supernova exploded nearby. Higgs *et al.* [1] and Baars *et al.* [11] actually found a ~1° radio shell of G78.2+2.1 with a synchrotron spectrum. The source DR4 constitutes the brightest southeastern part of G78.2+2.1, and its radio emission consists of two components, thermal and nonthermal.

Here, we present our Hα Fabry–Perot observations of the region and reduce the archival ROSAT and ASCA X-ray data for G78.2+2.1. We also use the archival VLA data for the eastern part of G78.2+2.1.

Section 2 describes the technique of interferometric observations and presents the results of our study of the radial-velocity field toward the SNR and in its vicinity. The X-ray observations of G78.2+2.1 are reduced in Sect. 3. The data and the conclusions concerning the SNR nature that follow from them are discussed in Sect. 4.

2. INTERFEROMETRIC Hα OBSERVATIONS

2.1. Observing and Reduction Techniques

We studied the radial-velocity field in Hα by using a Fabry–Perot interferometer with a CCD at the Cassegrain focus of the 125-cm reflector at the Crimean Station of the Sternberg Astronomical Institute. The pre-monochromatization was carried out by means of an interference filter with a FWHM of ≃20 Å. The field of view and the angular resolution were, respectively, 10′ and 3–4″; the actual spectral resolution corresponded to ≃15 km s^{-1}. The free dispersion region (the radial-velocity range free from the overlapping of adjacent interference orders) was ~800 km s^{-1}; the [N II] 6584 Å line was in the middle of this range and was clearly separated from Hα, whose largest zero-level width did not exceed 200 km s^{-1} everywhere in the region under study.

The line profile was fitted with one or more Gaussians by assuming that the FWHM of each component was larger than the FWHM of the instrumental profile and that the signal-to-noise ratio was ≥5. In 1997–1998, we obtained 23 interferograms in a large area including the SNR G78.2+21. We also used the observations of

the bright nebula near γ Cygni performed by Lozinskaya [6] with the same Fabry–Perot interferometer at the focus of the 125-cm reflector; the only difference was the use of an image intensifier instead of a CCD array as the light detector. In 1974, a total of eight Hα interferograms and five [N II] interferograms were taken; the total number of previous velocity measurements exceeds 100.

The localization of the interferometric rings of the Hα and [N II] lines in the G78.2+2.1 image is shown in Fig. 1. Also shown in this figure is the localization of rings for the nearby Cygnus X region, which mainly falls within the X-ray shell we identified (see Subsect. 3.2). For a comparison with velocities in the extended Cygnus X region, we used about 40 more Hα images outside the boundaries of Fig. 1.

2.2. Results of the Hα Observations

The H II velocity measurements based on the 1997–1998 observations are shown in Fig. 2 in the form of radial-velocity histograms for the Hα components. Figures 2a and 2b correspond, respectively, to the SNR G78.2+2.1 and to the nearby regions of the Cygnus X complex outside the bright SNR but inside the weak outer X-ray shell identified in Subsect. 3.2.

We see from Fig. 2a that the characteristic H II radial velocity toward G78.2+2.1 lies in the range $V(\mathrm{LSR}) = 0$–10 km s^{-1} at half maximum of the histogram. At the same time, a group of negative radial velocities, $V(\mathrm{LSR}) = -(45$–$20)$ km s^{-1}, is clearly identified. The mean velocities corresponding to the two peaks in the histogram are $V_1 = 2.6 \pm 4.3$ km s^{-1} (for 109 measurements) and $V_2 = -34.7 \pm 7.9$ (for 21 measurements).

A comparison of the velocity distributions for the bright SNR (Fig. 2a) and for the weak outer X-ray shell (Fig. 2b) reveals no statistically significant differences. Velocities from $V(\mathrm{LSR}) = -5$ to $V(\mathrm{LSR}) = +15$ km s^{-1} at half maximum of the histogram are observed in the outer region; the mean velocity is $V(\mathrm{LSR}) = 6.0 \pm 4.2$ km s^{-1}. A component at $V(\mathrm{LSR}) = -(50$–$20)$ km s^{-1} with a mean velocity of -34 km s^{-1} is also distinguished in the histogram of Fig. 2b.

The Hα and [N II] profiles for the bright nebula near γ Cygni turned out to be single. The mean velocity of the nebula is $V(\mathrm{LSR}) = 9 \pm 3$ km s^{-1}; the mean velocity of the nearby bright H II regions of the radio source DR4 (at distances no larger than 10′ from the nebular boundary) is $V(\mathrm{LSR}) = -2 \pm 2$ km s^{-1}. These measurements agree, within the error limits, with $V(\mathrm{LSR}) \simeq 5$ km s^{-1} obtained by Johnson [7] from a single interferogram of the γ Cygni nebula. The velocities near the radio source DR4 and the γ Cygni nebula are seen to match those of the main component in the diagram of Fig. 2a for the extended SNR G78.2+2.1.

When making a comparison with the velocity field in the Cygnus X complex outside G78.2+2.1 and the weak outer shell, we made sure that a single line was manly observed in the east and in the west in the velocity range from 2.5 to 17. 5 km s^{-1} with a mean velocity of 10 ± 4.2 km s^{-1}. The corresponding histogram for distances between 2° and 4° from the SNR center is shown in Fig. 2c. At the same time, local regions with high-velocity gas motions are encountered east and north of G78.2+2.1, i.e., closer to the Cygnus X center. They are probably associated with additional sources of mechanical energy or with large-scale motions of a different origin; their discussion is beyond the scope of our study. We therefore collected the velocities of these "peculiar" regions in the histogram of Fig. 2d solely to emphasize that high velocities in the range from –35 to +35 km s^{-1} are observed not only toward the SNR. Similar mean velocities were obtained for Cygnus X from radio recombination-line observations: The group of sources DR 18, 20, 21, 22, and 23 has the mean velocity $V_{166\alpha} = 6$ km s^{-1}; and the group of IC 1318b, c, DR 6, 9, 12, 13, and 15 has the mean velocity $V_{166\alpha} = -5$ km s^{-1} [12]. The mean velocity of the Cygnus X complex as inferred from the $H_{110\alpha}$ measurements by Piepenbrink and Wendker [13] is –2.9 km s^{-1} (see also [14]).

Thus, our Hα measurements have shown that there is agreement between the velocities toward the G78.2+2.1 shell, for its bright southeastern part near γ Cygni, and for the outer weak X-ray shell.

Our measured high H II velocities toward the SNR are confirmed by 21-cm observations: Landecker *et al.* [15] and Braun and Strom [16] detected high-velocity H I clouds of small angular sizes here. The high velocity of the shock triggered by the SNR expansion is also suggested by the X-ray observations presented in Sect. 3. Nevertheless, since high H II velocities are observed not only toward the SNR but also outside it in the central region of Cygnus X, we cannot unequivocally relate the detected high velocities to G78.2+2.1.

3. X-RAY EMISSION FROM THE SUPERNOVA REMNANT

X-ray emission from the bright southeastern part of G78.2+2.1 was observed from the Einstein Observatory [17]. The ROSAT images of G78.2+2.1 were published in [18, 19] but without quantitative estimates, only to localize the gamma-ray source 2EG J2020+4026 and the associated compact X-ray source.

3.1. The Archival ROSAT and ASCA Data and Their Reduction

We analyzed the archival data for G78.2+2.1 from two X-ray observatories: ROSAT [20] and ASCA [21]. The PSPC instrument of the ROSAT Observatory has an angular resolution of 0′.5 and a spectral energy resolution $E/\Delta E \simeq 0.4$ at 1 keV. The SIS0 and SIS1 instruments (CCD arrays) of the ASCA Observatory have a spectral resolution $E/\Delta E \sim 50$ at energies 6 keV. The

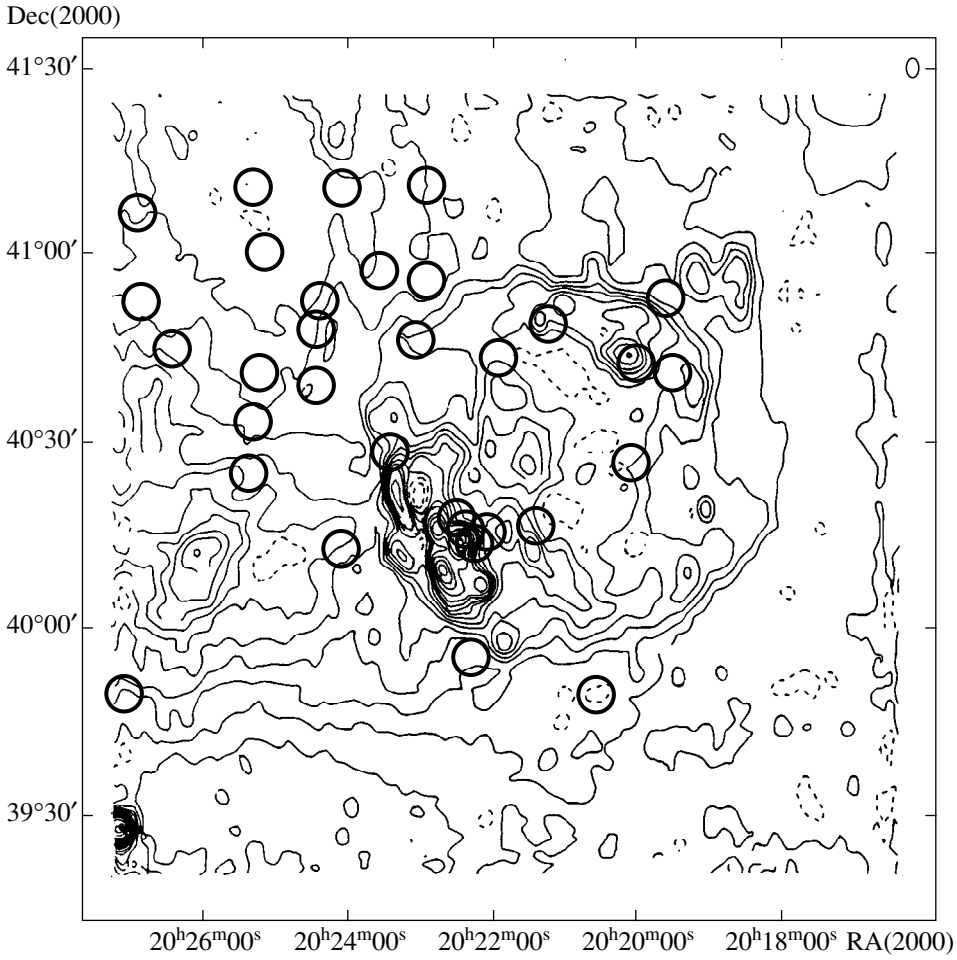

Fig. 1. Localization of interferometric rings of the Hα and [N II] 6584 Å lines superimposed on radio isophotes of G78.2+2.1 from [1].

point response function of the telescopes is characterized by a central peak with a FWHM of ~1′ and broad (~3′) wings. When all the four CCD arrays are used, the SIS field of view is 20′ × 20′. The SIS detectors are described in detail in [22].

We used the software package described in [23] to reduce the ROSAT data. Based on this packet, we chose exposure intervals with a minimum background, estimated the background level, and obtained exposure maps.

X-ray spectra were constructed from the ROSAT observations by using the XRAY package in the IRAF data-reduction system. Determination of the PSPC background in this package is based on [24]. We performed a spectral analysis in the recommended 0.2–2.0-keV energy band.

We used the 0.5–2.0-keV energy band, where the background effect is at a minimum, to analyze the images. The images were processed by wavelet transform analysis [25, 26].

The SNR G78.2+2.1 was observed in five PSPC/ROSAT pointings; the entire region corresponding to the bright radio source G78.2+2.1 was observed in the central part of the field of view, where the background effect is negligible. When weaker X-ray features far outside the radio SNR (the outer weak shell; see Subsect. 3.2) are analyzed, it should be borne in mind that these features can result in part from an enhancement of the PSPC background at the edge of the field of view. One of the pointings was centered on the SNR northern region, which simplified appreciably the background-subtraction procedure in this observation.

We analyzed the ASCA data by using the standard FTOOLS V4.1 software package for initial data reduction. This reduction involves choosing exposure intervals with a minimum background, estimating the background level, removing "hot pixels" of the SIS0 and SIS1 detectors, constructing the detector response matrix for the epoch of observation, and calibrating the instrumental energy scale.

The SIS/ASCA observations (three pointings) cover only the central part of G78.2+2.1 ($R \le 15'$) and the region north of the SNR center ($0' \le R \le 30'$).

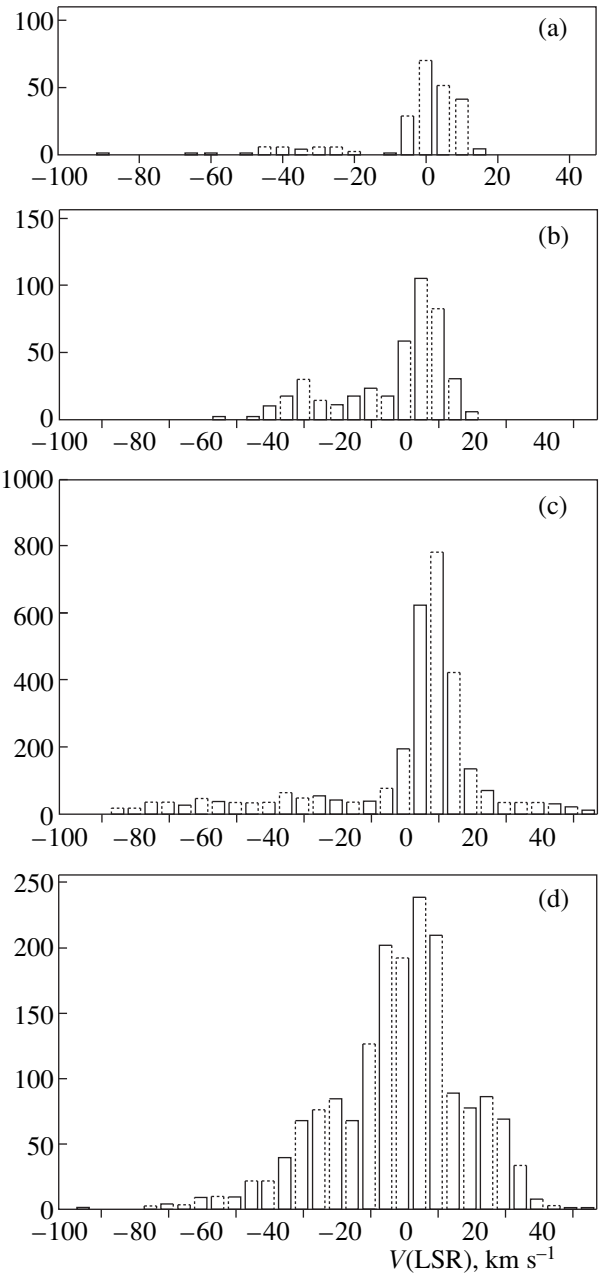

Fig. 2. Radial-velocity histograms for the Hα components: (a) in the SNR G78.2+2.1; (b) in the nearby region of the Cygnus complex X outside the bright SNR but inside the weak outer X-ray shell (see the text in Subsect. 3.2); (c) in the Cygnus X complex south and west of G78.2+2.1 at 2°–4° from the SNR center; (d) in the Cygnus X complex east and north of G78.2+2.1 (see text).

3.2. X-ray Image of the SNR

The X-ray (0.5–2.0 keV) brightness distribution of the SNR constructed by reducing the ROSAT data is shown in Fig. 3a. For comparison, Fig. 3b shows the distribution of synchrotron radio emission at a frequency of 1.4 GHz from [1] on the same scale. The X-ray image of the SNR G78.2+2.1 is characterized by a shell morphology; in general, there is agreement between the large-scale radio and X-ray structures of the SNR.

Figure 4 compares the fine X-ray emission features with the radio brightness distribution at 1.4 GHz as inferred from VLA aperture-synthesis observations. The radio isophotes were constructed from archival NRAO VLA Sky Survey (NVSS) data; the NVSS survey is described in detail in [27]. As follows from Fig. 4, there is a correlation between the features of the X-ray and radio images on scales of several arcminutes. This correlation is most noticeable at the eastern boundary, where the SNR most likely collides with a dense cloud of interstellar gas. In other regions, there is no one-to-one correspondence: Bright X-ray knots correspond to all compact bright radio features, but there are X-ray knots with no corresponding radio brightening.

The two elongated regions of reduced X-ray brightness, a wide band in the south (from RA = 20^h19^m, D = 39°40′ to RA = 20^h26^m, D = 39°40′) and a narrow band at the eastern boundary of G78.2+2.1 (RA = 20^h24^m, D = 40°0′–41°20′), are probably attributable to absorption; dust lanes are seen here on Palomar Atlas red maps.

The outer region of weak X-ray emission far outside the synchrotron source G78.2+2.1 and the bright X-ray SNR is clearly seen in Fig. 3a. This outer X-ray region is symmetric about G78.2+2.1; its geometrical center coincides with the SNR center, and the size is ~2°, which is twice the size of the bright shell.

The outer X-ray shell has been identified here for the first time. As was noted in Subsect. 3.1, weak features of the outer shell were observed at the edge of the field of view in four of the five telescope pointings and may partly result from an enhancement of the background toward the detector edge. One pointing was centered on the northern part of the SNR; the bright G78.2+2.1 shell, and the weak outer shell were observed at the center of the field of view. We therefore believe the reality of the northern part of the outer shell to be beyond question.

Figure 5 shows the SNR surface-brightness profiles. The SNR-averaged profile and the cuts in the northward and southward directions are presented. The profiles were constructed from three independent PSPC/ROSAT observations. The PSPC background effect does not change with radius in this figure, because we applied a correction for the instrument sensitivity. The difference in the background levels between the three observations can be easily determined from the flux in the central region $R \le 5'$, where the sky areas under study coincide. For comparison, the figure also shows the temperature profiles obtained in spectral analysis (see Subsect. 3.3).

Based on Figs. 3a and 5, we cannot unambiguously determine whether the detected outer weak emission is a shell or halo structure, because, as was pointed out

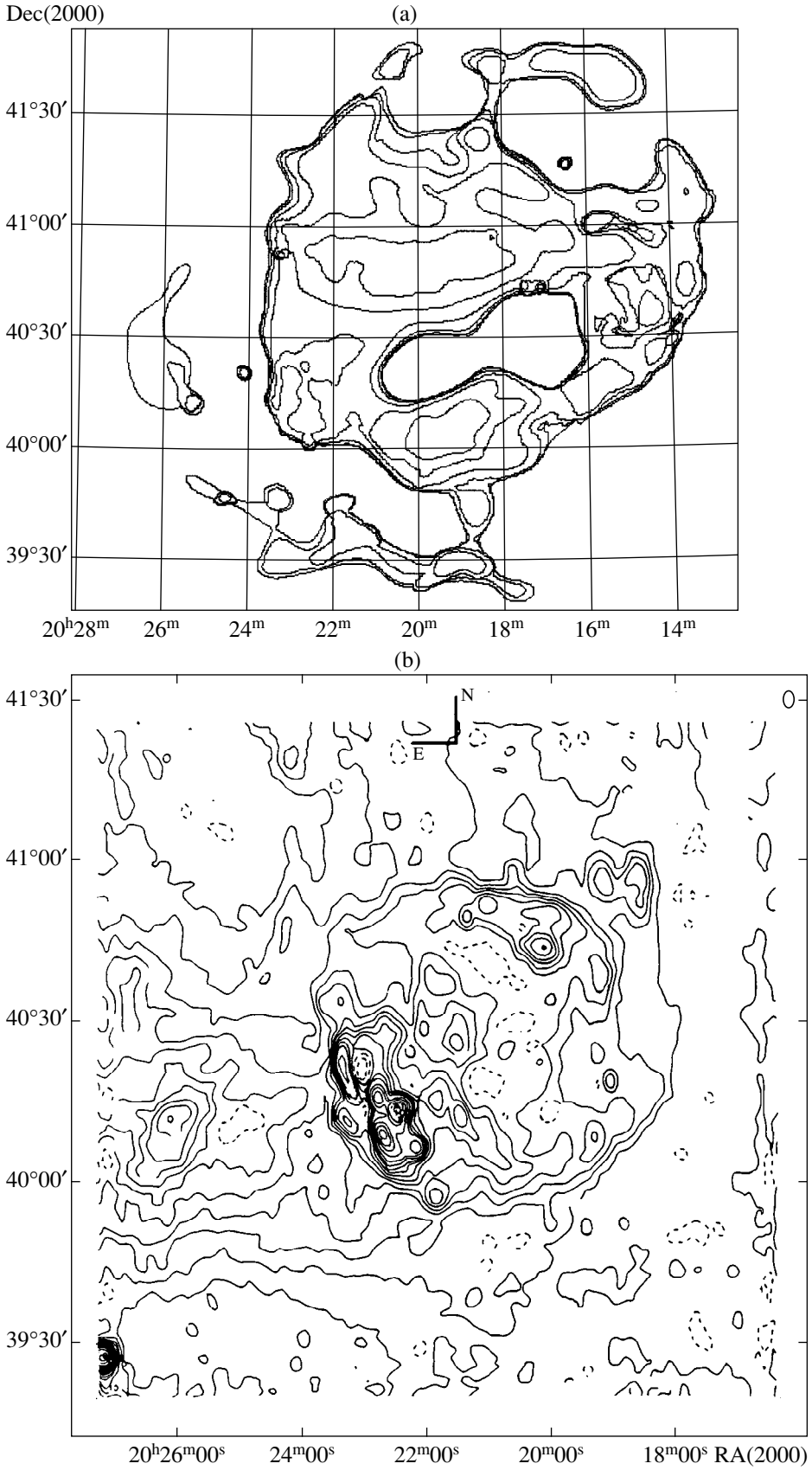

Fig. 3. (a) X-ray (0.5–2.0 keV) brightness distribution of the SNR as constructed from ROSAT data; (b) radio brightness distribution at 1.4 GHz from [1] on the same scale.

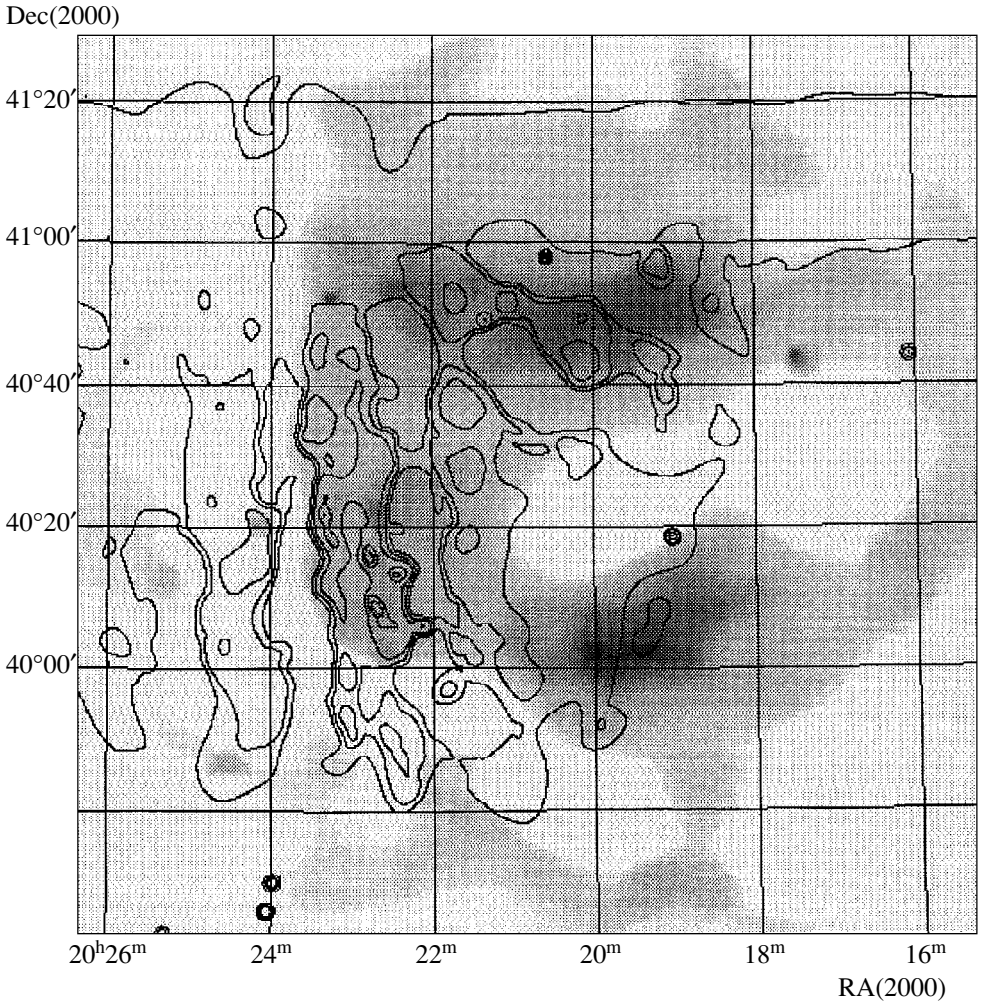

Fig. 4. X-ray (0.5–2.0 keV) brightness distribution as constructed from ROSAT data (black-and-white image) superimposed on the radio (1.4 GHz) isophotes constructed from archival NRAO VLA Sky Survey (NVSS) data.

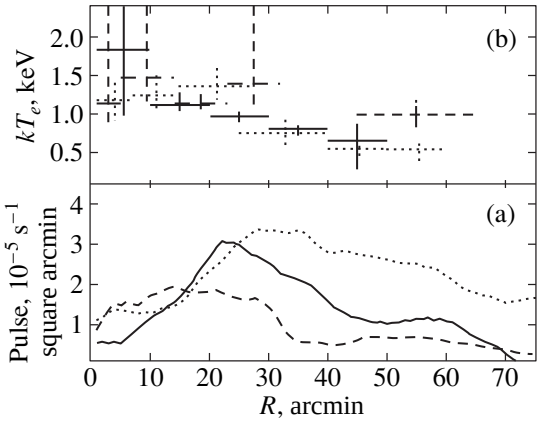

Fig. 5. (a) SNR surface-brightness profiles constructed from three independent PSPC/ROSAT observations: averaged over the remnant (solid line), in the northward (dotted line) and southward (dashed line) directions. (b) The temperature variation with distance from the SNR center; the lines designations are the same as those in (a). The data in the northward direction within 25′ were obtained from SIS/ASCA observations; the remaining values were obtained from PSPC/ROSAT observations.

above, the most pronounced dip in the eastern cut can be produced by the interstellar absorption, and the contribution of this cut to the average profile is significant.

3.3. X-ray Spectrum

Since an analysis of the ROSAT spectral data is complicated by low statistics and interstellar extinction, we first analyzed the ASCA data. We used the MEKAL model [28, 29] and the table of relative elemental abundances from [30] for the solar photosphere (Fe/H = 4.65×10^{-5} by the number of atoms).

Figure 6a shows the localization of the field of view for three ASCA pointings superimposed on the ROSAT image of the SNR. The average spectrum of this region is shown in Fig. 6b.

The spectral fit for this part of G78.2+2.1 in the ionization equilibrium plasma model corresponds to the temperature $kT_e = 1.4 \pm 0.1$ keV and the heavy-element abundance $Z = 0.27 \pm 0.1 Z_\odot$. Here, all confidence intervals correspond to a 68% confidence level. The derived

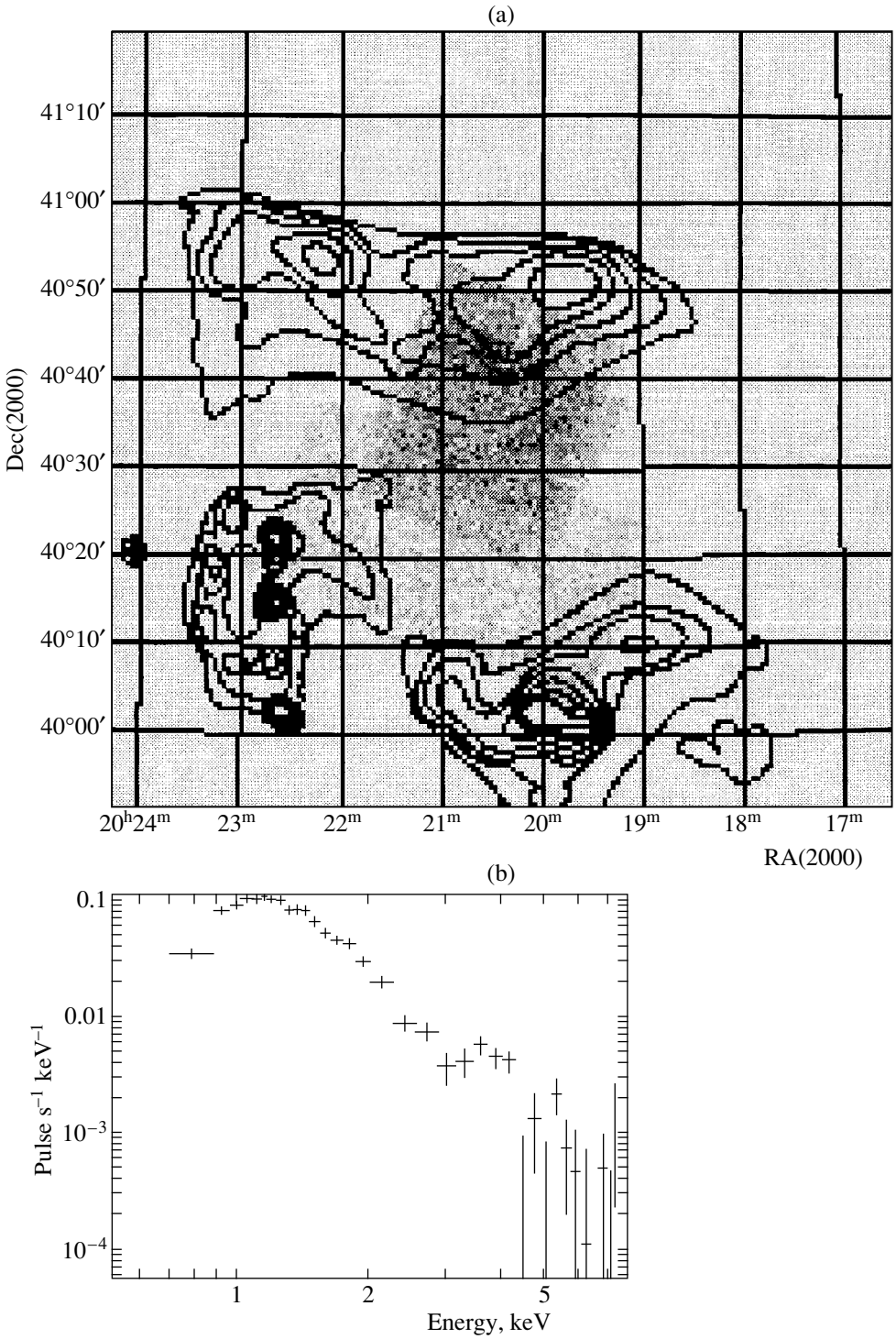

Fig. 6. (a) SIS/ASCA image of the central part of the SNR formed from the sum of four pointings superimposed on the surface brightness isolines as constructed from PSPC/ROSAT data. (b) The average SIS/ASCA spectrum of this region.

abundance agrees with the abundance for the Galactic thick disk [31]. Note that only the iron abundance affects the Z determination for solar elemental abundances.

The nonequilibrium ionization model [32], as applied to the ASCA data, yields a higher temperature (kT_e = 2.77 ± 0.4 keV), a comparable heavy-element abundance [$Z = (0.24 \pm 0.07)Z_\odot$], and the ionization parameter $\log(n_0 t_i)$ = 11.06 s cm^{-3}; the confidence interval is (11.00–11.16). The parameter $n_0 t_i$, where n_0 is the ambient density of the interstellar medium and

t_i is the time after the shock passage, characterizes the advanced stage of ionization equilibrium (ionization age). The spectrum in Fig. 6b is "nonequilibrium" in that, in the presence of the iron-line emission peak at energy 1 keV characteristic of a 1.4-keV temperature, the continuum emission proves to be harder and corresponds to a temperature of 2.8 keV. Note also that, when the temperature in the PSPC/ROSAT and SIS/ASCA experiments is determined, the iron peak at 1 keV is of crucial importance. Under the assumption of ionization equilibrium, the derived temperatures are therefore the "ionization" ones.

When analyzing the ROSAT data, we took the elemental abundance that was deduced for the northern part of the SNR from ASCA measurements. The X-ray spectrum of the shell's extended bright features that fits the ROSAT data best assuming equilibrium plasma of this chemical composition yields $kT_e = 1.37 \pm 0.12$ and 1.00 ± 0.05 keV for the eastern and southern regions, respectively.

The profile of temperature variation with distance from the SNR center is shown in Fig. 5. The figure reveals a temperature constancy within 20′ at a 1.3-keV level and a subsequent drop in temperature, both in the northward and southward directions and, on average, over the SNR. The temperature at 60′ from the center is 0.5 keV, on average, over the SNR and in the north and twice as high in the east.

As we see from the figure, the outer X-ray shell (or the halo) is distinguished not only by its morphology but also differs from G78.2+2.1 in spectrum, although there is no sharp temperature drop.

The absorption of X-ray emission from the three bright SNR regions mentioned above corresponds to the column density $N(\mathrm{H}) = (1\text{–}3) \times 10^{21}$ cm^{-2}. The column density derived from the X-ray data is in close agreement with that deduced from direct 21-cm measurements: Landecker *et al.* [15] obtained $N(\mathrm{H\,I}) \approx 1.6 \times 10^{21}$ cm^{-2}, on average, over the SNR and a slightly higher value for its bright southeastern part.

Note that the Einstein observations with a lower angular resolution and lower sensitivity revealed emission from the brightest part of the SNR and yielded a similar temperature ($4 \times 10^6 \le T_\mathrm{X} \le 5 \times 10^7$ K), density ($n_0 \simeq 0.1\text{–}0.4$ cm^{-3}), and column density [$N(\mathrm{H\,I}) = 3 \times 10^{21} - 3 \times 10^{22}$ cm^{-2}] (see [17]).

The mean density and mass of X-ray emitting plasma

Region	Radius	n_X, cm^{-3}	M, $M_\odot$
Entire SNR	0′–40′	0.05 ± 0.01	47 ± 3
SNR + halo	0–60	0.04 ± 0.01	95 ± 10
Center	0–15	0.08 ± 0.01	4.0 ± 0.8
North	15–40	0.05 ± 0.01	11 ± 0.8
North	15–60	0.04 ± 0.01	27 ± 1.4
East	15–30	0.08 ± 0.01	5.9 ± 0.4
South	15–30	0.084 ± 0.004	8.3 ± 0.4
West	30–60	0.024 ± 0.003	14 ± 2

4. DISCUSSION

The distance $d \simeq 1.8$ kpc to G78.2+2.1 and its linear size of ~33 pc were determined from the dependence of surface radio brightness on SNR diameter [the so-called Σ(D) dependence] by Higgs *et al.* [1] and Landecker *et al.* [15]. Using a more complete Σ(D) dependence, which included a number of extragalactic calibration sources [3, 33], we obtained a similar SNR diameter of 29.4 pc and distance of 1.7 kpc from the flux density S (1 GHz) = 340 Jy [34]. At such a distance, the expected mean shell velocity in the Galactic rotation model by Dambis *et al.* [35] is ≃6–7 km s^{-1}; i.e., it agrees with the observed H II velocities in G78.2+2.1.

Since the error in the distance estimated from the Σ(D) dependence can reach 30% and since the kinematic distances toward the Galactic longitudes l = 70–80° are unreliable, we take d = 1.7 kpc as the most probable value. The masses and mean densities estimated for different parts of the SNR (the corresponding radii are indicated) by analyzing in detail the X-ray spectra with a radial-step width of 5′–10′ are given in the table. When calculating the "exact" mass, we determined the density, temperature, and absorption distributions in the plane of the sky. As we see from the table, the mass of the outer shell or the halo is approximately equal to the mass of the bright SNR G78.2+2.1.

For comparison, note that the masses estimated from the total SNR luminosity by assuming spherical and shell ($\Delta R/R \simeq 0.3$) models are 140 and $110 M_\odot$, respectively. For such a mass estimate, we took the coefficient of volume luminosity in accordance with the temperature kT = 1.4 keV and metallicity $Z = 0.27 Z_\odot$ derived above; the MEKAL model was used. The SNR shell model is seen to yield the estimate that is closest to the exact value in the table: $95 \pm 10 M_\odot$.

The temperatures $T_\mathrm{X} = 1.6 \times 10^7$ K (for ionization equilibrium plasma) and $T_\mathrm{X} = 3.2 \times 10^7$ K (in the absence of ionization equilibrium) deduced from the X-ray spectrum of the bright shell are typical of the gas behind an adiabatic shock front. The corresponding shock velocity is $V_\mathrm{s} = (1\text{–}1.5) \times 10^3$ km s^{-1}.

The mass of the postshock gas in a SNR is the principal parameter that characterizes its evolutionary status [3]; the X-ray plasma mass $M \approx 50\text{–}100 M_\odot$ suggests a transition from the phase of free expansion to the phase of adiabatic expansion (Sedov phase). Our mass estimate for the hot plasma in the entire G78.2+2.1 shell agrees with the mass determined from IRAS observations; Saken *et al.* [36] identified a spherical infrared shell with the SNR and estimated the total mass of its gas to be $M = 100 M_\odot$.

Assuming the radius R = 15 pc and the post-shock temperature $T_\mathrm{s} = (1.6\text{–}3.2) \times 10^7$ K for the standard explosion kinetic energy $E = 10^{51}$ erg, we obtain an age

of (4–6) $\times$ 10^3 years and the ambient gas density n_0 = 0.14–0.3 cm^{-3} for the SNR at the adiabatic phase in a homogeneous medium. This density is in agreement with the initial density (n_0 = 0.32 cm^{-3}) independently estimated from the mass of the infrared shell by assuming that the gas swept up from the inner volume concentrates in it.

Thus, the X-ray observations of the bright source G78.2+2.1 lead to a self-consistent model for a young SNR at an early stage of adiabatic expansion in a medium of relatively low density.

At this stage, the optical emission from the SNR must be weak: Intense radiative cooling in a homogeneous medium of density n_0 = 0.3 cm^{-3} begins considerably later, when the SNR radius, expansion velocity, and age are, respectively, $R_c \approx 30$ pc, $v_c \approx 250$ km s^{-1}, and $t_c \approx 5 \times 10^4$ years.

Indeed, as yet no bright optical shell that could be unambiguously correlated with G78.2+2.1 (or with the outer X-ray shell) has been detected. The optical emission from the SNR may be represented by weak filaments in the west with the $I(\mathrm{H}\alpha)/I([\mathrm{S\ II}])$ ratio typical of SNRs [37]. However, filaments emitting in [S II] 6717/6731 Å are clearly seen on photographs from the atlas of Parker *et al.* [38] far outside G78.2+2.1 and the weak outer shell. To reach a more definitive conclusion, we need the relative line intensities in the spectra of these filaments inside and outside the SNR. As we made sure in Subsect. 2.2, the Hα emission toward G78.2+2.1, including the filaments mentioned above, does not differ significantly in radial velocities from the emission of the nearby part of Cygnus X.

We therefore cannot rule out the possibility that the optical nebulae toward G78.2+2.1 are H II regions. This is consistent with the radio spectrum of G78.2+2.1, which exhibits variations in the spectral index attributable to the superposition of two components: Synchrotron radiation of the SNR and thermal radiation of the H II regions [4]. The contribution of thermal radio emission is largest in the region of DR4 and the bright nebula near γ Cygni [1, 11]. Here, the expanding G78.2+2.1 shell most likely collides with a dense cloud, as suggested by the sharp brightness gradient and the nonspherical plane boundary of the bright X-ray and radio shells (Fig. 4). This is also evidenced by the two small CO knots detected by Fukui and Tatematsu [39] at V(LSR) = –(3–1) and +(1–3) km s^{-1}, which closely coincide with the regions of local brightening of the radio shell and anticorrelate with the X-ray brightness.

H I observations revealed a geometrically thick, slowly expanding shell around the SNR [14, 15] and high-velocity cloudlets [15, 16]. The mean velocity of the H I shell is V(LSR) = +3 km s^{-1}, the probable expansion velocity is ~10 km s^{-1}, the mass is $8 \times 10^3 M_\odot$, the mean density is ≈2.5 cm^{-3}, and the kinetic energy does not exceed a few percent of the energy of a standard supernova explosion (10^{51} erg) [14]. As was pointed out by Gosachinskii *et al.* [14], judging by the energetics, the outer H I shell could be produced both by the supernova explosion and by the stellar wind from the supernova progenitor. Since the X-ray emission from G78.2+2.1 suggests an early adiabatic phase, the latter currently seems more justified.

The existence of an outer weak X-ray shell far outside the synchrotron radio source G78.2+2.1 and the bright X-ray SNR undoubtedly requires an observational confirmation. If the reality of the weak X-ray shell (or the halo) is confirmed, then the question of its nature and relationship to the H I shell will arise.

The coexistence of a cold H I shell and a weak outer X-ray shell of virtually the same size could be explained in principle by the fact that the supernova explosion occurred at the boundary of an extended dense cloud with a sharp density gradient. In this case, the SNR has the peculiar shape of two connected hemispheres of different sizes at different evolutionary stages because of the difference in initial ambient density. The part of the SNR in the dense gas may be represented by the bright X-ray source G78.2+2.1 and the extended H I shell produced by the progenitor's stellar wind in the cloud, while the part of the SNR in the low-density intercloud medium may be represented by the outer X-ray shell. The SNR VRO42.05.01 [40] is an example of such a structure for the direction of density gradient perpendicular to the line of sight, which is "favorable" for the observer.

If the line of sight is directed along the density gradient, we will see the X-ray and H I shells coinciding "by chance" in projection onto the plane of the sky. However, the fact that the outer X-ray shell has a lower temperature than the bright G78.2+2.1 shell is in poor agreement with this model.

An explanation of the coexistence of the H I shell and the two X-ray shells in the model of a supernova explosion in the cavity swept up by the supernova progenitor wind is of greater interest. The evolution of a SNR in a cavity has long been analyzed by many authors (see [41] and references therein). The key point here is the collision of the SNR with the dense cavity walls (before the collision, the supernova shell expands virtually without deceleration; after the collision, the radiative phase of the postshock gas sets in very rapidly). Depending on the mass ratio of the supernova shell and the shell swept up by the wind, as well as on the velocity at which the shock triggered by the supernova impinges on the cavity walls, one might expect the formation of a double X-ray shell at least in two stages. X-ray emission from the gas heated by the blast wave in the swept-up shell and from the gas behind the reflected shock in the SN ejecta can be observed at the early stage, until the mass of the postshock gas in the swept-up shell does not exceed the ejected mass by more than a factor of 40–50. In this case, the inner shell must be hotter and, under certain conditions, can be brighter than the outer one.

Subsequently, the H I shell swept up by the wind is fragmented because of the Rayleigh–Taylor instability at the contact surface between the gas behind the direct shock front and that behind the reflected shock front. As a result, an outer X-ray shell representing the gas behind the direct shock front, which has mainly passed the H I shell through breaks between its individual fragments, can be formed. The neutral hydrogen associated with the SNR G78.2+2.1 actually exhibits a distinct clumpy structure, as suggested by the small-scale ($\approx$6–10′) high-velocity H I cloudlets detected by Braun and Strom [16] and Landecker *et al.* [15].

Observations of the SNR W44 provide evidence that the H I shell swept up by the wind may turn out to be inside the SNR. Koo and Heiles [42] explained an expanding H I shell (of radius 9 pc) inside a synchrotron radio shell (of radius 15 pc) in terms of this model. The age of the pulsar associated with W44 is $\simeq 3 \times 10^4$ years; W44 exhibits a more "advanced" stage of interaction with the swept-up shell than does G78.2+2.1. Here, there are all the signatures of the radiative phase: bright optical filaments and X-ray emission with a relatively low temperature of $T_e = (4–8) \times 10^6$ K enhanced toward the center.

5. CONCLUSION

Our optical and X-ray observations of G78.2+2.1 and their comparison with radio-continuum studies and IRAS data provide evidence for a young adiabatic SNR ($M_{\mathrm{X-ray}} = 95 \pm 10 M_\odot$, $V_s \simeq 10^3$ km s^{-1}, $t \simeq (5–6) \times 10^3$ years).

In general, there is agreement between the large-scale X-ray and radio structures of G78.2+2.1; the X-ray image exhibits a shell structure ($\Delta R/R \simeq 0.3$). A comparison with the radio map at $\nu = 1.4$ GHz constructed from archival VLA data reveals the coincidence of features at the eastern SNR boundary on scales of several arcminutes.

A weak X-ray emission (an outer shell or halo) has been detected far outside the synchrotron radio source G78.2+2.1 for the first time. The outer shell size of $\simeq 2°$ is twice the size of the bright source G78.2+2.1.

We conclude that the previously identified [14, 15], slowly expanding massive H I shell around G78.2+2.1 was produced by the stellar wind from the supernova progenitor. The SNR expansion mainly took place inside the cavity swept up by the wind; the interaction with the dense walls of the swept-up shell has begun relatively recently. The formation of the weak outer X-ray shell we detected can be explained in terms of the theory of SNR evolution in the cavity swept up by the progenitor's stellar wind [41].

We emphasize that both alternatives considered in Sect. 4 to account for the outer X-ray shell and its coexistence with the H I shell are speculative so far. To elucidate the nature of the outer shell or the halo and to determine the evolutionary status of the SNR requires the following:

First, a confirmation of the existence of outer weak X-ray emission and determination of its structure: a shell or a plateau.

Second, a confirmation of the existence of an H I shell. Recall that Landecker *et al.* [15] detected an expanding H I ring around G78.2+2.1 only by observing two clouds with markedly differing radial velocities, one in emission and the other in absorption. The H I ring structure identified by Gosachinskii *et al.* [14], into which the SNR fits well in the plane of the sky, is also ambiguous. The authors pointed out that the distribution of 21-cm emission in the vicinity of G78.2+2.1 is extremely nonuniform; the western part of this shell is identified unreliably, because it is projected onto the large shell around the entire Cygnus X complex; the pattern is distorted by the emission from the bright source Cygnus A in the beam wing.

Third, special observations aimed at searching for optical emission from the SNR are required. The lower temperature of the outer X-ray shell suggests that the radiative cooling in this region may be already significant, and the optical emission can be noticeable at least in the outer region outside G78.2+2.1, if not in the SNR itself.

Fourth, and this is the key point, searches for the corresponding outer radio-continuum structure are required. Only after the radio spectrum associated with the outer X-ray shell has been determined can we elucidate its nature and, accordingly, the evolutionary status of the SNR.

ACKNOWLEDGMENTS

We used the observational data retrieved from the HEASARC archive. This study was supported by the Russian Foundation for Basic Research (project no. 98-02-16032) and the Astronomy Program (project no. 1.3.1.2).

REFERENCES

1. L. A. Higgs, T. L. Landecker, and R. S. Roger, Astron. J. **82**, 718 (1977).
2. H. L. Wendker, L. A. Higgs, and T. L. Landecker, Astron. Astrophys. **241**, 551 (1991).
3. T. A. Lozinskaya, *Supernovae and Stellar Wind in the Interstellar Medium* (AIP, New York, 1992).
4. X. Zhang, Y. Zheng, T. L. Landecker, *et al.*, Astron. Astrophys. **324**, 641 (1997).
5. S. Van den Bergh, A. P. Marcher, and Y. Terzian, Astrophys. J., Suppl. Ser. **26**, 19 (1973).
6. T. A. Lozinskaya, Astron. Zh. **52**, 515 (1975).
7. H. M. Johnson, Astrophys. J. **206**, 243 (1976).
8. V. P. Arkhipova, N. A. Gorynya, V. F. Esipov, *et al.*, Astron. Tsirk., No. 810, 4 (1974).

9. V. P. Arkhipova and T. A. Lozinskaya, Astron. Zh. **55**, 1320 (1978).
10. T. A. Lozinskaya, Pis'ma Astron. Zh. **3**, 306 (1977) [Sov. Astron. Lett. **3**, 163 (1977)].
11. J. Baars, H. R. Dickel, and H. J. Wendker, Astron. Astrophys. **62**, 13 (1978).
12. A. J. Landecker, Astron. J. **89**, 95 (1984).
13. A. Piepenbrink and H. J. Wendker, Astron. Astrophys. **191**, 313 (1988).
14. I. G. Gosachinskii, T. A. Lozinskaya, and V. V. Pravdikova, Astron. Zh., 1999 (in press).
15. T. L. Landecker, R. S. Roger, and L. A. Higgs, Astron. Astrophys., Suppl. Ser. **39**, 133 (1980).
16. R. Braun and R. G. Strom, Astron. Astrophys., Suppl. Ser. **63**, 345 (1986).
17. L. A. Higgs, T. L. Landecker, and F. D. Seward, *Supernova Remnants and Their X-ray Emission, IAU Symp. 101*, Ed. by J. Danziger and P. Gorenstein (Reidel Publ., Dordrecht, 1983), p. 281.
18. J. A. Esposito, S. D. Hunter, G. Kanbach, *et al.*, Astrophys. J. **461**, 820 (1996).
19. K. T. S. Brazier, G. Kanbach, A. Carraminana, *et al.*, Mon. Not. R. Astron. Soc. **281**, 1033 (1996).
20. J. Truemper, Adv. Space Res. **2**, 241 (1983).
21. Y. Tanaka, H. Inoue, and S. S. Holt, Publ. Astron. Soc. Jpn. **46**, L37 (1994).
22. B. E. Burke, R. W. Mountain, D. C. Harrison, *et al.*, IEEE Trans., **EED**-38, 1069 (1991).
23. S. L. Snowden, D. McCammon, D. N. Burrows, *et al.*, Astrophys. J. **424**, 714 (1994).
24. P. P. Plucinsky, S. L. Snowden, U. G. Briel, *et al.*, Astrophys. J. **418**, 519 (1993).
25. A. A. Vikhlinin, Candidate's Dissertation, IKI RAN (Space Research Inst., Russian Academy of Sciences) (Moscow, 1995).
26. S. A. Grebenev, W. Forman, C. Jones, *et al.*, Astrophys. J. **445**, 607 (1995).
27. J. J. Condon, W. D. Cotton, E. W. Greisen, *et al.*, Astron. J. **115**, 1693 (1998).
28. R. Mewe, E. H. B. M. Gronenschild, and G. H. J. Oord, Astron. Astrophys., Suppl. Ser. **62**, 197 (1985).
29. R. Mewe and J. Kaastra, *Internal SRON-Leiden Report* (1995).
30. E. Anders and N. Grevesse, Geochim. Cosmochim. Acta **53**, 197 (1989).
31. L. S. Lyubimkov, *Stellar Chemical Composition: Methods and Results of Analysis* [in Russian], Ed. by A. A. Boyarchuk (IPR Astroprint, Odessa, 1995).
32. J. P. Hughes and D. J. Helfand, Astrophys. J. **291**, 544 (1985).
33. T. A. Lozinskaya, Pis'ma Astron. Zh. **7**, 29 (1981) [Sov. Astron. Lett. **7**, 17 (1981)].
34. D. A. Green, *A Catalogue of Galactic SNRs (1996 August Version)* (Mullard Radio Astron. Obs., Cambridge, 1996).
35. A. K. Dambis, A. M. Mel'nik, and A. S. Rastorguev, Pis'ma Astron. Zh. **21**, 331 (1995) [Astron. Lett. **21**, 291 (1995)].
36. J. M. Saken, R. A. Fesen, and J. M. Shull, Astrophys. J., Suppl. Ser. **81**, 715 (1992).
37. S. Van den Bergh, Astrophys. J., Suppl. Ser. **38**, 119 (1978).
38. R. A. Parker, Th. R. Gull, and R. P. Kirshner, *An Emission-Line Survey of the Milky Way* (NASA, Washington DC, 1979).
39. Y. Fukui and K. Tatematsu, *Supernova Remnants and the Interstellar Medium, IAU Coll. 101*, Ed. by R. S. Roger and T. L. Landecker (Cambridge University, Cambridge, 1988), p. 261.
40. T. L. Landecker, S. Pineault, D. Routledge, *et al.*, Astrophys. J. Lett. **261**, L41 (1982).
41. G. Tenorio-Tagle, M. Rozyczhka, J. Franco, *et al.*, Mon. Not. R. Astron. Soc. **251**, 318 (1991).
42. B.-C. Koo and C. Heiles, Astrophys. J. **442**, 679 (1995).

Translated by V. Astakhov

Astronomy Letters, Vol. 26, No. 2, 2000, pp. 88–103. Translated from Pis'ma v Astronomicheskiĭ Zhurnal, Vol. 26, No. 2, 2000, pp. 115–132.

Optical Spectrum of the Infrared Source IRAS 23304+6147

V. G. Klochkova[1], R. Szczerba[2], and V. E. Panchuk[1]

[1] *Special Astrophysical Observatory, Russian Academy of Sciences, Nizhniĭ Arkhyz, Stavropolskiĭ kraĭ, 357147 Russia*
[2] *Copernicus Astronomical Center, Torun, Poland*

Received July 8, 1998; in final form, March 24, 1999

Abstract—Based on CCD spectra obtained with the PFES echelle spectrometer of the 6-m telescope, we have determined for the first time the effective temperature $T_{\rm eff}$ = 5900 K, surface gravity $\log g$ = 0.0, and detailed chemical composition of the faint star identified with the infrared source IRAS 23304+6147 by the model-atmosphere method. Its metallicity indicates that the object belongs to the old Galactic disk (the mean abundance of the iron-group elements V, Cr, and Fe for IRAS 23304+6147 is [X/H] = –0.61 dex). The stellar atmosphere exhibits an enhancement of carbon and nitrogen, [C/Fe] = +0.98, [N/Fe] = +1.36, and C/O > 1. Significant overabundances of lanthanides were detected: the mean [X/Fe] = +1.04 for La, Ce, Pr, Nd, and Eu. The elemental abundances suggest that the atmospheric chemical composition of IRAS 23304+6147 was modified mainly by nucleosynthesis followed by mixing. By modeling the object's spectrum, we revealed absorption features at the positions of well-known absorption diffuse interstellar bands (DIBs). An analysis of radial-velocity and intensity measurements for these DIBs leads us to conclude that, for IRAS 23304+6147, the DIBs originate mostly in its circumstellar dust envelope expanding at a velocity of about 20 km s^{-1}. Molecular C_2 Swan emission bands were detected in the object's spectrum, which also originate in the circumstellar envelope. There is a close match between the object's atmospheric effective temperatures determined independently by the model-atmosphere method and by modeling its optical and infrared energy distribution, within the accuracy of the methods. © *2000 MAIK "Nauka/Interperiodica".*

INTRODUCTION

Here, we continue to study the optical spectra of Galactic infrared sources identified with stars at the short, post-asymptotic-giant-branch (post-AGB) evolutionary stage, at which intermediate-mass stars pass into the planetary-nebula phase. Our previous results of a spectroscopic analysis of candidates for protoplanetary nebulae (PPNe) were published in a series of papers [1–9]. The definition of the class of PPN candidate objects (high-luminosity stars with evidence of mass loss and with a detached, expanding gas–dust envelope) and a list of the main observed features are given in the review by Kwok [10]. Being at the post-AGB stage, these objects are of great interest in studying the chemical evolution of stars and the Galaxy as a whole. The stars at such an advanced evolutionary stage exhibit chemical peculiarities attributable to their own history—a successive change of energy-releasing nuclear reactions accompanied by a change in the structure and chemical composition of the stellar envelope, by the mixing of matter, and by the dredge-up of nuclear-reaction products to the surface layers.

Since the peculiarities of the optical spectra for peculiar supergiants with large infrared excesses were considered in some detail in a recent review by Klochkova [2], here we only list the fundamental properties of the spectra of the objects under study. First, the spectrophotometric characteristics are abnormal. The spectral energy distribution of the program objects shows a double-peak structure because of the superposition of the optical flux from the central star and the infrared flux from its dust envelope [11]. The spectral energy distribution for IRAS 23304+6147 (hereafter referred to as IRAS 23304) is given in [12].

Second, the peculiarity of PPN optical spectra relative to the spectra of normal supergiants of the corresponding spectral types manifests itself in the presence of variable Hα emission in the PPN spectra, which is not observed in the spectra of normal supergiants. An example is given in Fig. 1, which shows a portion of one of the spectra for IRAS 23304 obtained with the 6-m telescope.

The third peculiarity that distinguishes the spectra of PPN candidates from those of classical supergiants is a superposition of the atomic spectrum typical of spectral types F and G and the molecular absorption spectrum (C_2, CN, CH) typical of cooler atmospheres. An in-depth analysis of the molecular spectra suggests that they originate in the circumstellar envelope [5, 13].

Some of the PPN candidates selected by infrared energy distributions and during optical observations with a medium spectral resolution are accessible to observations with a high spectral resolution. We drew up our program of optical observations with a high spectral resolution by using published studies in which IRAS sources were cross-correlated with star catalogs. For the observations, we selected infrared sources associated with high-luminosity stars (luminosity classes Ia, I, and II) of spectral types A–K with apparent mag-

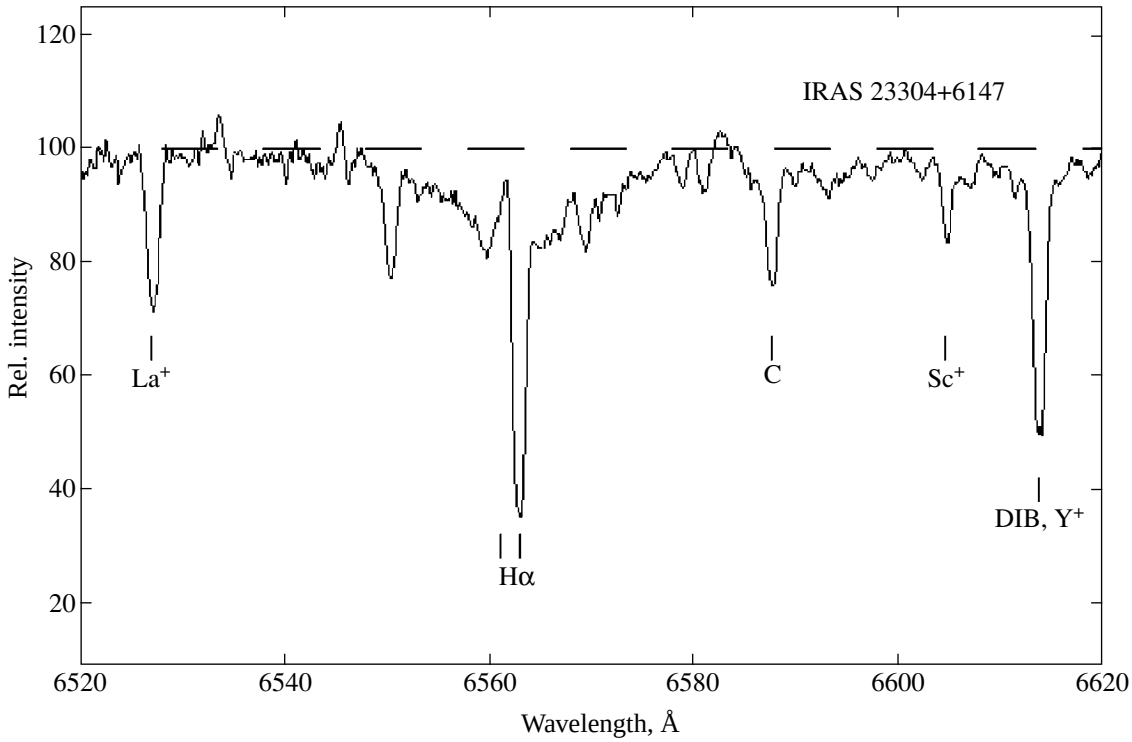

Fig. 1. IRAS 23304 spectrum near Hα. DIB is the diffuse-interstellar-band position.

nitudes (to $V \le 15^m$) accessible to high-spectral-resolution observations with the 6-m telescope.

Another criterion for selecting interesting PPN objects is the presence of features in their infrared spectra. The 21-μm emission feature was detected in the infrared spectra of several PPNe [14] and in the spectrum of IRAS 23304 [12]. The 21-μm feature is peculiar in that it was detected only in the spectra of a subclass of PPNe with carbon-rich envelopes and is unobservable in the spectra of objects at adjacent evolutionary phases. Most of the representatives of this PPN subclass are given in the review by Kwok [10]. The objects of this subclass are closely grouped together in the region of the [25–60] [12–25] infrared-color diagram between evolved carbon stars and planetary nebulae; their infrared colors are even redder than those of carbon stars [15]. In particular, IRAS 07134+1005 identified with the optically bright, peculiar supergiant HD 56126, which may be considered to be a typical representative of the PPN family with adequately studied properties [1], also belongs to this PPN subclass.

Since the PPN subclass under study is characterized by rapid mass loss accompanied by gas condensation, one might expect both quasi-periodic and secular light variations in individual objects. Having performed *BVRI* photometry of IRAS 23304 and having compared three epochs of observations, Reddy and Parthasarathy [16] concluded that the object appears to have faded appreciably in recent years; its magnitudes are $V = 13\overset{m}{.}5$ and $B = 15\overset{m}{.}8$ for JD 2449005.5. They estimated the visual absorption to be $A_V = 2.8$. Infrared and optical low-resolution spectra led Reddy and Parthasarathy [16] to conclude that IRAS 23304 is similar in observed properties to IRAS 04296+3429, whose optical spectrum was independently studied with a high spectral resolution by Klochkova *et al.* [9] and Decin *et al.* [17].

The heightened interest in this subclass of PPNe is attributable, in particular, to the correlation between the presence of a 21-μm feature in their spectra and a clear carbon overabundance in the envelopes of these objects, as suggested by CO and HCN emission features in their radio spectra. For the post-AGB stars, a carbon overabundance is expected to result from the preceding evolution and mixing of matter. This interest was rewarding after large overabundances of heavy metals synthesized in neutronization processes were detected in the atmospheres of several objects of this subclass [1, 3, 4, 9, 17–20].

There is an additional important aspect in the problem of determining the chemical composition of stars with gas–dust envelopes which is related to gas condensation on dust grains followed by selective settling of envelope material into the stellar atmosphere. These processes may well be associated with the phenomenon of semiregular light variations in RV Tau stars, among which objects with an almost complete set of properties of the subclass under discussion were found [21]. Because of the separation processes, the final chemical composition of a supergiant's surface layers depends

on a large set of physical and chemical parameters of the star itself and its envelope.

OBSERVATIONS AND DATA REDUCTION

We carried out all observations with the 6-m BTA telescope using the PFES echelle spectrometer [22] equipped with a 1040 × 1170 CCD array, which provided the spectral resolution $R = 15\,000$. On different dates (see Table 1), three spectra with a signal-to-noise ratio higher than 100 were obtained for IRAS 23304 in the wavelength range 4600–8000 or 4700–8600 Å. To calibrate the spectrograms in wavelength, we took a spectrum of an argon-filled lamp with a cathode covered with thorium salts for each exposure of the stellar spectrum.

The echelle spectra were extracted from the CCD images by using the ECHELLE context of the MIDAS-ESO system (version NOV95) in the Linux environment. To identify telluric lines in the spectra, we took a similar spectrum of a hot, rapidly rotating star on each observing night. The spectrum quality was high enough to measure the equivalent widths W with an accuracy of 10–15 mÅ, in agreement with the accuracy estimated from the formula of Cayrel de Strobel [23]. The line equivalent widths used to compute the chemical composition of IRAS 23304 are given in Table 2.

DETERMINING THE MODEL-ATMOSPHERE PARAMETERS AND CHEMICAL COMPOSITION

Since a wide spectral range was recorded simultaneously, we were able to use only the spectral criteria unaffected by interstellar and circumstellar reddening to determine the fundamental model parameters $T_{\rm eff}$ and $\log g$. We derived the effective temperature from the condition that the abundance of neutral iron was independent of the excitation potential of the corresponding lines and chose the surface gravity from the condition of ionization balance for iron atoms and the microturbulence from the condition that the iron abundance was independent of the line intensity.

When the model-atmosphere parameters are determined, it is important to restrict the analysis to low- and moderate-intensity lines. The approximation of a stationary plane-parallel atmosphere begins to "break down" from the strongest spectral features. In addition, some of the strong absorption features may originate in the circumstellar envelope, and the intensity of the shell components is included in the intensity of the atmospheric components at an insufficient spectral resolution. At the same time, the amount of matter concentrated in the cold envelope is not enough to form weak lines which emerge mostly during transitions to high excited levels [5]. For this reason, using the above criteria for the entire set of lines results in significant errors in the atmospheric parameters [21]. Studies of the molecular spectra formed in the envelopes of post-AGB stars show that the state of envelope matter cannot be described in terms of thermodynamic equilibrium with the stellar atmosphere [5, 13]. Here, we restricted the analysis to lines with $W < 0.25$ Å when determining the model-atmosphere parameters and with $W < 0.3$ Å in the subsequent calculations of elemental abundances; only for barium had we to use lines of its ions with $W \le 0.7$ Å, which were enhanced due to a considerable atmospheric overabundance of this element in the object under study.

We used the grid of standard models by Kurucz [24] to determine the fundamental model-atmosphere parameters (effective temperature $T_{\rm eff}$ and surface gravity $\log g$) and to compute the chemical composition. Oscillator strengths gf of the spectral lines used to determine the model parameters and elemental abundances are given in Table 2. We took oscillator strengths gf for most lines from the extensive list of Luck [25] and oscillator strengths for the carbon and sulfur lines from Giridhar *et al.* [26].

The effective temperature was determined from the condition that the iron abundance was independent of the lower level excitation potential of the lines used. An additional reliability criterion for the method is the lack of the same dependence for other chemical elements, which are also represented in the spectra by numerous lines (for example, C I, Ca I, Si I, Sc II, Ni I). In addition, for a reliably determined microturbulence, there is no dependence of individual abundances on the equivalent widths of the lines used in the calculations. The titanium abundances derived from lines of neutral and ionic species agree, within the accuracy of the method. This agreement provides evidence that the surface gravity was estimated correctly from the condition of ionization balance for iron atoms. In general, the internal agreement between the parameters suggests that the homogeneous model atmospheres we use are suitable for computing weak lines in the LTE approximation.

Table 1 Log of observations and heliocentric radial velocities of IRAS 23304+6147 measured from various features in its optical spectra

Spectrum	JD 2450000+	λ, Å	$V_\odot$, km s^{-1}					
			Metal lines	Hα absorption	Hα emission	$C_2(0;1)$ λ 5635 Å	Na ID	DIB
s16611	588.64	4600–8000	−24.9	−25.6	−88.7	−46.7	−31.5 −45.0	−35.8
s17504	674.48	4680–8600	−25.3	−26.9	−97.0	−50.4	−38.4	−38.3
s18212	764.49	4680–8600	−23.4	−24.9	−86.5	−50.7	−40.0	−39.7

We derived the following model-atmosphere parameters for IRAS 23304: $T_{\rm eff}$ = 5900 K, $\log g$ = 0.0, ξ_t = 6.0 km s^{-1}, and [Fe/H] = –0.65.

The typical accuracy of determining the model parameters for a star with a temperature of about 6000 K is, on the average, $\Delta T_{\rm eff} \approx 200$ K, $\Delta \log g \approx 0.3$ dex, $\Delta\xi_t \approx 0.5$ km s^{-1}. It should be borne in mind that most of the lines used to compute the chemical composition have equivalent widths up to 100–150 mÅ, which places stringent requirements on the accuracy of observational data, because at a given spectral resolution, the accuracy of W for weak lines depends mainly on the spectral signal-to-noise ratio. The elemental abundances derived from a set of lines has a small scatter; the error of the mean δ normally does not exceed 0.10–0.12 dex for more than 8–10 lines (see Table 5 below). Note that here we ignored hyperfine structure and isotopic shifts, which broaden the Ni I and Ba II lines.

MODELING THE SOURCE'S SPECTRAL ENERGY DISTRIBUTION

The method of modeling the energy distribution is detailed in [27]; we only briefly outline the salient features of the method.

The energy spectrum was modeled by solving the equation of transfer in a spherically symmetric gas–dust envelope for a set of frequencies ν with allowance for the grain size distribution and quantum heating effects for small grains.

Since IRAS 23304 belongs to carbon-rich sources [28], during our modeling we assumed the dust to consist of polycyclic aromatic hydrocarbons (PAHs) (the detailed properties of a = 5–10 Å grains are described in [27]), amorphous carbon (AC) particles with $a > 50$ Å [29], and grains from 10 to 50 Å in size, whose absorption coefficient was calculated by averaging the opacities for PAHs and AC using the formula

$$Q_{\rm abs,\,\nu} = fQ^{\rm PAH}_{\rm abs,\,\nu}(a) + (1-f)Q^{\rm AC}_{\rm abs,\,\nu}(a),$$

where f = 1 for a = 10 Å and f = 0 for a = 50 Å.

The above method of describing the dust opacity allows us to use a continuous grain size distribution and to fill the gap between carbon-containing cyclic molecules and small carbon particles.

The model parameters are given in Table 3, where the following notation is used: $(L/L_\odot)$ is the luminosity of the central star, in fractions of the solar luminosity; d is the distance to the object; $R_{\rm out}$ is the system's outer radius; $V_{\rm exp}$ is the envelope expansion velocity; $R_{\rm in}$ (hot dust envelope) is the inner radius of the hot dust envelope; $\bar{T}_{\rm d}$ [$R_{\rm in}$ (hot dust envelope)] is the mean grain temperature at the inner radius of the hot dust envelope; $\rho_{\rm gas}$ (hot dust envelope) is the radial (r) distribution of gas density in the hot dust envelope; $\dot{M}_{\rm post-AGB}$ is the mass-loss rate at the post-AGB stage; $R_{\rm in}$ (main envelope) is the inner radius of the main envelope; $\bar{T}_{\rm d}$ [$R_{\rm in}$ (main envelope)] is the mean grain temperature at the inner radius of the main envelope; $\rho_{\rm gas}$ (main envelope) is the radial (r) distribution of gas density in the main envelope; $\dot{M}^{\rm min}_{\rm AGB}$ and $\dot{M}^{\rm max}_{\rm AGB}$ are the minimum and maximum mass-loss rates at the AGB stage; a_- and a_+ are the minimum and maximum grain radii, respectively; p is the parameter of the power-law grain size distribution; $t_{\rm dyn}$ is the post-AGB envelope expansion time; and $M_{\rm dust}$ is the total mass of dust in the envelopes. More detailed information about the modeling algorithm can be found in [27].

An empirical opacity function was specified as follows. The 21-μm band was fitted by a Gaussian with the parameters (a central wavelength of 20.6 μm and a band width of 1.5 μm) determined from the modeling for IRAS 07134+1005; in the source's spectrum, this feature has a maximum intensity compared to other sources. To achieve better agreement, we increased the band intensity by 10% relative to its intensity for IRAS 07134+1005. For the 30-μm band, we used the sum of half-Gaussians of equal intensities and different widths. This was first done for IRAS 22272+5435; as a result, we obtained the following parameters: the widths of the short- and long-wavelength components are $\sigma_{\rm L}$ = 4 μm and $\sigma_{\rm R}$ = 9 μm, respectively, and the central wavelength is λ = 27.2 μm [27]. For IRAS 23304, we increased the intensity of this band by 20% and $\sigma_{\rm R}$ to 13 μm. To produce the empirical opacity function, we then added the sum of the 21- and 30-μm band profiles to the amorphous-carbon absorption curve.

The solid line in Fig. 2 indicates the solution of the transfer equation with allowance for quantum heating effects for PAH particles (the assumed parameters are given in Table 3). The best agreement was obtained for a stellar effective temperature of 5700 K, while the spectral classification G2 Ia [30] yields $T_{\rm eff}$ = 5200 K. Note that, under the assumption of $T_{\rm eff}$ = 5300 K, we can explain only the data affected by reddening.

The dashed line in Fig. 2 in the range 18–48 μm indicates the continuum level. Taking this continuum and the extents of the 21-μm and 30-μm bands from 18 to 22 and from 22 to 48 μm, respectively, we estimated the flux in the 21-μm band to be approximately 5.3% of the total infrared flux ($284L_\odot$ in the wavelength range from 5 to 300 μm for an assumed distance to the source of 1 kpc) and the flux in the 30-μm band to be approximately 26.5% of the total infrared flux.

Figure 2 shows the following observational data: the two sets of ultraviolet and visible photometric data from [12] (filled circles and squares), the near-infrared photometric observations by Hrivnak and Kwok [12] (filled circles), and infrared-band measurements (filled squares); for comparison, the filled triangles represent the data from [31]; and the filled circles represent the measured IRAS 12-, 25-, and 60-μm fluxes. The same observations corrected for reddening are indicated by

Table 2. Atomic data (lower-level excitation potentials *EP* and oscillator strengths *gf*), line equivalent widths *W* in the IRAS 23304 spectrum, and the chemical composition $A(X)$ ($A(\mathrm{H}) = 0$) computed with the model parameters $T_{\mathrm{eff}} = 5900$ K, $\log g = 0.0$, and $\xi_t = 6.0$ km s^{-1}

λ, Å	Species	*EP*, eV	log *gf*	*W*, mÅ	*A*(*X*)	λ, Å	Species	*EP*, eV	log *gf*	*W*, mÅ	*A*(*X*)
6707.75	Li I	0.00	0.06	55	–9.32	7003.57	Si I	5.96	–0.63	96	–4.50
5817.70	C I	7.68	–2.87	29	–3.58	7405.79	Si I	5.61	–0.54	175	–4.40
5912.58	C I	9.00	–2.62	05	–3.48	7849.98	Si I	6.19	–0.65	104	–4.22
6007.18	C I	8.64	–2.18	17	–3.67	7932.35	Si I	5.96	–0.47	161	–4.22
6012.21	C I	8.64	–2.30	15	–3.61	5696.63	S I	7.87	–1.21	24	–4.88
6014.84	C I	8.64	–1.71	42	–3.69	5700.24	S I	7.87	–0.98	19	–5.22
6016.45	C I	8.64	–1.82	38	–3.63	6041.92	S I	7.87	–1.00	24	–5.08
6120.81	C I	8.85	–2.42	19	–3.19	6045.99	S I	7.87	–0.79	26	–5.25
6413.55	C I	8.77	–2.00	142	–2.42	6052.63	S I	7.87	–0.63	109	–4.58
6605.80	C I	8.85	–2.31	61	–2.67	6743.58	S I	7.87	–0.70	86	–4.67
6671.82	C I	8.85	–1.65	168	–2.49	6748.79	S I	7.87	–0.44	106	–4.78
6711.30	C I	8.54	–2.47	24	–3.29	6757.16	S I	7.87	–0.29	78	–5.14
6828.12	C I	8.54	–1.51	176	–2.87	5349.47	Ca I	2.71	–0.31	45	–6.75
7100.30	C I	8.64	–1.60	168	–2.73	5581.98	Ca I	2.52	–0.56	103	–6.19
7108.94	C I	8.64	–1.68	71	–3.38	5588.76	Ca I	2.52	0.36	228	–6.29
7111.48	C I	8.64	–1.32	157	–3.09	5590.13	Ca I	2.52	–0.57	21	–7.04
7115.19	C I	8.64	–0.90	244	–2.90	5598.49	Ca I	2.52	–0.09	117	–6.57
7116.99	C I	8.65	–1.08	244	–2.71	5857.46	Ca I	2.93	0.24	65	–6.90
7119.67	C I	8.64	–1.31	242	–2.51	6102.73	Ca I	1.88	–0.79	145	–6.31
7423.64	N I	10.33	–0.61	119	–2.99	6122.23	Ca I	1.89	–0.32	169	–6.63
7442.29	N I	10.33	–0.31	116	–3.31	6162.18	Ca I	1.90	–0.09	203	–6.63
7468.31	N I	10.34	–0.13	101	–3.62	6166.44	Ca I	2.52	–1.14	64	–5.92
8216.34	N I	10.34	0.16	164	–3.73	6169.04	Ca I	2.52	–0.80	57	–6.32
8242.39	N I	10.34	–0.21	231	–2.89	6169.56	Ca I	2.52	–0.48	140	–6.04
6155.98	O I	10.74	–0.66	52	–3.05	6493.79	Ca I	2.52	–0.11	218	–5.91
6156.77	O I	10.74	–0.44	61	–3.16	6717.69	Ca I	2.71	–0.52	140	–5.83
6158.18	O I	10.74	–0.29	123	–2.69	7148.15	Ca I	2.71	0.14	207	–6.07
5682.65	Na I	2.10	–0.71	79	–6.10	5318.37	Sc II	1.36	–2.04	59	–9.61
6160.75	Na I	2.10	–1.27	78	–5.55	5357.19	Sc II	1.51	–2.21	143	–8.74
5711.10	Mg I	4.34	–1.68	103	–4.90	5552.24	Sc II	1.45	–2.27	94	–9.03
6318.71	Mg I	5.11	–1.97	39	–4.47	5640.99	Sc II	1.50	–1.01	200	–9.63
6319.24	Mg I	5.11	–2.20	55	–4.06	5667.15	Sc II	1.50	–1.20	244	–9.17
7362.28	Al I	4.02	–0.96	8	–6.00	5684.20	Sc II	1.51	–1.01	282	–9.10
7836.13	Al I	4.02	–0.29	23	–6.19	6245.62	Sc II	1.51	–0.93	226	–9.59
5665.56	Si I	4.92	–2.04	47	–4.48	6604.58	Sc II	1.36	–1.48	190	–9.42
5708.41	Si I	4.95	–1.47	194	–3.96	5173.74	Ti I	0.00	–1.06	155	–7.08
5753.65	Si I	5.61	–1.30	119	–4.00	5514.54	Ti I	1.44	–0.50	35	–7.18
5772.15	Si I	5.08	–1.75	128	–3.99	5918.55	Ti I	1.07	–1.40	10	–7.24
5793.08	Si I	4.93	–2.06	111	–3.93	5129.16	Ti II	1.89	–1.39	241	–8.18
5948.55	Si I	5.08	–1.23	195	–4.08	5185.90	Ti II	1.89	–1.35	293	–7.85
6087.79	Si I	5.87	–1.71	57	–3.83	5211.53	Ti II	2.59	–1.85	159	–7.56
6091.92	Si I	5.87	–1.40	48	–4.24	5418.80	Ti II	1.58	–2.17	249	–7.69
6125.03	Si I	5.61	–1.51	57	–4.27	6606.97	Ti II	2.06	–2.79	74	–7.73
6237.33	Si I	5.61	–1.14	99	–4.30	5928.89	V II	2.52	–1.59	68	–8.60
6243.82	Si I	5.61	–1.34	82	–4.22	5247.58	Cr I	0.96	–1.64	46	–7.17
6244.48	Si I	5.61	–1.36	63	–4.37	5296.69	Cr I	0.98	–1.40	86	–7.04
6414.99	Si I	5.87	–1.16	43	–4.54	5345.77	Cr I	1.00	–0.98	69	–7.57

Table 2. (Contd.)

λ, Å	Species	*EP*, eV	log*gf*	*W*, mÅ	*A*(*X*)	λ, Å	Species	*EP*, eV	log*gf*	*W*, mÅ	*A*(*X*)
5787.97	Cr I	3.32	–0.08	49	–6.48	6151.62	Fe I	2.18	–3.30	20	–5.06
6978.46	Cr I	3.46	0.14	83	–6.27	6173.34	Fe I	2.22	–2.88	53	–4.96
5237.35	Cr II	4.07	–1.16	226	–7.21	6191.56	Fe I	2.43	–1.60	205	–5.03
5308.46	Cr II	4.07	–1.81	159	–7.01	6219.28	Fe I	2.20	–2.43	74	–5.26
5310.73	Cr II	4.07	–2.28	139	–6.67	6230.73	Fe I	2.56	–1.28	164	–5.48
5313.61	Cr II	4.07	–1.65	198	–6.92	6246.32	Fe I	3.60	–0.96	173	–4.73
5369.36	Cr II	3.87	–2.86	47	–6.97	6254.26	Fe I	2.28	–2.48	42	–5.43
5502.07	Cr II	4.17	–1.99	155	–6.77	6256.37	Fe I	2.45	–2.62	68	–4.87
5510.73	Cr II	3.83	–2.48	125	–6.79	6265.13	Fe I	2.18	–2.55	77	–5.13
5223.19	Fe I	3.63	–2.39	5	–5.19	6302.49	Fe I	3.69	–1.16	71	–5.13
5253.46	Fe I	3.28	–1.67	48	–5.19	6380.75	Fe I	4.19	–1.40	28	–4.91
5281.79	Fe I	3.04	–1.02	131	–5.44	6393.60	Fe I	2.43	–1.62	127	–5.49
5307.36	Fe I	1.61	–2.99	56	–5.38	6411.65	Fe I	3.65	–0.82	115	–5.19
5322.04	Fe I	2.28	–3.03	22	–5.16	6419.98	Fe I	4.73	–0.24	39	–5.40
5364.87	Fe I	4.45	0.22	129	–5.37	6430.85	Fe I	2.18	–2.01	108	–5.47
5373.71	Fe I	4.47	–0.86	22	–5.28	6592.91	Fe I	2.73	–1.60	117	–5.29
5389.48	Fe I	4.42	–0.41	57	–5.31	6609.12	Fe I	2.56	–2.69	30	–5.13
5391.46	Fe I	4.15	–0.94	27	–5.40	6677.99	Fe I	2.69	–1.47	136	–5.34
5398.29	Fe I	4.45	–0.67	90	–4.75	5132.66	Fe II	2.81	–4.18	112	–5.40
5400.50	Fe I	4.37	–0.16	132	–5.04	5136.80	Fe II	2.84	–4.49	58	–5.46
5410.91	Fe I	4.47	0.28	162	–5.19	5414.05	Fe II	3.22	–3.79	128	–5.30
5415.20	Fe I	4.39	0.50	246	–4.91	5425.25	Fe II	3.20	–3.36	185	–5.41
5424.07	Fe I	4.32	0.52	249	–4.96	6084.10	Fe II	3.20	–3.98	102	–5.32
5445.04	Fe I	4.39	–0.02	123	–5.23	6113.33	Fe II	3.22	–4.31	133	–4.77
5473.90	Fe I	4.15	–0.76	58	–5.19	6149.25	Fe II	3.89	–2.92	197	–5.12
5501.46	Fe I	0.96	–2.95	176	–5.27	6238.38	Fe II	3.89	–2.87	237	–4.92
5522.46	Fe I	4.21	–1.55	8	–5.30	6369.46	Fe II	2.89	–4.36	160	–4.89
5554.89	Fe I	4.55	–0.44	86	–4.91	6383.72	Fe II	5.55	–2.27	82	–4.96
5565.71	Fe I	4.61	–0.29	81	–5.05	6416.92	Fe II	3.89	–2.85	230	–4.99
5569.62	Fe I	3.42	–0.54	194	–5.17	6432.68	Fe II	2.89	–3.74	238	–5.05
5615.64	Fe I	3.33	–0.14	219	–5.50	6516.08	Fe II	2.89	–3.45	286	–5.02
5624.54	Fe I	3.42	–0.90	96	–5.44	7479.69	Fe II	3.89	–3.88	43	–5.29
5686.53	Fe I	4.55	–0.63	55	–4.99	7515.79	Fe II	3.90	–3.68	131	–4.79
5753.12	Fe I	4.26	–0.76	61	–5.07	7711.71	Fe II	3.90	–2.74	214	–5.23
5760.35	Fe I	3.64	–2.49	10	–4.79	5115.40	Ni I	3.83	–0.11	57	–6.51
5762.99	Fe I	4.21	–0.45	86	–5.22	5587.87	Ni I	1.93	–2.14	98	–5.97
5806.73	Fe I	4.61	–1.05	15	–5.15	5593.74	Ni I	3.90	–0.84	25	–6.15
5816.36	Fe I	4.55	–0.68	34	–5.19	5682.20	Ni I	4.11	–0.47	45	–6.04
5859.61	Fe I	4.55	–0.60	51	–5.06	5754.68	Ni I	1.93	–2.33	31	–6.41
5883.84	Fe I	3.96	–1.36	25	–5.21	5847.00	Ni I	1.68	–3.21	20	–5.99
5916.25	Fe I	2.45	–2.99	32	–4.88	6086.29	Ni I	4.27	–0.53	42	–5.87
5930.17	Fe I	4.65	–0.23	71	–5.15	6108.12	Ni I	1.68	–2.45	85	–6.02
5976.78	Fe I	3.94	–1.38	25	–5.20	6111.06	Ni I	4.09	–0.87	23	–5.99
5987.06	Fe I	4.79	–0.59	54	–4.81	6767.77	Ni I	1.83	–2.17	45	–6.53
5997.78	Fe I	4.61	–1.05	17	–5.10	7122.24	Ni I	3.54	0.04	88	–6.72
6003.03	Fe I	3.88	–1.12	53	–5.14	5218.21	Cu I	3.82	0.27	81	–7.82
6078.49	Fe I	4.79	–0.38	76	–4.83	6362.35	Zn I	5.79	0.27	76	–7.32
6094.42	Fe I	4.65	–1.94	3	–4.94	5119.11	Y II	0.99	–1.36	283	–9.30

Table 2. (Contd.)

λ, Å	Species	*EP*, eV	log*gf*	*W*, mÅ	*A*(*X*)	λ, Å	Species	*EP*, eV	log*gf*	*W*, mÅ	*A*(*X*)
5123.21	Y II	0.99	–0.82	256	–10.05	5330.58	Ce II	0.86	–0.23	172	–10.21
5728.89	Y II	1.84	–1.12	236	–9.11	5472.30	Ce II	1.24	–0.18	95	–10.34
5735.71	Zr I	0.00	–0.39	13	–9.22	5610.24	Ce II	1.04	0.00	200	–10.13
6025.44	Zr I	0.15	–1.32	10	–8.28	5219.03	Pr II	0.79	–0.24	211	–10.25
6127.48	Zr I	0.15	–1.06	8	–8.65	5322.82	Pr II	0.48	–0.54	152	–10.61
6134.57	Zr I	0.00	–1.28	8	–8.57	5276.88	Nd II	0.86	–0.61	217	–9.74
6143.18	Zr I	0.07	–1.10	18	–8.32	5416.38	Nd II	0.86	–0.93	65	–10.36
6762.36	Zr I	0.00	–1.09	08	–8.79	5485.71	Nd II	1.26	–0.12	245	–9.68
5853.67	Ba II	0.60	–1.00	489	–8.94	5842.39	Nd II	1.28	–0.60	191	–9.53
6141.71	Ba II	0.70	–0.08	698	–8.66	6031.31	Nd II	1.28	–0.70	23	–10.72
6496.90	Ba II	0.60	–0.38	653	–8.74	6034.23	Nd II	1.55	–0.53	34	–10.44
5377.06	La II	2.29	0.40	112	–10.57	6049.51	Eu II	1.28	–0.80	21	–11.55
5808.31	La II	0.00	–2.08	151	–10.17	6437.64	Eu II	1.32	–0.28	68	–11.47
5117.17	Ce II	1.39	0.13	153	–10.13	6645.13	Eu II	1.38	0.20	143	–11.42
5187.46	Ce II	1.20	0.20	220	–10.00						

Table 3. Model parameters for the IRAS 23304+6147 envelopes

Parameter	Value
$T_{\rm eff}$	5700 K
$\log L/L_\odot$	3.92
d	4.7 kpc
$R_{\rm out}$	0.5 pc
$V_{\rm exp}$	15.5 km s^{-1}
$R_{\rm in}$ (hot dust envelope)	8.6×10^{-4} pc
$\bar{T}_{\rm d}$ [$R_{\rm in}$ (hot dust envelope)]	670 K
$\rho_{\rm gas}$ (hot dust envelope)	$\sim r^{-2.0}$
$M_{\text{post-AGB}}$	$5\times10^{-7}\,M_\odot$ years
$R_{\rm in}$ (main envelope)	1.28×10^{-2} pc
$\bar{T}_{\rm d}$ [$R_{\rm in}$ (main envelope)]	205 K
$\rho_{\rm gas}$ (main envelope)	$\sim r^{-2.6}$
$\dot{M}_{\rm AGB}^{\rm min}$	$3.70\times10^{-5}\,M_\odot$ years^{-1}
$\dot{M}_{\rm AGB}^{\rm max}$	$3.36\times10^{-4}\,M_\odot$ years^{-1}
a_-	5 Å
a_+	0.25 μm
p	3.7
$t_{\rm dyn}$	800 years
$M_{\rm dust}$	$0.0112M_\odot$

open symbols. In addition, the thin solid line in the wavelength range 10 to 50 μm represents the Kuiper Airborne Observatory spectrum [28] supplemented with observations with the IRAS low-resolution spectrometer (LRS). Also shown here are two sets of photometric data (in the bands from *B* to *M*) corrected for interstellar extinction using the average absorption law of Cardelli *et al.* [32] under the assumption that the total *V* absorption is between $1\overset{m}{.}5$ and $2\overset{m}{.}5$ (the figure shows the minimum and maximum values in each band). These absorption estimates can be taken from [33].

It is important to emphasize that the effective temperature of IRAS 23304, $T_{\rm eff}$ = 5700 K, obtained by modeling the source's optical and infrared spectral energy distribution is in good agreement with the temperature $T_{\rm eff}$ = 5900 K that we independently determined from the degree of excitation of Fe I lines.

DISCUSSION OF RESULTS

Let us consider in more detail some of the features that we identified by analyzing the optical spectrum of IRAS 23304.

Emission Features

As was already noted above, the Hα profile in PPN spectra is distorted by emission. In turn, the emission profile is deformed by absorption in the layers above the emission-component formation regions. The radial velocities corresponding to the absorption component of the Hα profile and the blueshifted emission feature are given in Table 1. Clearly, interpretation of the posi-

tion measurements for the emission-component remnants in terms of the "emission-component radial velocity" depends on the position of the emission feature on the atmospheric-absorption wing, on the position of the absorption-line center in the overlying layers relative to the emission-component center, and on the intensity ratios of all the three components. We therefore attach no clear physical meaning to the position measurements for the emission-component remnants (when they are made within the atmospheric Hα absorption profile). It is important to emphasize that the shape of the complex Hα profile in PPN spectra is variable with a characteristic time scale of several days [2].

Radio observations of molecular transitions allow us to measure the velocity of the "star + envelope" system's center and to estimate the envelope expansion velocity from the line width. This velocity can also be estimated independently from optical spectral features that originate in the atmosphere and in the envelope. It may well be that, in combination with estimation of the parameters of the layers which form (and distort) the Hα emission, such measurements can help construct a full picture of stratification in the atmosphere and the envelope.

Let us now turn to optical manifestations of the envelope. We pointed out above that absorption molecular bands were found in the optical spectra of individual PPNe against the background of the spectrum typical of an F, G supergiant. Klochkova and Panchuk [5] showed that the intensity of TIO bands in the spectrum of IRAS 07331+0021 could not be explained in terms of the model atmosphere that described atomic lines well. The temperature of the outer atmospheric layers corresponding to the intensity of these bands must be appreciably lower. An alternative is the formation of the TIO absorption spectrum in the envelope. Bakker *et al.* [13] detected Swan and Phillips C_2 absorption molecular bands and red CN absorption molecular bands in the spectra of ten of the sixteen post-AGB stars studied by them and concluded that these molecular spectra originated in the circumstellar gas–dust envelope. The emission in the Phillips C_2 molecular (1; 0) band was detected only in RAFGL 2688. We also emphasize the conclusion of Bakker *et al.* [13] that absorption molecular bands of the above carbon-containing molecules are observed in the optical spectra of all the known objects with the 21μm feature. Before we began our systematic studies of PPNe with the 6-m telescope, we knew only three observations of emission molecular features in PPN optical spectra: Crampton *et al.* [34] detected and identified the Swan C_2 molecular (0; 0) and (0; 1) bands in the spectrum of the nebula RAFGL 2688 (Egg nebula); Schmidt *et al.* [35] detected emission bands in the spectral range 5600–6600 Å in the nebula RAFGL 915 (Red Rectangle), which were subsequently identified with diffuse interstellar bands (DIBs); and CH^+ emission lines were detected [36] and identified [37] in the object's blue spectrum.

Table 4. Equivalent widths of diffuse absorption bands normalized to unit reddening [$W/E(B–V)$, Å mag^{-1}] for different objects

Object \ λ, Å	6177	6196	6269	6284
IRAS 23304+6147	0.38	0.38	0.27	1.75
Dif	0.50	0.05	0.13	1.20
GMC	0.34	0.02	0.04	0.85

Table 5. Chemical composition of IRAS 23304+6147 [for $\log\epsilon(X) = 12.0$]. Here, n is the number of lines used, and δ is the error of the mean abundance for a given number of lines. The elemental abundances in the solar photosphere were taken from [48]; for lithium, we use its abundance in meteorites

Sun		IRAS 23304				
X	$\log\epsilon(X)$	X	$\log\epsilon(X)$	n	δ	[X/Fe]
Li	3.31	Li I	2.68	1		+0.01
C	8.55	C I	8.89	18	0.11	+0.98
N	7.97	N I	8.69	5	0.17	+1.36
O	8.87	O I	9.03	3	0.14	+0.80
Na	6.33	Na I	6.18	2		+0.49
Mg	7.58	Mg I	7.52	3	0.24	+0.58
Al	6.47	Al I	5.90	2		+0.07
Si	7.55	Si I	7.79	17	0.05	+0.88
SI	7.21	S I	7.05	8	0.09	+0.48
Ca	6.36	Ca I	5.64	15	0.10	–0.08
Sc	3.17	Sc II	2.71	8	0.12	+0.18
Ti	5.02	Ti I	4.56	3	0.05	+0.18
		Ti II	4.20	5	0.10	–0.18
V	4.00	V II	3.40	1		+0.04
Cr	5.67	Cr II	5.09	7	0.07	+0.06
Fe	7.50	Fe I	6.85	57	0.03	–0.01
		Fe II	6.88	16	0.06	+0.02
Ni	6.25	Ni I	5.80	11	0.09	+0.19
Cu	4.21	Cu I	4.18	1		+0.61
Zn	4.60	Zn I	4.68	1		+0.76
Y	2.24	Y II	2.51	3	0.29	+0.91
Zr	2.60	Zr I	3.36	6	0.14	+1.40
Ba	2.13	Ba II	3.22	3	0.08	+1.73
La	1.22	La II	1.63	2	0.20	+1.05
Ce	1.55	Ce II	1.84	5	0.06	+0.93
Pr	0.71	Pr II	1.57	2		+1.50
Nd	1.50	Nd II	1.92	6	0.20	+1.06
Eu	0.51	Eu II	0.52	3	0.04	+0.65

The above two objects belong to systems in which the light from their central parts (the star and the inner regions of the circumstellar envelope) is heavily absorbed in the gas–dust disk and scattered by dust grains of the bipolar structure. Assume that objects must be encountered with an orientation for which the object's central part is obscured from the observer by a dust disk. The absorption of light from the central star then decreases tens and hundreds of times, and the

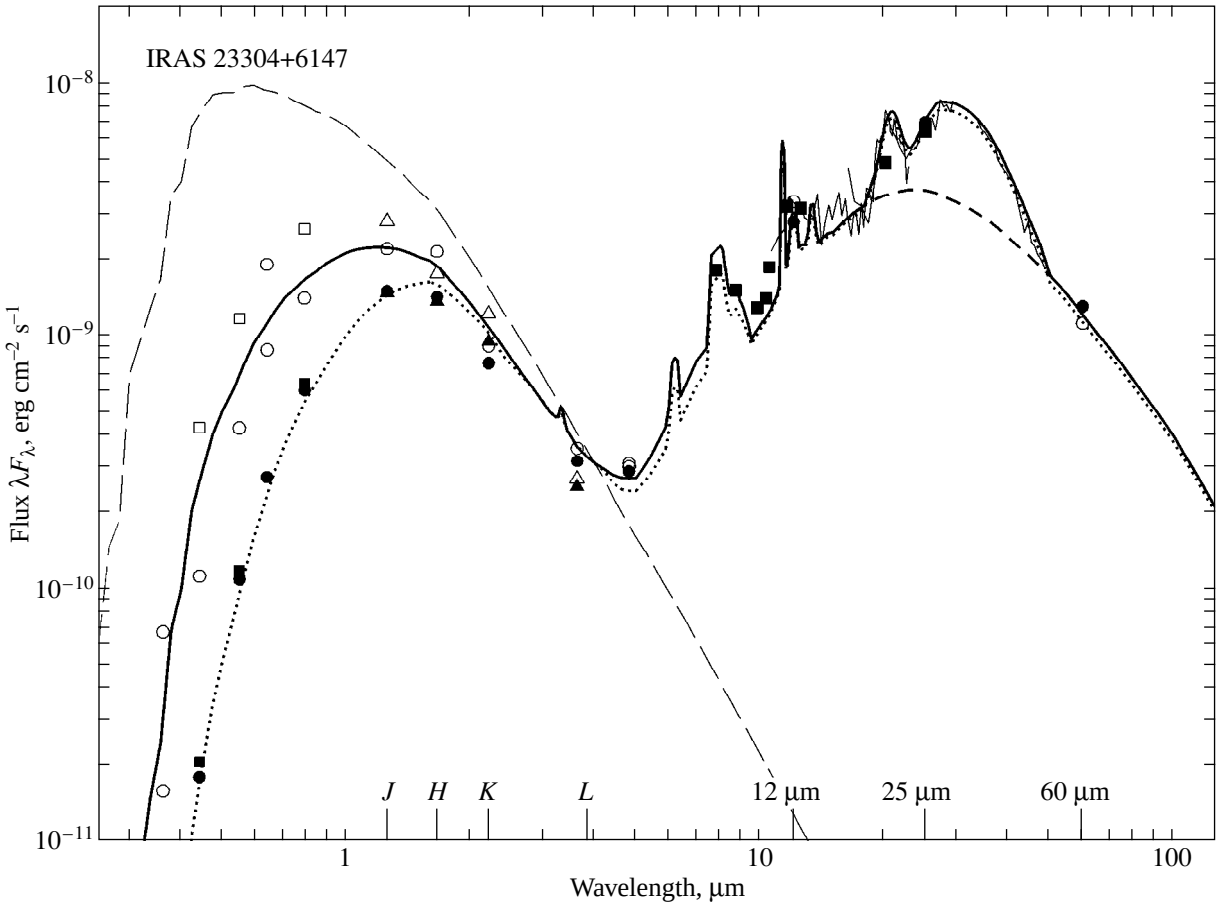

Fig. 2. Spectral energy distribution of IRAS 23304 modeled by using an empirical opacity function with allowance for quantum heating effects (solid line) and by assuming that the stellar radiation corresponds to a theoretical model with $T_{\rm eff}$ = 5700 K and $\log g$ = 0.5 (dashed line up to 12 μm). The dotted line represents the radiation for a theoretical model with $T_{\rm eff}$ = 5300 K. The notation for the observational data is given in the text.

bipolar structure in the neighborhood of the bright star becomes barely detectable. By observing the system's spectrum in this orientation, we can record both absorption and emission spectra belonging to the same molecular species. The former case is realized when the photospheric emission dominates over the envelope emission, and the latter case is realized when the envelope emission dominates.

Based on echelle spectra from the 6-m telescope, Klochkova *et al.* [9] detected strong Swan emission bands in the spectrum of IRAS 04296+3429, which belongs to the group of carbon-rich PPNe with the 21μm feature. Subsequently, a systematic search for these bands was conducted, and they were detected in two more objects: IRAS 22223+4327 [2] and IRAS 23304+6147 (Fig. 3). Notice that all these objects, including RAFGL 2688, belong to the fainter part of the list of PPNe under study (their magnitudes are $V = 13$–15^m); in the fainter objects (IRAS 04296+3429 and RAFGL 2688), the emission-band intensity (in fractions of the continuum intensity) turns out to be higher. RAFGL 2688, where the central object is obscured by a dust disk, has the highest relative intensity of the Swan emission bands. It would therefore be natural to assume that not the differences in emission intensity but primarily the differences in the degree of absorption of light from the central object underlie the phenomenon.

Most spectroscopically monitored objects in our list exhibit a time-varying intensity of the Hα emission. It may therefore well be that the emission in the Swan bands is also variable with time. However, the effect attributable to the different angular sizes of the star and the envelope must be kept in mind here. Of the four above objects in which such emission was detected, one (RAFGL 2688) clearly shows an extended structure (several arcseconds). A similar structure, which is unobservable because of the contrast associated with a different orientation of the dust disk (see above), may also be in other objects. It is important to emphasize that the angular sizes of such envelopes no longer allow them to be considered as pointlike objects. In this case, the flux from the envelope recorded through a spectrometer slit with characteristic sizes of one arcsecond is virtually independent of the seeing at the time of

observation, whereas the flux recorded from a pointlike object (stellar atmosphere) is inversely proportional to the seeing-disk diameter.

It should be noted that a weak emission feature, which we identified with the Swan 5635 Å (0;1) band head, is observed in the complex spectrum of the nebula RAFGL 915 [35] against the background of extended red emission. Thus, the number of post-AGB objects in which C_2 molecular emission bands were detected reaches five: RAFGL 915, RAFGL 2688, IRAS 04296+3429, IRAS 22223+4327, and IRAS 23304+6147.

Absorption Features Identified with Diffuse Interstellar Bands

We invoked the mechanism of resonance fluorescence [9] to explain the intensity ratios of the Swan (1; 0), (0; 0), and (0; 1) emission bands in the spectrum of IRAS 04296+3429. We assumed that there was a medium between the stellar atmosphere and the envelope emission-feature region in which selective absorption (reddening) of the light from the stellar atmosphere exciting carbon molecules occurs. Below, we present new observations which support this hypothesis.

Some of the emission bands detected by Schmidt *et al.* [35] in the spectrum of the nebula RAFGL 915 were identified by Sarre *et al.* [38] with absorption diffuse interstellar bands (DIBs) in the spectrum of the standard HD 183143. It therefore seems natural to search for circumstellar absorption features at the DIB positions. We found such DIBs in several cool post-AGB objects; below, we describe only the IRAS 23304 spectrum.

Figures 4a and 4b show two portions of the IRAS 23304 spectrum with the strongest DIBs and the synthetic spectra that we computed by using the STARSP code [39] for a model with the parameters and chemical composition determined for IRAS 23304. The vertical lines mark the DIB positions listed in [40].

To determine whether our list of atomic lines is complete and whether the model description of the atmospheric spectrum is proper, Fig. 5 compares the observed and synthetic spectra in the wavelength range which, judging by numerous studies of DIBs in the spectra of highly reddened hot stars, can be assumed to be relatively free from these features [40]. The nonideal match between the observed and theoretical spectra is explained by incompleteness of our line list, by the scatter of experimental oscillator strengths, by inaccuracy of the model fit, and by several other factors, whose analysis is the subject of a separate study. Here, it is important for us to establish whether the detection of DIBs is reliable (which can be determined by subtracting the synthetic spectrum from the observed one in a spectral range where strong DIBs are expected to be present).

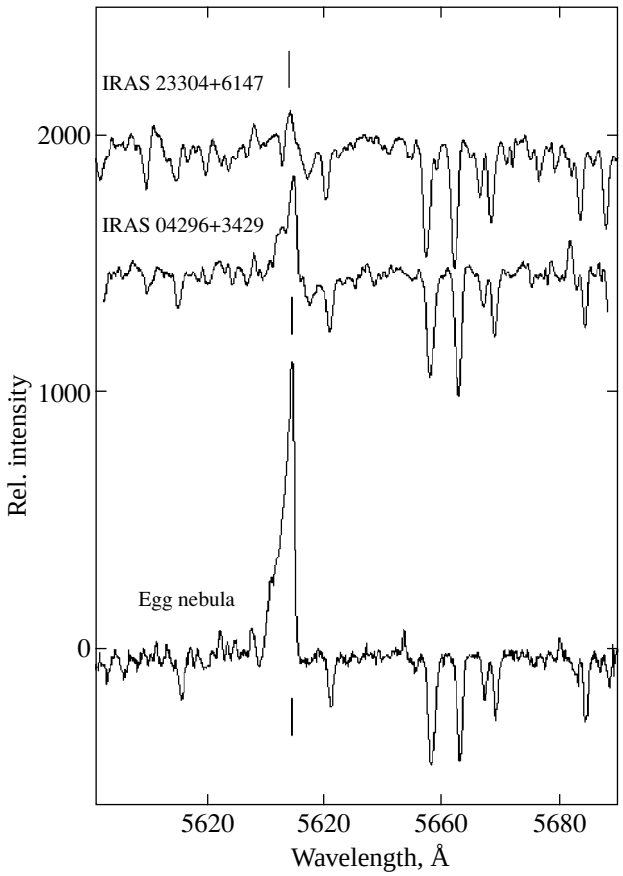

Fig. 3. Spectra of three objects near the Swan C_2 λ5635 Å molecular (0;1) band.

Searches for DIBs in the spectra of evolved stars have already been made. Cohen and Jones [41] detected DIBs in the spectrum of a highly reddened planetary-nebula nucleus (WC11, IRAS 21282+5050). Le Bertre and Lequeux [42] analyzed a sample of stars with evidence of mass loss and, having confirmed the results of Cohen and Jones [41] for IRAS 21282+5050, also detected DIBs in the spectra of IRC+10420 and AC Her. Recall that IRC+10420 is an object that rapidly evolves toward the WR stage [8] and that the chemical composition of the semiregular variable AC Her corresponds by all signs to the subgroup of cool post-AGB stars at the PNN phase under study [21]. However, no DIBs were detected in the spectra of two hot post-AGB stars: HR 4049 (B9 I) and HD 213985 (B9 I) [42].

All the seven cool post-AGB objects (IRAS 04296+3429, IRAS 05381+1012, IRAS 07134+1005, IRAS 22223+4327, IRAS 22272+5435, IRAS 23304+6147, and RAFGL 2688) in whose BTA spectra we reliably detected DIBs exhibit the 21-μm emission feature in the infrared spectra. As far as we know, as yet no detailed studies of the infrared spectrum have been carried out for the semiregular variable AC Her, whose spectrum also exhibits DIBs. Notice a possible relationship between circumstellar absorption bands and

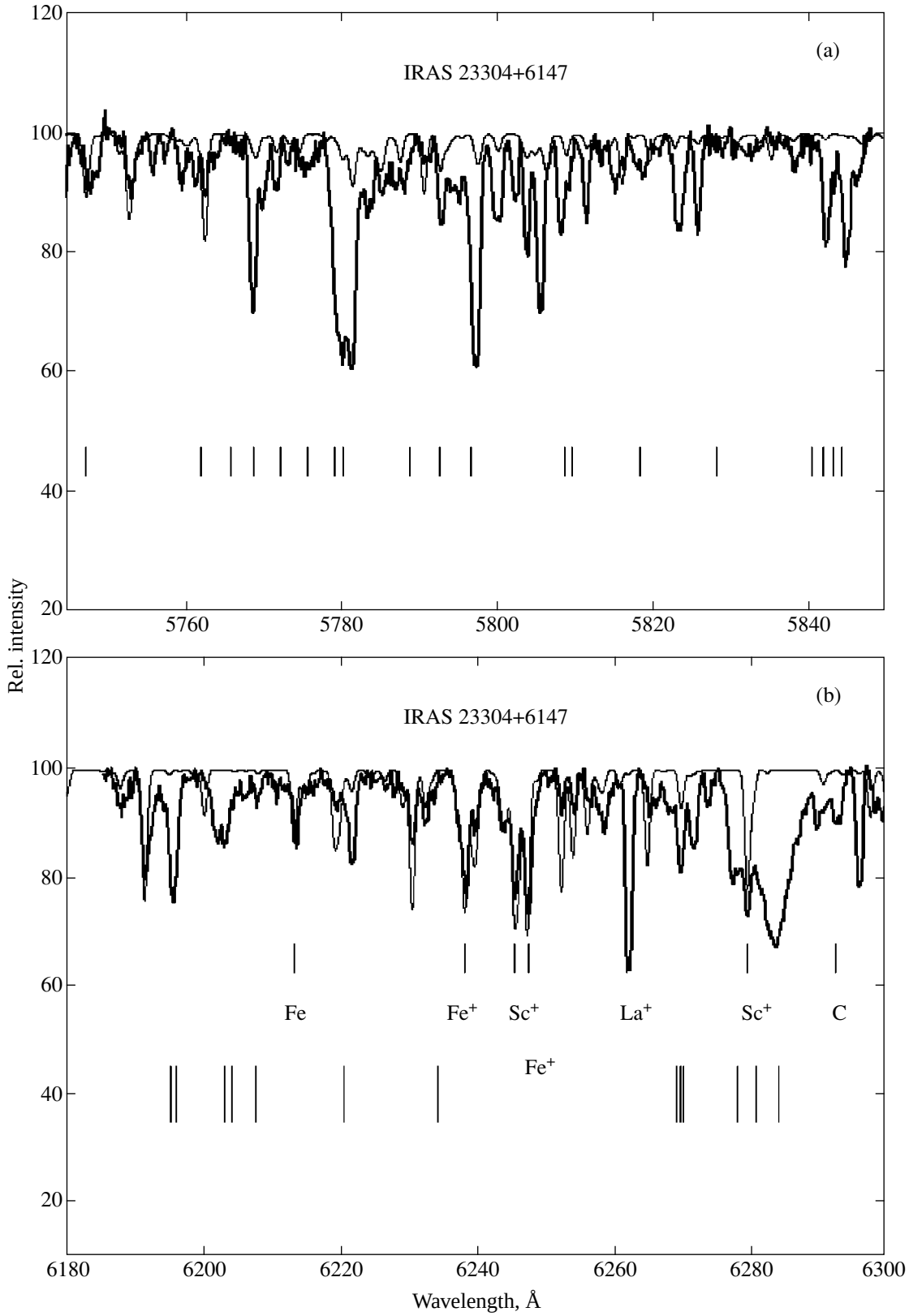

Fig. 4. Comparison of the observed (heavy line) and theoretical (thin line) spectra for IRAS 23304 near the λ5780 Å (a) and λ6280 Å (b) bands. The vertical lines (with no indication of a chemical element) mark the positions of known DIBs from [40].

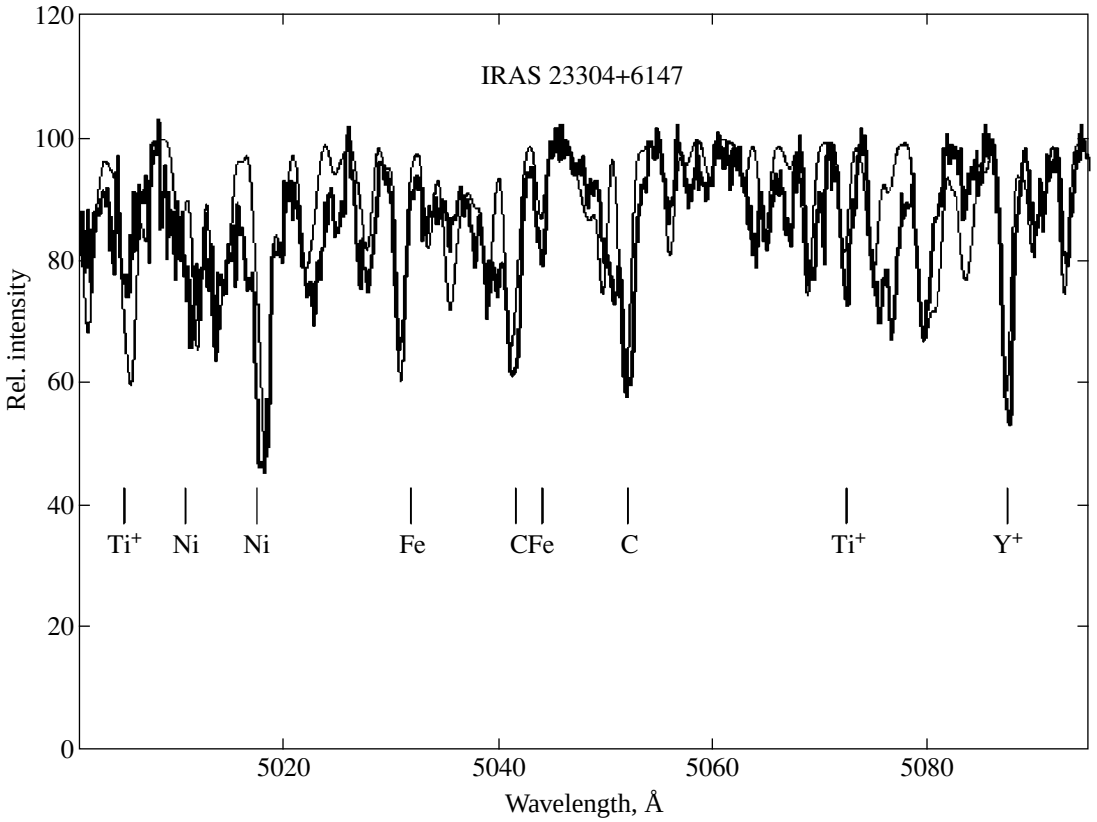

Fig. 5. Same as Fig. 4 in a region free from known DIBs.

the 21μm emission feature observed in the infrared spectra of those PPNe which show evolutionary changes in chemical composition. This circumstance may have a direct bearing on the problem of DIBs carriers, which has not yet been completely solved [43].

Attempts to group the DIBs into families within each of which the relative behavior of the DIBs and other interstellar features is more correlated in nature than that of the DIBs belonging to different families is one of the main ways of solving the problem of DIB identification [44, 45]. Apart from cross correlations of the DIB intensities, the change of the DIB equivalent width normalized to the reddening (or to the total absorption) with its value to which the normalization was made [$E(B–V)$ or A_V] is known to be nonmonotonic. For example, two types of dependence of the normalized DIB intensity on absorption were distinguished in the Orion direction [46]. For stars with a small reddening [$E(B–V) < 0\overset{m}{.}08$) in front of the gas–dust complex, $W/E(B–V)$ increases with $E(B–V)$. For large reddenings, when much of the hydrogen is in molecular form, the normalized intensities of all DIBs decrease with increasing reddening. In addition, the normalized DIB intensity for a diffuse (cloudless) interstellar medium is known to be constant with increasing value to which the normalization was made. Thus, the dependences of the normalized DIB intensities on reddening (absorption) were established for different types of interstellar-medium structure. If we estimate the reddening for post-AGB stars, then it becomes possible to compare the behavior of the normalized DIB intensities in their spectra with similar dependences for the interstellar medium.

We measured the equivalent widths of several DIBs in the IRAS 23304 spectrum. Table 4 gives the results of our measurements and the equivalent-width normalization to $E(B–V) = 0\overset{m}{.}93$, which corresponds to $A_V = 2\overset{m}{.}8$, as estimated by Reddy and Parthasarathy [16]. Table 4 also gives the means for a diffuse interstellar medium (Dif) and for a giant molecular cloud (GMC), as derived by Jenniskens *et al.* [46]. The normalized DIB intensities in the IRAS 23304 spectrum are, on the average, higher that those for the diffuse interstellar medium and even higher than those for the passage of light through the giant molecular cloud where the DIBs are weaker. We conclude that, in the direction of IRAS 23304, the conditions that ensure the relationship between the reddening and the DIB intensity differ both from the conditions in the diffuse interstellar medium and from those in the giant molecular cloud.

The very fact that the spectra of some post-AGB stars at high Galactic latitudes contain DIBs points to their circumstellar nature. For IRAS 23304, this is suggested more strongly by a comparison of the radial

velocities as measured from DIBs and from atmospheric absorption features (see below).

Radial Velocities

Our radial-velocity measurements from individual spectrograms are given in Table 1. We selected unblended lines (40–70 lines in each spectrogram) to measure the radial velocities by comparing the observed spectrum with the corresponding synthetic one. The position zero point of each spectrogram was determined by the standard method, by referencing to the positions of ionospheric emission features of the night sky and a telluric absorption spectrum, which are observed against the background of the object's spectrum. The error in the radial velocity measured from a single spectral line is about $\sigma = 1.2$ km s^{-1}. The mean velocity obtained from numerous unblended metal lines for all times of our observations is in good agreement with the system's heliocentric velocity $V_{sys} = -25.8$ km s^{-1} determined from radio observations [47] by using the shift of the center of the CO line profile. As follows from the data in Table 1, within the above error limits, the shift of the Hα absorption component agrees with the metal-line positions.

The positions of asymmetric C_2 molecular emission band heads at a given spectral resolution are determined with a lower accuracy, but we can argue with confidence that the molecular-emission regions move outward more rapidly (approximately by 20 km s^{-1}) than do the photospheric-absorption regions. When the resonance sodium doublet is resolved into atmospheric and circumstellar components (spectrum s16611), the radial velocity of the circumstellar component, within the error limits of the method, matches the radial velocity as inferred from molecular emission features. It follows from Table 1 that the circumstellar envelope is the formation region of the absorption features identified with DIBs. Note that the difference between the system's velocities is estimated to be 15.5 km s^{-1} (from the CO radio observations by Woodsworth *et al.* [47]) and 14 km s^{-1} (from the shell absorption features measured by Bakker *et al.* [13]), in agreement with our estimate of 20 km s^{-1} independently obtained from other optical spectral features.

We emphasize that it would be unreasonable to expect a close match between the measured radial velocities for the atmosphere and the envelope. First, high-resolution spectra revealed radial-velocity shifts of molecular absorption features originating in the envelope relative to atmospheric spectral lines [13]. Second, the positions of DIBs may be a function of the characteristics of the medium in which they are formed. We know a case where the positions of sharp features in the emission spectrum of DIBs are not firmly fixed on the wavelength scale. Sarre *et al.* [38] showed the positions and widths of the three strongest emission features in the RAFGL 915 spectrum identified with DIBs to be a function of the distance of the nebular region under study from the exciting star. The positions of the emission features originating in the colder distant nebular regions were shown to correspond more closely to the DIB positions. If the analogy is extended to the formation of the DIB absorption spectrum in a circumstellar envelope with a gradient in velocity and other characteristics, one should not expect a close match between the radial velocities of the circumstellar envelope determined from the corresponding sodium-doublet components and the velocities determined from DIBs whose positions were taken from studies of the interstellar medium.

Noteworthy is the presence of emission in the Hα profile, which is blueshifted from the system's velocity approximately by 75 km s^{-1}, suggesting the existence of a high-velocity stellar-wind component in IRAS 23304.

Chemical Composition

The elemental abundances $\log\varepsilon(X) \pm \delta$ averaged over the set of measured lines are listed in Table 5. The second column in this table gives the corresponding data [48] for the solar atmosphere, which we used to determine

$$[X/\mathrm{Fe}] = [\log\varepsilon(X) - \log\varepsilon(\mathrm{Fe})]_* - [\log\varepsilon(X) - \log\varepsilon(\mathrm{Fe})]_\odot,$$

required to analyze the abundance pattern at various metallicities. Below, we consider the abundance pattern in the stellar atmosphere in more detail.

The atmospheric iron in IRAS 23304 is appreciably underabundant compared to the solar one: [Fe/H] = –0.65 dex. The derived abundances of iron-group elements (vanadium and chromium) correspond to this value of [Fe/H], in agreement with the behavior of these elements in a wide range of metallicities [49]. The mean abundance of the iron-group elements V, Cr, and Fe for IRAS 23304 is [X/H] = –0.61 dex. This metallicity suggests that the object belongs to the old (thick) Galactic disk. Recall that this type of population is characterized by a scale height of ~1.3 pc and the mean metallicity [Fe/H] = –0.6 dex at a dispersion of 0.3 dex [50].

Since the object under study is at the stage of intense mass transfer between the atmosphere and the circumstellar gas–dust envelope, it should first be established how the chemical elements which undergo condensation to a varying degree behave. The atmospheric abundance of a chemical element depends on the condensation temperature of its atoms on envelope grains. As a result, Fe, Mg, Si, and Ca may be significantly underabundant, while the CNO elements, S, and the iron-group element Zn are virtually unaffected by fractionation [51]. Whereas an appreciable fraction of iron nuclei condense on grains, there is an underabundance of gas-phase iron nuclei in the atmosphere. In this case, normalizing the chemical-composition determinations to the gas-phase iron abundance results in relative over-

abundances of the elements which undergo condensation to a lesser degree.

The sulfur overabundance [S/Fe] = +0.48 as inferred with a high accuracy from a set of lines and the less reliable (from one line) zinc overabundance [Zn/Fe] = +0.76 are clearly seen in the pattern of atmospheric elemental abundances in IRAS 23304. The zinc abundance, which does not change during stellar nucleosynthesis in the interiors of low- and intermediate-mass stars, changes by the same value as the iron abundance over a wide range of metallicities [49, 52]. For this reason, the conclusion about the zinc overabundance does not depend on which scale (differential or absolute) it was obtained. The sulfur overabundance is more difficult to interpret. The mean sulfur abundance for unevolved solar-metallicity stars is 0.15 dex higher than the solar value, while for the metallicity [Fe/H] = –0.65 the sulfur overabundance is [S/Fe] = +0.35 [49]. It should be noted that the sulfur overabundance [S/Fe] = +0.55 [1] is also observed in the atmosphere of the normal Population I supergiant α Per without evidence of a circumstellar envelope. Consequently, only part of the sulfur overabundance [S/Fe] in the IRAS 23304 atmosphere can be explained by the condensation of iron nuclei.

Both its Galactic latitude (b = +1°) and radial velocity provide evidence that we are dealing with a Population I object. If the initial (i.e., before the elemental separation) ratios [Zn/Fe] and [S/Fe] in the IRAS 23304 atmosphere are assumed to match their means for unevolved disk stars ([Zn/Fe] = 0 and [S/Fe] = +0.15), then we can estimate the underabundance of iron nuclei because of condensation, –0.54 dex, which is close to that in Table 5 ([Fe/H] = –0.65). Consequently, if we accept the hypothesis of elemental separation in the envelope, then, by all signs, the object should be classed with Population I post-AGB stars.

Thus, the results of our abundance determinations for the IRAS 23304 atmosphere (see below) can all be considered in terms of two hypotheses: (1) a disk object with an initial solar metallicity and with the observed abundances of iron-peak elements (V, Cr, Fe, Ni) reduced by fractionation and (2) an old-disk object with the initial metallicity [Fe/H] = –0.65 and abnormally high abundances of zinc and sulfur.

The atmospheric CNO abundances in IRAS 23304 differ markedly from their solar values. The enhancement of carbon and nitrogen in IRAS 23304, [C/Fe] = +0.98 and [N/Fe] = +1.36, was derived fairly reliably from a large set of spectral lines of these elements. The oxygen overabundance was determined by using the equivalent widths of three lines near a wavelength of 6155 Å without allowance for the infrared oxygen triplet. The derived abundance ratios C/N/O lead us to conclude that we detected signatures of dredge-up of the matter processed during hydrogen and helium burning (third dredge-up) in the stellar atmosphere. This conclusion is also confirmed by the large overabundance of the *s*-process elements yttrium ([Y/Fe] = +0.91) and barium ([Ba/Fe] = +1.73). The conclusion is valid both for the first and second hypotheses.

The equivalent width of the Li I λ6707 Å resonance doublet in the IRAS 23304 spectrum was measured fairly reliably. Interestingly, the relative abundance of lithium [Li/Fe] = 0.01 corresponds to the situation in the Solar system (Table 5 gives the lithium abundance in meteorites for the solar chemical composition). The synthesis of Li nuclei at the AGB stage is possible for a narrow range of luminosities M_{bol}, from -6^m to -7^m [53]. This is consistent with spectroscopy of AGB stars in the Magellanic Clouds [54, 55].

The sodium overabundance relative to metallicity [Na/Fe] = +0.49 is within the range of values known for high-luminosity stars (according to the first hypothesis, the sodium abundance is nearly solar). We emphasize that the sodium overabundance (relative to metallicity) is observed both for young massive supergiants [56-58] and for definitely low-mass high-luminosity stars in globular clusters [59]. Previously [21], we considered the large sodium overabundance in the atmospheres of supergiants in more detail.

The conclusion about the enhancement of silicon is valid for both hypotheses; as a result, a nonsilicate composition of the envelope dust can be assumed.

The three available spectra clearly revealed an overabundance of heavy metals (La, Ce, Nd, Pr, Eu): [*X*/Fe] = +1.04. According to the second hypothesis, the significant mean overabundance (0.4 dex) is preserved. The ratio [Ba/Eu] is an *s*-process indicator independent of metallicity for [Fe/H] > –1. [Ba/Eu] ~ 0 for unevolved stars [50] and [Ba/Eu] = 1.08 in the IRAS 23304 atmosphere, which provides evidence for the operation of the *s* process [60].

In general, the abundance pattern for IRAS 23304 suggests that elements before the iron peak and heavier elements are overabundant. This pattern is more distinct for the first hypothesis but does not change fundamentally if we abandon the assumption that a considerable fraction of iron atoms condense. Such an abundance pattern, which formed with the involvement of separation, is observed in the atmospheres of several post-AGB stars with large infrared excesses attributable to circumstellar envelopes [21, 26, 61, 62].

The results for scandium allow us to make a more definitive choice between the two hypotheses under consideration. For the developed separation processes, the abundance of this element in the gas component decreases much more rapidly than the iron abundance (see, e.g., [62]). At the same time, the relative atmospheric abundance of scandium in the object under study is [Sc/Fe] = +0.18. Thus, the abundance of zinc and, partly, sulfur provides evidence for the separation hypothesis, but the scandium abundance is in conflict with the overall pattern of separation. We are therefore inclined to assert that the detected chemical anomalies in IRAS 23304 are mostly the result of stellar nucleo-

synthesis (CNO and *s*-process elements), while the role of separation is open to argument.

It should be noted that the abundance pattern in the IRAS 23304 atmosphere is consistent with the chemical composition of several related objects which form a special subgroup of PPNe with similar parameters (temperature, metallicity): IRAS 07134+1005 [1], IRAS 19500–1709 [19], IRAS 05341+0852 [16], IRAS 04296+3429 [9, 17], and IRAS 22223+4327 [17]. The expected signatures of the third dredge-up were revealed in the atmospheres of objects only from this small subgroup of PPNe with carbon-rich gas–dust envelopes, while the infrared spectra of all these objects exhibit an as yet unidentified band at 21 μm.

CONCLUSION

Based on echelle spectra from the 6-m telescope, we studied the spectrum of the faint star identified with the infrared source IRAS 23304. The abundance of the iron-peak elements is, on the average, [X/H] = –0.61 dex; assuming a low separation efficiency of these elements, IRAS 23304 can be classified as belonging to the old disk population. The abundances of the CNO and *s*-process elements were found to increase. The above evolutionary changes in chemical composition allow this object to be classified as belonging to the small class of PPNe identified by a set of signatures in the infrared and optical spectra. As an additional empirical criterion, the presence of circumstellar diffuse absorption bands may be added to the set of such signatures (a carbon-rich envelope, the 21-μm band in the infrared spectrum, atmospheric overabundances of the CNO and *s*-process elements) that was drawn up by Klochkova *et al.* [9] and Decin *et al.* [17]. It was shown that the circumstellar envelopes, which manifest themselves in molecular absorption lines, could also exhibit molecular emission features. The expansion velocities of the IRAS 23304 envelope measured from the absorption and emission molecular spectra are essentially the same.

ACKNOWLEDGMENTS

The spectroscopic study of anomalous supergiants with infrared excesses is supported by the Russian Federal Program “Astronomy” (project no. 1.4.1.1), the Russian Foundation for Basic Research (project no. 99-02-18339), and the Polish State Research Committee (grants nos. 2.P03D.026.09 and 2.P03D.002.13).

REFERENCES

1. V. G. Klochkova, Mon. Not. R. Astron. Soc. **272**, 710 (1995).
2. V. G. Klochkova, Bull. SAO **44**, 5 (1998).
3. L. Zaĉs, V. G. Klochkova, and V. E. Panchuk, Mon. Not. R. Astron. Soc. **275**, 764 (1995).
4. L. Zaĉs, V. G. Klochkova, V. E. Panchuk, *et al.*, Mon. Not. R. Astron. Soc. **282**, 1171 (1996).
5. V. G. Klochkova and V. E. Panchuk, Bull. SAO **41**, 5 (1996).
6. V. G. Klochkova and T. V. Mishenina, Bull. SAO **44**, 83 (1998).
7. V. G. Klochkova, E. L. Chentsov, and V. E. Panchuk, Astron. Astrophys. **323**, 789 (1997).
8. V. G. Klochkova, E. L. Chentsov, and V. E. Panchuk, Mon. Not. R. Astron. Soc. **292**, 19 (1997).
9. V. G. Klochkova, R. Szczerba, and V. E. Panchuk, Astrophys. Space Sci. **255**, 485 (1997).
10. S. Kwok, Ann. Rev. Astron. Astrophys. **31**, 63 (1993).
11. K. Volk and S. Kwok, Astrophys. J. **342**, 345 (1989).
12. B. J. Hrivnak and S. Kwok, Astrophys. J. **368**, 564 (1991).
13. E. J. Bakker, E. F. Van Dishoeck, L. B. F. M. Waters, *et al.*, Astron. Astrophys. **323**, 469 (1997).
14. S. Kwok, K. Volk, and B. J. Hrivnak, Astrophys. J. Lett. **345**, L51 (1989).
15. S. Kwok, B. J. Hrivnak, and T. R. Geballe, Astrophys. J. **454**, 394 (1995).
16. B. E. Reddy and M. Parthasarathy, Astron. J. **112**, 2053 (1996).
17. L. Decin, H. van Winkel, C. Waelkens, *et al.*, Astron. Astrophys. **332**, 928 (1998).
18. M. Parthasarathy, P. García Lario, and S. R. Pottash, Astron. Astrophys. **264**, 159 (1992).
19. H. van Winckel, Astron. Astrophys. **319**, 561 (1997).
20. B. E. Reddy, M. Parthasarathy, G. Gonzáles, *et al.*, Astron. Astrophys. **328**, 331 (1997).
21. V. G. Klochkova and V. E. Panchuk, Pis’ma Astron. Zh. **24**, 754 (1998) [Astron. Lett. **24**, 650 (1998)].
22. V. E. Panchuk, I. D. Najdenov, V. G. Klochkova, *et al.*, Bull. SAO **44**, 127 (1998).
23. G. Cayrel de Strobel, *Calibration of Fundamental Stellar Quantities*, in *Proceedings of IAU Symposium No. 111*, Ed. by D. S. Haynes, L. E. Pasinetti, and A. G. D. Philip (Reidel, Dordrecht, 1985), p. 137.
24. R. L. Kurucz, *ATLAS 9 Stellar Atmosphere Programs and 2 km/s Grid*, CD-ROM No. 136 (Smithsonian Astrophysical Observatory, 1993).
25. R. E. Luck, Astrophys. J., Suppl. Ser. **75**, 579 (1991).
26. S. Giridhar, N. K. Rao, and D. Lambert, Astrophys. J. **437**, 476 (1994).
27. R. Szczerba, A. Omont, K. Volk, *et al.*, Astron. Astrophys. **317**, 859 (1997).
28. A. Omont, S. H. Moseley, P. Cox, *et al.*, Astrophys. J. **454**, 819 (1995).
29. F. Rouleau and P. G. Martin, Astrophys. J. **377**, 526 (1991).
30. B. J. Hrivnak, Astrophys. J. **438**, 341 (1995).
31. P. García Lario, A. Manchado, S. R. Pottasch, *et al.*, Astron. Astrophys., Suppl. Ser. **82**, 497 (1990).
32. J. A. Cardelli, G. C. Clayton, and J. S. Mathis, Astrophys. J. **345**, 245 (1989).
33. Th. Neckel and G. Klare, Astron. Astrophys., Suppl. Ser. **42**, 251 (1980).

34. D. Crampton, A. P. Cowley, and R. M. Humphreys, Astrophys. J. Lett. **198**, L135 (1975).
35. G. D. Schmidt, M. Cohen, and B. Margon, Astrophys. J. Lett. **239**, L133 (1980).
36. C. Waelkens, H. van Vinkel, N. R. Trams, *et al.*, Astron. Astrophys. **256**, L15 (1992).
37. S. P. Balm and M. Jura, ASP Conf. Ser. **45**, 137 (1993).
38. P. J. Sarre, J. R. Miles, and S. M. Scarrott, Science **269**, 674 (1995).
39. V. V. Tsymbal, ASP Conf. Ser. **108**, 198 (1995).
40. P. Jenniskens and F.-X. Desert, Astron. Astrophys., Suppl. Ser. **106**, 39 (1994).
41. M. Cohen and B. F. Jones, Astrophys. J. Lett. **321**, L151 (1987).
42. T. Le Bertre and J. Lequeux, Astron. Astrophys. **274**, 909 (1993).
43. D. A. Williams, Astrophys. Space Sci. **237**, 243 (1996).
44. G. Chlewicki, M. S. de Goort, G. P. van der Zwet, *et al.*, Astron. Astrophys. **173**, 131 (1987).
45. J. Krelowski and G. A. H. Walker, Astrophys. J. **312**, 860 (1987).
46. P. Jenniskens, P. Ehrenfreund, and B. Foing, Astron. Astrophys. **281**, 517 (1994).
47. A. W. Woodsworth, S. Kwok, and S. J. Chan, Astron. Astrophys. **228**, 503 (1990).
48. N. Grevesse, A. Noels, and A. J. Sauval, ASP Conf. Ser. **99**, 117 (1996).
49. F. X. Timmes, S. E. Woosley, and T. A. Weaver, Astrophys. J., Suppl. Ser. **98**, 617 (1995).
50. A. McWilliam, Ann. Rev. Astron. Astrophys. **35**, 503 (1997).
51. H. E. Bond, Nature **356**, 474 (1992).
52. J. C. Wheeler, C. Sneden, and J. W. Truran, Jr., Ann. Rev. Astron. Astrophys. **27**, 279 (1989).
53. I.-J. Sackmann and A. I. Boothroyd, Astrophys. J. Lett. **392**, L71 (1992).
54. V. V. Smith and D. L. Lambert, Astrophys. J. Lett. **345**, L75 (1989).
55. V. V. Smith and D. L. Lambert, Astrophys. J. Lett. **361**, L69 (1990).
56. D. D. Sasselov, Publ. Astron. Soc. Pac. **98**, 561 (1986).
57. A. A. Boyarchuk, I. Gubeny, I. Kubat, *et al.*, Astrofizika **25**, 335 (1988).
58. A. A. Boyarchuk, L. S. Lyubimkov, and N. A. Sakhibullin, Astrofizika **28**, 343 (1988).
59. G. González and G. Wallerstein, Mon. Not. R. Astron. Soc. **254**, 343 (1992).
60. R. A. Malaney, Astrophys. J. **321**, 832 (1987).
61. G. González, D. L. Lambert, and S. Giridhar, Astrophys. J. **479**, 427 (1997).
62. G. González, D. L. Lambert, and S. Giridhar, Astrophys. J. **481**, 452 (1997).

Translated by V. Astakhov